UNIVERSIDADE FEDERAL DO RIO DE JANEIRO
OBSERVATÓRIO DO VALONGO

On the distance to expansion nebulae based on the improved distance mapping technique

Sebastian Gómez Gordillo

Dissertação de Mestrado apresentada ao Programa de Pós-Graduação em Astronomia da Universidade Federal do Rio de Janeiro - UFRJ, como parte dos requisitos necessários à obtenção do título de Mestre em Ciências (Astronomia).

Advisor: **Denise Rocha Gonçalves**
Co-Advisor: **Stavros Akras**

Rio de Janeiro
March 23, 2018

On distances to expasion nebulae based on the improved distance mapping technique

Sebastian Gomez Gordillo

Dra. Denise Rocha Gonçalves (Orientadora)
Stavros Akras (Co-orientador)

Dissertação de mestrado submetida ao Programa de Pós-Graduação em Astronomia, Observatório do Valongo, da Universidade Federal do Rio de Janeiro - UFRJ, como parte dos requisitos necessários à obtenção do título de Mestre em Ciências - Astronomia.

Aprovada por:

Denise Rocha Gonçalves

Presidente, Dra. Denise Rocha Gonçalves- (Orientadora) – OV/UFRJ

Dr. Hektor Sthenos Alves Monteiro – (Avaliador Externo)- UNIFEI

Dr. Helio Jaques Rocha Pinto – (Avaliador Interno) – OV/UFRJ

Rio de Janeiro
Março de 2018

CIP - Catalogação na Publicação

G633o

Gómez Gordillo, Sebastian
On the distance to expansion nebulae based on the improved distance mapping technique / Sebastian Gómez Gordillo. -- Rio de Janeiro, 2018.
106 f.

Orientadora: Denise Rocha Gonçalves.
Coorientador: Stavros Akras.
Dissertação (mestrado) - Universidade Federal do Rio de Janeiro, Observatório do Valongo, Programa de Pós-Graduação em Astronomia, 2018.

1. Distances. 2. 3D models. 3. Planetary Nebulae. 4. Stellar Remnants. I. Rocha Gonçalves, Denise, orient. II. Akras, Stavros, coorient. III. Título.

Elaborado pelo Sistema de Geração Automática da UFRJ com os dados fornecidos pelo(a) autor(a).

Acknowledgements

First, special thanks to my family. Thanks for always being there, for all the support, for the lovely words and all the expressions through the distance. Thanks for giving me the bases to endure and overtake all the challenges that I had and that I will face.

I would like to thank my advisors, Stavros Akras and Denise Rocha Gonçalves. Thanks for all the help, the lessons, the discussions, for always be there when I needed, and for show and teach me how science is made. Your guidance and understanding was fundamental in my journey during these 2 years. It was great to meet you guys.

I have to recognize that this marvelous journey in astronomy started long ago in El Grupo Halley de Astronomía y Ciencias Aeroespaciales from the Universidad Industrial de Santander, in Bucaramanga, Colombia. There, I met exceptional people and I had a bunch of great times. One of these friends, an incredible woman, Heidy Quitian, decided to follow her cosmic dreams with a further step, and eventually showed to me that things which seems impossible are actually not, when you really want them. I am deeply grateful Heidy, for open to me the doors, of the astronomical science and of Brazil. Thanks for all the motivation and help.

My deepest gratitudes to my Brazilian roots, de Sousa and Paiva families. You received this Colombian in your lifes with widely open arms, as a son, a brother, a cousin, a nephew and a grandchild. You showed to me what is Brazil, how delicious, joyful, warm, hospitable and humble it is. Thanks for all the parties, the barbecues and adventures that we shared together. You made this journey a lot more better and enjoyable. We will meet again soon!

I can not forget the Macacos! I would never imagine how great is the Ultimate community here in Brazil, but specially here in Rio de Janeiro. Playing with you guys have no price. So many games and celebrations have taught me that this sport is far beyond the field. Thanks for let me keep the disc flying with you all. Up!

To all my friends here at the Valongo Observatory (OV-UFRJ) thank you so much, for the support, the histories, the company and all those fun times. Special thanks to Ana Carolina L., what a classmate, friend and wonderful person. The best of the best for your life.

To Claudia F., my absolute gratitude for being such a warm, intelligent and helpful person.

Finally I would like to thank CAPES for the financial support.

For you people, which decide to explore the mysterious wonders of the sky, keep scratching the truths, maybe, one day we will understand what is going on.

For Ely and Helio.

To Callithrix.

Resumo

Resumo da Dissertação de Mestrado submetida ao Programa de Pós-graduação em Astronomia da Universidade Federal do Rio de Janeiro - UFRJ, como parte dos requisitos necessários à obtenção do título de Mestre em Ciências (Astronomia).

Diversos objetos astrofísicos como nebulosas planetárias (PNe), remanescentes de nova e supernova e as nebulosas de estrelas variáveis azuis luminosas, entre outros, mostram expansão radial. Todos estes objetos necessitam uma determinação precisa da distância, já que esta é parâmetro essencial para derivar suas características físicas, tais como tamanho, massa, luminosidade e idade. Uma técnica inovadora baseada no método da paralaxe de expansão - a técnica de mapeamento de distância, DMT - foi recentemente proposta por Akras & Steffen (2012). Esta técnica combina vetores de velocidade tangencial, advindos de modelos morfo-cinemáticos tri-dimensionais (3D) e vetores de movimentos próprios observados para estimar a distância. A técnica DMT foi aprimorada e estudada estatisticamente com o objetivo de restringí-la e de entender a relação entre seus parâmetros de entrada e o cálculo da distância. DTM foi então aplicada, com êxito, a quatro PNe (NGC 6702, NGC 6543, NGC 6302 e BD+30 3639), uma remanescente de nova (Gk Persei) e à componente externa de η Carinae. Utilizando o código morfo-cinemático 3D SHAPE geramos novos modelos para NGC 6543, NGC 6302 e NGC 6702, enquanto que para as demais nebulosas usamos modelos da literatura. As novas estimativas de distância desses objetos concordam muito bem com estudos anteriores, excetuando-se o caso de η Carinae. Também demonstramos que a técnica DMT é uma ferramente útil para revelar regiões cinematicamente diferenciadas do restante da nebulosa, além de ser robusta na determinação da distância.

Keywords: Distâncias. Modelos em 3 dimensões. Nebulosas planetárias. Remanescentes estelares.

Abstract

Abstract da Dissertação de Mestrado submetida ao Programa de Pós-graduação em Astronomia da Universidade Federal do Rio de Janeiro - UFRJ, como parte dos requisitos necessários à obtenção do título de Mestre em Ciências (Astronomia).

Astrophysical objects as planetary nebulae (PNe), nova and supernova remnants and the stellar ejecta of luminous blue variables, among others, show radial expansion. An accurate distance determination is needed for all these kind of objects, since it is an essential parameter for deriving their physical characteristics, such as size, mass, luminosity and age. An innovative technique based on the expansion parallax method – the distance mapping technique, DMT – was recently proposed by Akras & Steffen (2012). It combines tangential velocity vectors from 3D morpho-kinematic models and observed proper motion vectors to estimate the distance. The DMT was improved and statistically studied in order to understand the relationship between its input parameters and the resulting distance. We successfully applied the DMT to four PNe (NGC 6702, NGC 6543, NGC 6302 and BD+30 3639), one nova remnant (Gk Persei) and the outer ejecta of η Carinae. New morpho-kinematic SHAPE models are generated for NGC 6543, NGC 6302 and NGC 6702, whereas for the remaining nebulae published models are used. The new distance estimated for these objects is found to be in good agreement with previous studies, except for the complex multicomponent model of η Carinae. We demonstrated the DMT is an useful tool for revealing kinematically peculiar regions within the nebulae, in addition to provide robust distance determination.

Keywords: Distances. 3D models. Planetary nebulae. Stellar remnants.

Contents

List of Figures

List of Tables

Chapter 1

Introduction

The stellar progenitors of planetary nebulae (PNe) are low-to-intermediate mass stars (0.08 to 8 $M_{\odot}$) (Osterbrock & Ferland, 2006). They are among the fastest evolving astrophysical objects known. They last only a few thousand years compared with the characteristic stellar lifetime of its progenitors, which live for billions of years (Frew & Parker, 2010). Studies on PNe have shown that they serve as tools for stellar evolution, galaxy and gas dynamics (Kwok, 2007). PNe also work as tracers of chemical abundances of stellar population, even in the intracluster medium (Bresolin et al., 2010), but more important as standard candles for the extragalactic distance scales, by means of their luminosity function (PNLF) (Ciardullo, 2012).

1.1 Stellar evolution of PNe progenitors

Nowadays, we understand PNe as one of the last stages of stellar evolution of low- and intermediate-mass stars. Roughly speaking these stars are born in giant molecular clouds of typical masses of $10^5 - 10^6$ $M_{\odot}$, reaching dimensions of approximately 10 pc, with temperatures of 10 - 100 K and densities of 10 - 300 particles/cm^3. The ones with the lowest temperatures being the densest (Kippenhahn & Weigert, 2012).

The following summary of protostar formation and pre-main sequence evolution presented here is based on Kippenhahn & Weigert (2012) and Salaris & Cassisi (2005).

1.1.1 Main sequence evolution

The pre-main sequence phase will last at least one hundred million years. After that time, if the protostars present masses equal or higher than 0.08 $M_{\odot}$, the H fusion temperature will be high enough ($\backsim 10^6$ K) to turns the premain sequence stars into stars of zero-age main sequence (ZAMS). From this point onwards, the ZAMS stars are powered by the central H-burning which releases nuclear binding energy by converting H atoms into He atoms. The contraction is halted by the energy produced by the nuclear fusion keeping the star in complete hydrostatic and thermal equilibrium. The stars evolve away from the ZAMS towards large radii and luminosities, entering in the most important phase of stellar evolution, the main sequence. The H-burning phase or main sequence (MS) phase, is the longest evolutionary stage. As an example, the Sun will last about 11.5

billion years. The lifetime in the MS is strongly related with the stellar mass, decreasing as the mass increases (Salaris & Cassisi, 2005). The evolution of the Sun (an excellent example of a low-mass star) in the Hertzsprung–Russell (HR) diagram, from the end of the protostellar stage to its final possible destiny is presented in Fig. 1.1. After the protostellar stage, the proto-Sun enters in the premain sequence and eventually, when this phase ends, the Sun joins the MS phase.

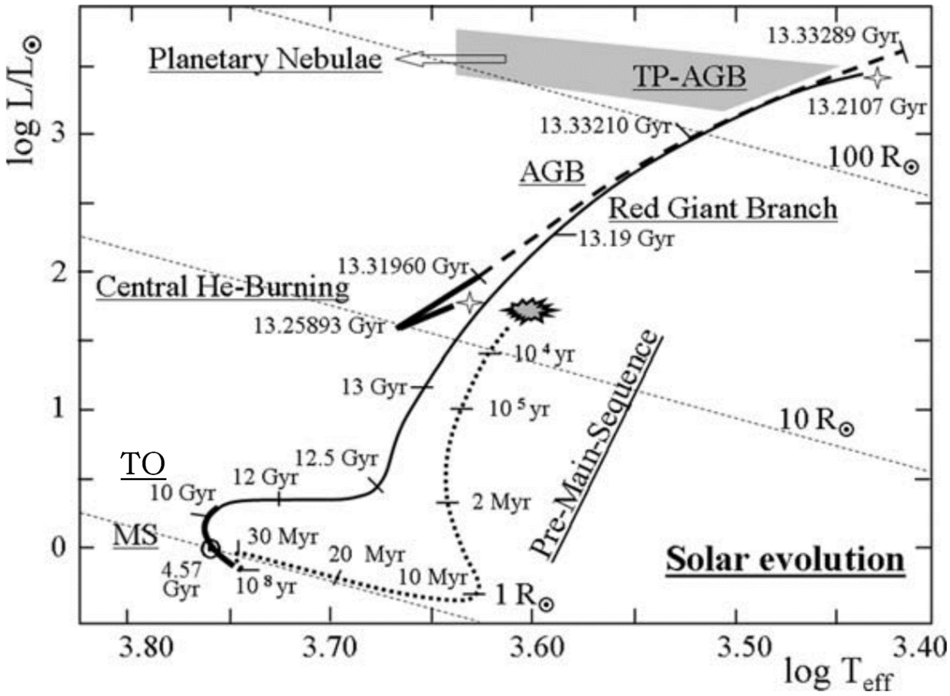

FIGURE 1.1: HR diagram of the solar-type stars evolution for $X = 0.72$ (H content), $Y = 0.266$ (He content) and $Z = 0.014$ (other elements content). Ages are indicated along the evolutionary track. Temperature is given in K. Adapted from Maeder (2008).

The formation of heavier elements than H, in the core of the star, induces a change in its composition through time, which generates the chemical evolution of the star. It is primarily concentrated on the core, where the fusion process is dominant, but larger volumes could be affected if a convective core is present (stars with $M > 1\ M_{\odot}$), due to the mixing induced (Kippenhahn & Weigert, 2012).

Fusion of the H nuclei can be achieved by two thermonuclear reactions, the proton-proton (p-p) chain and the CNO cycle. The p-p chain is present at lower nuclear temperatures ($T \leq 15\ \times 10^6$ K) in the case of low-mass stars, while the CNO cycle is the dominant reaction at higher temperatures, for larger stellar masses. H burning is the principal source of ^{7}Be and isotopes of C, N, O, F, Na and Ne. During its conversion into He, the H abundance decreases at the core and an inert He core begins to form. The number of free particles also decreases, which makes the pressure drops. Since the star self regulates the nuclear energy production to maintain hydrostatic equilibrium, a slight star contraction is needed to heat the core. The star's luminosity will maintain a slow growth trend over this phase because of the rise of the molecular weight and temperature (Salaris & Cassisi, 2005).

1.1.2 Post-main sequence evolution

The central H-burning phase continues until the H core is completely exhausted in the core. This stage corresponds to the point in the evolutionary track of a star where it leaves the MS phase, and it is called the turn off point (TO). The TO of the Sun will be approximately 5 Gy from now, as is shown in Fig. 1.1. For intermediate-mass stars it is marked with the letter "C" on Fig. 1.2. Initially, the nuclear fusion rate is maximum at the center, where the H abundance is homogeneous and the temperature is the highest. With time, the amount of central H drops and the central temperature keeps raising which switch the maximum of the nuclear fusion rate outside the center. After the exhaustion of the H in the stellar core, the burning process continues in the surrounding layer, while the He core contracts, and an H-burning shell appears around it (Salaris & Cassisi, 2005).

The evolution of the stars after the MS phase strongly depends on the stellar mass. Low mass stars (up to ~ 2.3 M$_\odot$) develop a degenerate He core surrounded by a H burning shell, present a long-lived red giant branch (RGB) phase, and display a violent He core ignition, called He flash. The intermediate-mass stars ($\sim 2.3 < M <\sim 8$ M$_\odot$) ignite He in a non-degenerate He core, displaying a further formation of a degenerate C-O core, and present a very short-lived RGB phase (Kippenhahn & Weigert, 2012).

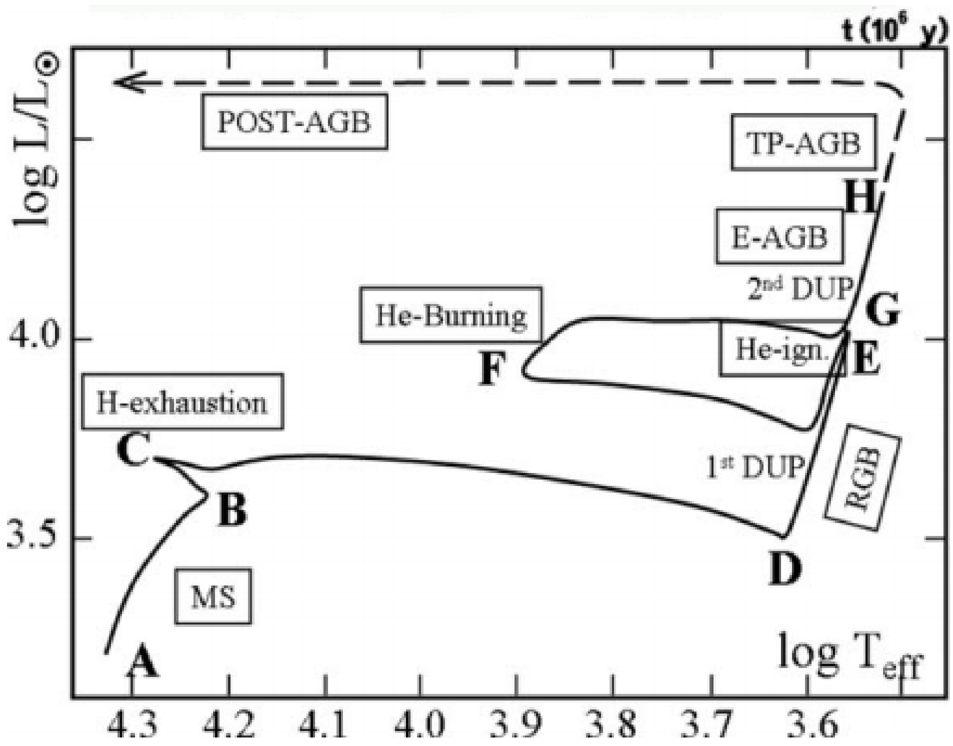

FIGURE 1.2: HR diagram showing the different phases of stellar evolution of intermediate-mass stars (7 $M_\odot$). Surface temperature give in K. Taken from Maeder (2008).

In intermediate-mass stars, the H burning shell increases the mass of the He core, which leads to a core contraction and temperature increase. The decreasing density of the burning shell leads to a pressure drop. To maintain thermal equilibrium, the H burning shell must remain at an approximately constant temperature, because of the thermostatic action of the nuclear fusion, and the shell can not display contraction, since it implies heating. Therefore, the pressure of the overlying envelope must decrease, entailing expansion of the layers above the H burning shell, and decreasing its surface temperature, as it is shown on the track from the letter "C" to "D" in Fig. 1.2. Due to the expansion, the outer layers cool down and the envelope opacity increases. Further expansion is supported by the energy trapped in the envelope. After the outer layers are cool enough because of the expansion, the stellar envelope becomes convective. Since convection is a very efficient energy transport mechanism, it slows down further expansion (avoiding the star dissolution) and marks the beginning of the RGB phase. Future expansion occurs at almost constant surface temperature while the luminosity increases. The material formed by the H burning shell is mixed (because the penetration of the outer convective layers into the H burning shell) through the envelope, reaching the surface. Such process is called dredge up. The first dredge up and the beginning of the RGB phase are marked on the track above as letter "D", in Fig. 1.2. The core contracts and finally reaches the temperature for efficient He burning, 10^8 K. The core contraction stops when the star is mainly nuclear burning supported, the RGB phase ends and the He burning stage starts, which corresponds to the longest phase after central H burning (Salaris & Cassisi, 2005). The final stage of post-main sequence evolution is marked from letter "E" on the evolutionary track in Fig. 1.2.

For low-mass stars, the He core becomes electron degenerated because it is relatively dense and cool. The degeneracy pressure can support the weight of the envelope and the star can remain in hydrostatic and thermal equilibrium through the phase of H shell burning. The shell adds new He material to the core and progressively migrates outward. The star is becoming a red giant, entering in the RGB phase. The Sun will turn into a red giant after it is 13 Gyr old, as it is shown in Fig. 1.1. An outer convective zone is developed and penetrates deeper in the star. This results in the increase of stellar luminosity. The first dredge up occurs and brings nuclear material to the surface. As the core grows, the rising of the luminosity and the radius inflation in the RGB accelerates. Then, the tip of the RGB is reached together with the ignition temperature of He. Since the core is highly degenerate, this produces a violent nuclear instability, called the He flash. The maximum of the local luminosity is around 10^{11} $L_{\odot}$, almost the luminosity of a whole galaxy, but only for a few seconds (Maeder, 2008). Most of the energy is absorbed by the expansion of the non-degenerate outer layers and another portion is irradiated by neutrinos. The He flash for the Sun is denoted in Fig. 1.1 by two 4-piked stars, showing its beginning and ending. Millions of years after a series of recurrent flashes occurring at the core, its degeneracy is fully removed. In the process, the luminosity drops by one order of magnitude because the expansion of the He core cools down the H burning shell, contracting the stellar envelope. The He burning ignites at some distance of the stellar center due to the strong neutrino cooling. Finally, the content of He has decreased in approximately 5% due to its conversion to C and the star initiates a non-degenerate phase of central He burning, because of the achieved thermal conditions ($\backsim 10^8$ K) for an efficient He fusion (Maeder, 2008).

The fundamental nuclear reactions present at the He burning phase are the triple alpha process (3α), the $^{12}\mathrm{C}(\alpha,\gamma)^{16}\mathrm{O}$ and $^{16}\mathrm{O}(\alpha,\gamma)^{20}\mathrm{Ne}$. Consequently, the He is mainly transformed into a mixture of ^{12}C, ^{16}O and ^{20}Ne. In the 3α process three ^{4}He nuclei are converted into ^{12}C (Salaris & Cassisi, 2005).

At this stage, the star is characterized by two nuclear burning sources, the nuclear He burning and the shell H burning around the He core. The star luminosity and its radius rise again due to the extra energy component provided by the central He burning. The high concentration of energy at the core make it convective together with the region over it. As long as the luminosity generated by the H burning shell is larger than that of the He burning, the star evolves towards larger surface temperatures. However, the efficiency of the H burning shell monotonically decreases as the efficiency of the He burning steadily increases. Then, the surface temperature drops and the central He burning dominates over the H burning shell. This process makes the star describes a loop in the HR diagram. The extension of these loops depends on the stellar mass. Large loops are generated by stars with large masses and vice versa (Kippenhahn & Weigert, 2012). A better loop is described by the star of 7 $M_{\odot}$ than by the Sun, as it is shown in Figs. 1.1 and 1.2.

1.1.3 Late evolution of PN progenitor stars

Tens of millions of years after the He burning phase started, the ^{4}He in the core has been processed mainly into ^{12}C, ^{16}O and ^{20}Ne, marking the end of the central He burning. The star then evolves to lower surface temperature and higher luminosity, to the so called asymptotic giant branch (AGB). The He burning continues, but in a concentric shell around the inert C-O core. Stars with initial masses lower than 8 $M_{\odot}$ present a degenerate C-O core, in which the electron degeneracy is high enough to prevent carbon ignition. The degenerate C-O core contracts and the He burning shell expands. This makes the H burning shell cools down and its burning process is reduced. This stage is called the early AGB (E-AGB). The outer convective envelope penetrates into the H shell, mixing the ashes of H burning. This represents the second dredge up, which transports the nuclear material from the H-burning shell to the stellar surface, and increases the stellar opacity. The E-AGB phase and the second dredge up are marked with the letter "G" in the case of a star with 7 $M_{\odot}$, in Fig. 1.2. For lower mass stars the H burning shell remains active at a low level, preventing the outer convective envelope from penetrating deeper into the star, and the second dredge up is halted in this case (Kippenhahn & Weigert, 2012; Maeder, 2008). The AGB phase for the Sun is denoted by the dashed line in Fig. 1.1. At 13.3196 Gyr the central He will be exhausted and the Sun will enter the E-AGB.

As the active part of the He burning shell reaches the inert H shell, it runs out of fuel and its luminosity decreases. Then, the He burning is halted which generates a contraction of the upper layers in response, by heating the inert H shell and igniting it. The H burning shell will add mass between the He and H shell (the intershell region) increasing the temperature and density of this region. The He in the intershell will be ignited in an unstable way, through the helium shell flash. The energy released drives convection in the intershell region and expands it. This extinguishes the H burning shell and provides a phase of stable He burning shell. Henceforth, the star displays alternating cycles of nuclear burning shells. The He burning shell becomes thermally unstable and the star undergoes periodic thermal pulses. This stage of stellar evolution is called thermally pulsing AGB (TP-AGB).

These thermal pulsation are understood as a pushing of the envelopes outward, because of the expansion of He shell, without having an influence on the core. In the case of low-mass stars, the luminosity and the surface temperature can vary appreciably within each pulsation. The variation is more pronounced if small amount of mass has been left in the unstable shells. Expansion and cooling of the intershell region could guarantee a deeper penetration of the outer convective envelope, beyond the H shell, and bring combined ashes from the He and H burning to the outer envelope. Such event, is called the third dredge up, in which He and ^{12}C can appear at the surface. The third dredge up is not yet fully understood, but explains the formation of carbon stars (stars with C/O > 1) (Maeder, 2008).

AGB stars are considered to be the major producers of C, N and elements heavier than Fe, by the s-process, slow neutron capture on Fe nuclei. The s-process needs a source of free neutrons, which are generated in the He-rich intershell region and brought to the surface by the dredge ups (Maeder, 2008; Kippenhahn & Weigert, 2012). The Sun will reach its maximum radius, $\sim 312\ R_{\odot}$, at the tip of the AGB phase or during the TP-AGB phase (Fig. 1.1). A 7 $M_{\odot}$ star of (Fig. 1.2) reaches the TP-AGB at the letter "H".

AGB stars present strong mass-loss events, due to the thermal pulses cycles, which are repeated several times until the whole envelope is gone, and because of the stellar winds or, better known in this case as superwinds. The mass-loss rates range from 10^{-5} M$_{\odot}$/year to 10^{-8} M$_{\odot}$/year. The superwinds are understood as a result of the coupling of the radiation field with dust, which is previously formed in the outer stellar atmosphere (Kippenhahn & Weigert, 2012).

When the mass of the H-rich envelope is very small, due to the several mass-loss events, the envelope shrinks, and the star leaves the AGB. The decrease of the stellar radius occurs at almost constant luminosity, since the H burning shell is still active. The envelope mass continues decreasing, the bottom is eroded by the H burning and at the top by the continuous mass-loss. This makes the star follow a horizontal track in the HR diagram towards higher surface temperatures. This stage is called the post-AGB phase, where the star remains in complete equilibrium. When the surface temperature becomes as high as 30,000 K, the star develops a week but fast wind, driven by radiation pressure. Its strong UV flux destroys the dust grains in the circumstellar envelope, dissociates the molecules and ionizes the gas. This mark the birth of a planetary nebula, part of the circumstellar envelope is ionized and starts to re-radiate in recombination and collisionally excited lines (forbidden lines). After the stellar envelope mass is as lows as 10^{-5} M$_{\odot}$, the H burning shell is extinguished, at a typical surface temperature of 10^{5} K. Then, the luminosity starts decreasing and the stellar remnant cools as a white dwarf (WD) (Kippenhahn & Weigert, 2012).

Nuclear fusion no longer provides energy for to WD which continue shining by radiating the stored thermal energy in their interiors, cooling at almost constant radius and decreasing luminosities. The characteristic luminosities and masses are around $10^{-4.5}\ L_{\odot}$ and $0.6\,$M$_{\odot}$, respectively (Kippenhahn & Weigert, 2012).

1.2 Morphology and kinematic of PNe

PNe exhibit a great diversity of shapes and morphologies as the result of a complex and not yet well understood radiative and hydrodynamical mass-loss evolution of their progenitors. The different morphologies and their evolution is nowadays understood by means of the generalized interacting stellar winds (GISW) model, which provides a feasible explanation for the formation of PNe.

To understand the morphological diversity of PNe, different classification systems have been proposed, based on spatially resolved nebula and the symmetry criterion. The former divides the PNe in round (R) (e.g. Abell 39), elliptical (E) (e.g. IC 418), bipolar (B) (B are the ones that have opposite lobes from the central region, e.g. M2-9) and irregular (e.g. NGC 6326) (Balick, 1987). This morphological scheme does not take into account the projection effect, i.e. a bipolar nebula seen pole-on resembles a round PN (Frank et al., 1993). The symmetry criterion divides PNe in axisymmetric (reflection symmetry around mayor and minor axis, e.g. IC 4406), reflection symmetry (reflection symmetry around the minor axis only, e.g. M2-9), point symmetric (symmetry only through the nebular center, e.g. He3-1475) and asymmetric (no symmetry about an axis or point, e.g. NGC 6326) (Balick & Frank, 2002). Fig. 1.3 shows the PNe selected as examples to illustrate the previously described morphological classification schemes. Even considering the symmetry criterion, some PNe escape with surprising multi-axis symmetries, such as Hu 2-1 (Miranda et al., 2001), and various compact, low-ionization young PNe (Sahai & Trauger, 1998), all illustrated on Fig. 1.4.

Structurally PNe are composed of main nebular components (rim, shell and halo) surrounding the central star (CS). According to Schönberner et al. (2005) the global structure of the nebula can be understood in terms of three components; the rim, the shell and the halo. The rim is the innermost thin shell, and a hot bubble, which is compressed by the fast winds from the post-AGB star that hits the slow AGB wind. This fast-stellar wind also drives the density structure and expansion of the rim (Corradi et al., 2007). The shell is a dense thick region outside the rim, accelerated by the resultant shock of the penetration of the ionization front in the neutral ejecta. Its structure is governed by thermal pressure, which is maintained by the heating from photoionization (Corradi et al., 2007). At the outer region, the halo is shielded from the UV radiation of the CS by the thick shell. The halo have very low surface brightness which make their discovery very hard. They are usually attributed to final mass-loss episodes common in the subsequent phases of the AGB (Balick & Frank, 2002).

Additional concentric structures, like rings and arcs, are usually presented in the halo of several PNe and they are classified as: rings, broken rings, rings/broken rings, equatorial arcs, disconnected arcs and elliptical arcs. The first is defined as a complete (or mostly complete) round and concentric structure. The second includes small round segments that do not trace a complete round structure, or are partially intercepted and disrupted by elongated inner shells. The third is assigned when it is unclear whether the round segments are complete or not, the fourth encompasses small round segments, enveloping the equatorial waist of the PNe, the fifth consist of disconnected set of round segments along different directions and in the last class, enters the elliptical segments. These rings are arcs associated with low frequent (quasi-) periodic enhancements in the mass-loss rate

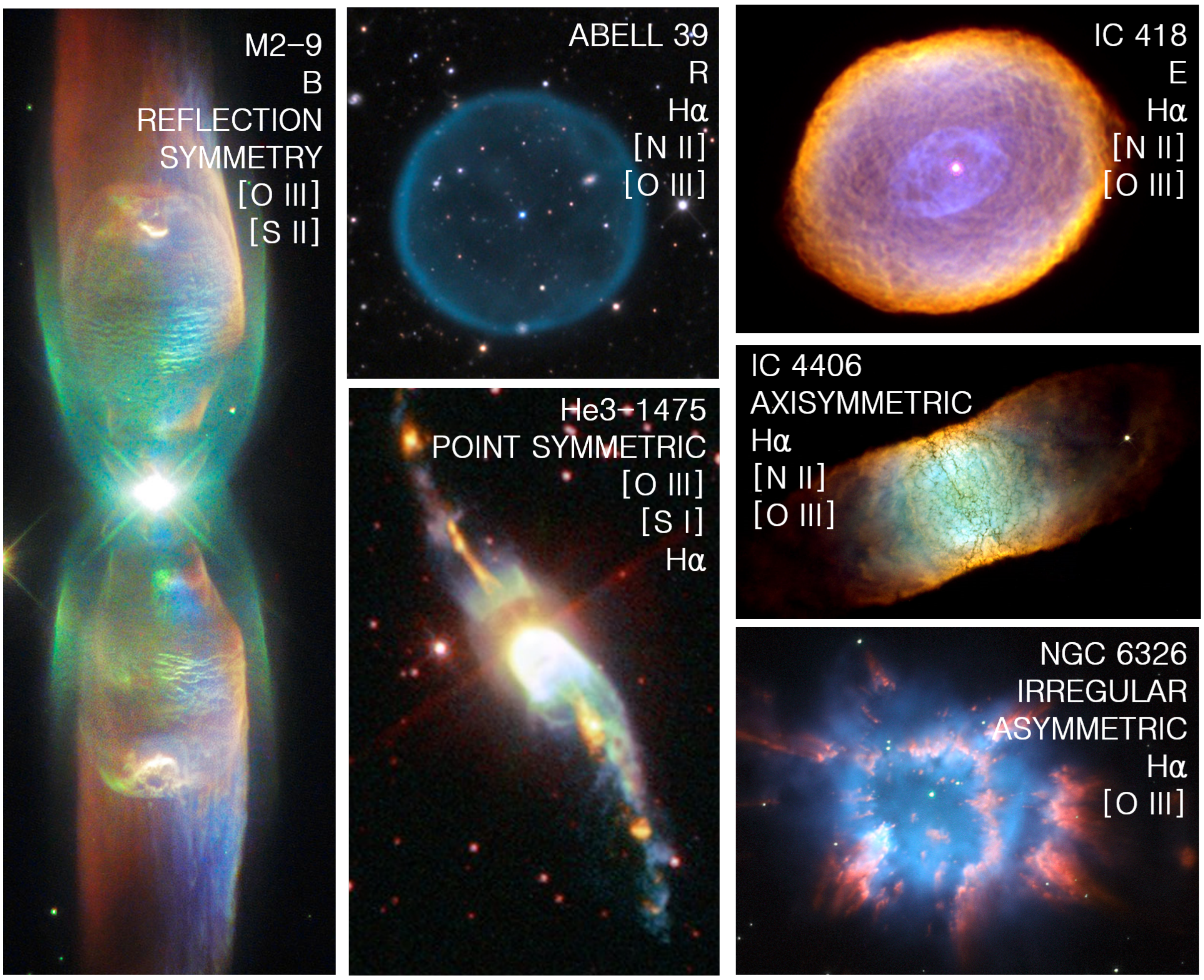

FIGURE 1.3: Morphological type illustration of PNe. M2-9 (B. Balick & NASA), Abell 39 (A. Frank Block/Mount Lemmon SkyCenter/University of Arizona), He3-1457 (ESA, A. Riera (Universitat Politecnica de Catalunya, Spain) and P. Garcia-Lario (ESA ISO Data Centre, Spain)), NGC 6326 (ESA/Hubble and NASA), IC 418 and IC 4406 (NASA and The Hubble Heritage Team (STScI/AURA)).

at the final stage of the AGB evolution; either because a small fraction of the progenitors produce such structures or they disappear with time (Ramos-Larios et al., 2016). All these concentric structures mentioned before are illustrated on Fig. 1.5.

PNe also exhibit a number of structures in smaller scales compared to the aforementioned features. Lying across the nebula are several fine-structures, like pairs of knots, jets, filaments and isolated features. Such structures, are morphologically and kinetically differentiated from the main bodies. Their spectrum is composed almost only of forbidden low ionization emission lines, such as [N II], [S II] and [O II]. In several cases the [O I] and [N I] emission lines are also detected. For that reason, they are called low-ionization structures (LIS) (Gonçalves et al., 2001). LIS seems to be spread across all the morphological types of PNe. Some of them have expansion velocities similar to the main bodies (rim, shell) of the nebula, while others have been found to exhibit velocities 2-3 or even more higher than the main components (Gonçalves et al., 2001).

The origin of PNe morphologies and further shaping process are not well understood. The

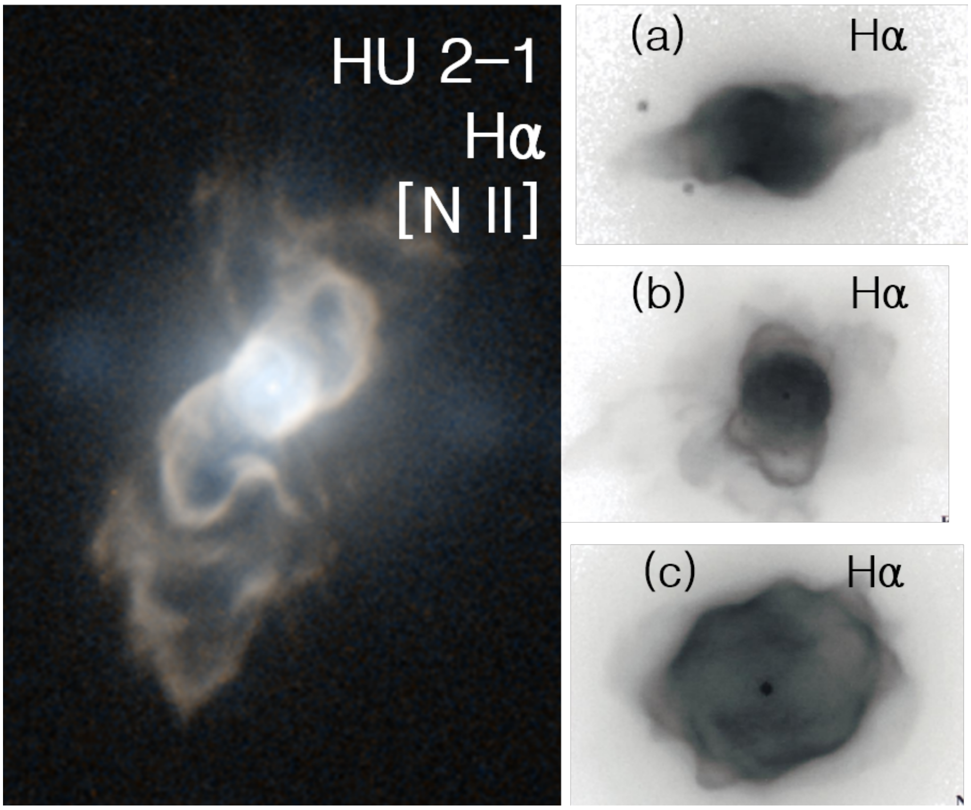

FIGURE 1.4: PNe that evade morphological classification schemes. Hu 2-1 (M. L. Humanson, Judy Schmidt, Mount Wilson Observatory); (a): M1-26, (b): He2-115 and (c): He2-138 (R. Sahai & NASA).

density distribution of shells in round PNe is well explained by the interacting stellar winds (ISW) models, where a fast stellar wind shocks the denser and slower material ejected during or just after the AGB phase, interacting hydrodynamically with it (Kwok et al., 1978). However, the ISW model fails to explain elliptical and bipolar PNe. So, the ISW theory was extended to the GISW model, to include aspherical environments (toroidal density distributions of dense material around the central region) in order to generalize it, and explain the bipolar and elliptical morphology (Icke, 1988; Icke et al., 1992; Soker & Livio, 1989; Mellema & Frank, 1995). The origin of these aspherical environments, able to generate an ambient shock that expands more quickly along the poles than the equator, is still a matter of conjecture. On the other hand, PNe with multiple pairs of lobes cannot be explained by GISW. To break the paradigm of the GISW about the shaping mechanism of PNe, multiple mechanisms and processes have been proposed. These mechanisms, individually or combined could explain the morphological diversity by considering several characteristics. As the presence of an stellar companion and the consequences of its binary interaction; the stellar rotation; presence of magnetic fields and where and when the star enters its final stage of evolution (Balick & Frank, 2002).

Chong et al. (2012) showed that complicated internal structures as knots, lobes, tori, ansae (two opposite bright knots along the major axis), S-shape and point-symmetric morphologies can be explained by a multipolar model. Following these authors the variation in inclination and position angle (PA) of the pairs of lobes, together with its shapes and sizes, could reproduce all the features at once, taking into account the orientation and sensitivity of the image techniques. Chong et al. (2012) also emphasize that the formation mechanism of multipolar lobes is not known. Precessing jets, coeval mass outflows and binary systems are postulated. Fig. 1.6 illustrates a number of tri-polar nebular models for different orientations, in comparison with observed images (Chong et al., 2012). The aim of that study was to demonstrate that the multipolar model works as a first-order approximation to the true morphologies of the selected objects.

Morphological and kinematic studies of PNe have been performed hand by hand. This is so, because the dynamical properties of the expelled material from the CS are fundamental in the nebular shaping process. PNe do not remain in a state of mechanical equilibrium and they must expand under the influence of the radiation pressure. The latter is due

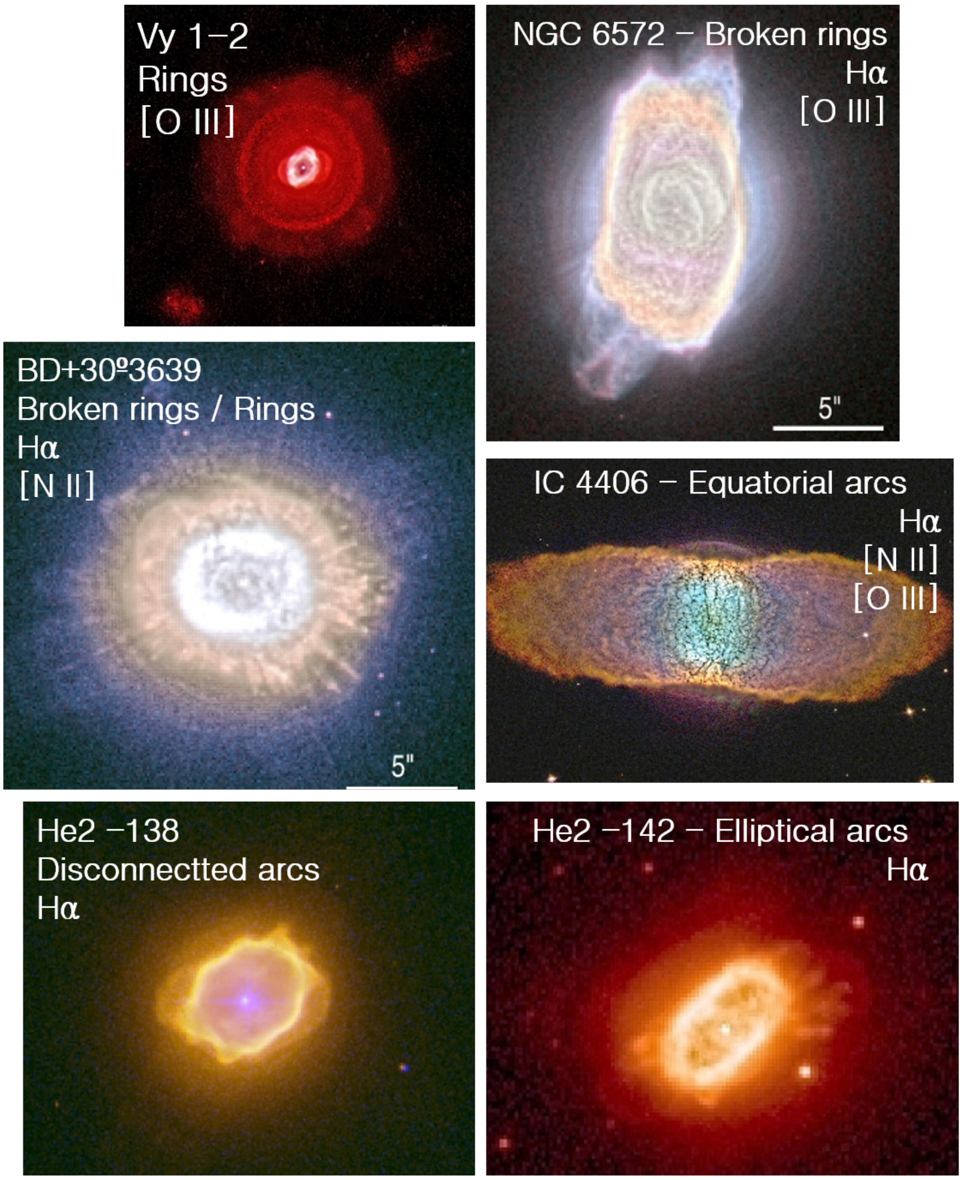

FIGURE 1.5: Examples of the classification scheme of concentric structures. Adapted from Ramos-Larios et al. (2016).

to the low density and size of the nebula, the weak action of the gravitational force, and the energy supplied by the CS through its radiation field and wind (Gurzadyan, 1997). High-dispersion spectroscopic studies showed that the emission lines are split at the central region of the nebula and their separation decreases continuously with the nebular radius, until it disappears at the apparent edge of the nebula (Osterbrock & Ferland, 2006). Such phenomenon is understood as the radial expansion of a nebula from its CS, with velocities of a few tens of km/s, which considerably exceed by a few orders of magnitude, the escape velocity of the CS at a distance of the ionized nebula (Gurzadyan, 1997). The fact that ions of the highest ionization potential have the lowest measured expansion velocity and vice versa, plus that the degree of ionization in a nebula decreases outwards, points out that the expansion velocity also increases outward. Even though, the expansion of PNe must be influenced by decelerating forces. The deceleration due to gravity and/or radiation pressure is almost negligible. The expansion of the nebula occurs in the interstellar medium (ISM), which has a non negligible density. The ISM prevents the material to move forward and results in decreasing velocities. Such decelerating mechanism is relevant when the nebula is large, hence, when the nebula becomes old (Gurzadyan, 1997).

The expansion of round, elliptical and some bipolar PNe is almost uniform, homologous and radial. Their expansion is faster along the projected symmetry axes, than in the equatorial plane (which is expected if they maintain their overall shapes as they evolve). This homologous expansion tends to grow linearly with the nebular radius (Hubble flows[1]) (Balick & Frank, 2002).

[1]jargon of the area

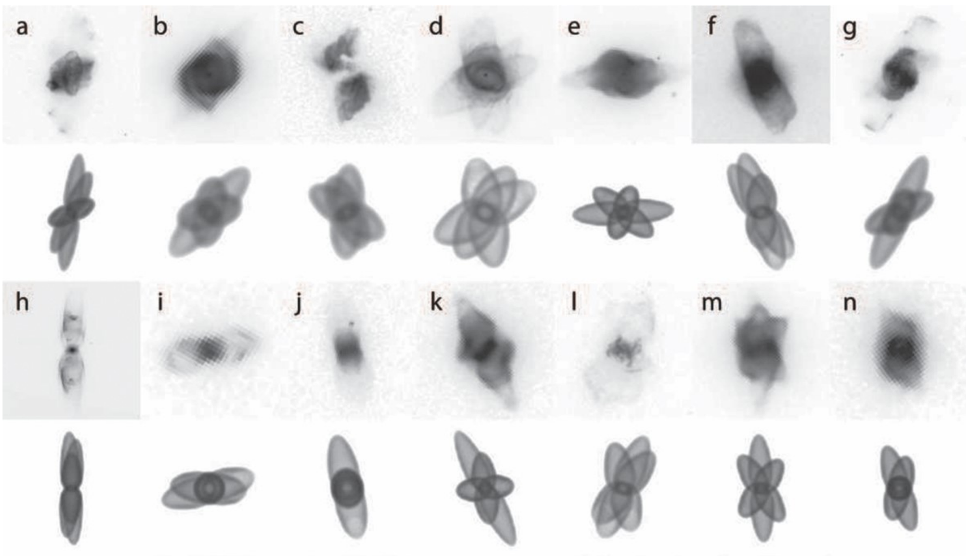

Figure 1.6: Comparison of observed PNe with a single tripolar model in different orientations. Adapted from Chong et al. (2012).

1.3 Distance to PNe

Calculate distance to PNe is difficult exercise and it is an active area of investigation nowadays. Traditional methods to estimate the distance to stars, rely on stellar properties and are not easily applicable to PNe. In a general point of view, none of the basic geometrical or physical parameters are constant for all PNe, and this complicates the distance determination. Unfortunately, distances to Galactic PNe are indispensable to determine their formation rate, Galactic distribution, space density distribution, total and ionized nebular masses, sizes, ages, luminosities and even the evolutionary states of their CS, among others (Kwok, 2007; Gurzadyan, 1997; Osterbrock & Ferland, 2006).

The techniques for calculating the distances to PNe can be divided in two types. The individual and the statistical methods (Jiménez, 2005).

1.3.1 Individual distances methods

These are independent and direct distance calculation to individual PN that usually present uncertainties around of 20% - 30% and can only be applied to nearby PNe.

Trigonometric parallax

It is one of the most direct ways to measure the distance of stellar objects, such as the CS of PNe. But it is limited by technology. Due to the orbital motion of the Earth around the Sun, an apparent shift of the position of the CS in the plane of sky appears, which is called parallax. For distant PN, the parallax is too small and high precision observations are required. Outstanding measurements are expected from GAIA survey in the early 2020s. A parallax precision of 6.7 microarcsec, proper motions to 3.5 microarcsec per year, and a distance accuracy around of 20% obtained up to 9.2 kpc away from the Sun are expected (ESA, 2016).

Spectroscopy distance

This method is based on the well-defined luminosity-spectral type relationship. More specifically, the absolute and apparent magnitude of a star are related with the logarithm of its distance, see Eq. (1.1) (Gurzadyan, 1997). By deriving the star absolute magnitude from the spectral type, which is determined by observing the spectrum of the star, and measuring the star's extinction corrected apparent magnitude, the distance of MS stars can be inferred. Such technique can be applied in the case of a binary system, for a resolved MS companion of the CS star (Kwok, 2007).

$$D = 10^{0.2(m-M+5-A)} \tag{1.1}$$

where m is the apparent and M the absolute magnitude of the star. A is the extinction and D the distance.

A variation of this method for CS of PNe is called model atmosphere (gravity) distances but it is not easily to apply (see, Eq. (1.2)) (Méndez et al., 1988). It is necessary to estimate the corrected CS apparent magnitude (V_0) by the effects of the interstellar extinction as well as the contribution of the nebular emission as well as calculate its CS mass (M_c). The CS's mass is obtained by comparing theoretical evolutionary tracks of CS surface temperature and gravity with its correspondent observed values. The observed surface temperature and gravity are derived from non-LTE line formation theory and high-resolution spectroscopy of H and He CS line profiles. The surface flux ($F_\star$) at λ5480 Å is derived from the apparent magnitude. One can see that a pure observational distance technique for MS stars gets model depended for PNe, being highly limited for bright CS.

$$D^2 \ \ [\mathrm{kpc}] = 3.82 \times 10^{-9} \frac{M_c \ [M_\odot] \ F_\star \ [\mathrm{erg \ cm^{-2}} \ s^{-1} \ \mathrm{\mathring{A}}^{-1}]}{g \ [\mathrm{cm} \ s^{-1}]} 10^{0.4V_0} \tag{1.2}$$

The apparent magnitude and surface flux used by these authors in this method are not general values. Another values can be used if are observationally available.

Extinction distances

From the foreground stars in the vicinity of a PN and the known extinction-distance relationship of these stars, the PN distance can also be determinated, if its reddening is known (Lutz, 1973). This method is almost confined to the Galactic plane. Outside the main Galactic dust layer, the distance could be underestimated. The method is also limited by the number of foreground stars in the vicinity of the PN (Phillips, 2006).

Cluster distances

For a PN that is a physical membership of a globular or open cluster, the distance is automatically estimated from the cluster's distance. The problem with this method lies in determining whether the the PN is a real physical membership of cluster or not. Frew et al. (2016) show that, so far, only 9 PNe are members of clusters. Several discussions are followed in literature to establish if a single PN is a physical membership of a cluster or not, by analyzing the position of the PN relative to the cluster and if both present similar systemic heliocentric velocities (Frew et al., 2016).

Distances from 3-D photoionization models

Distances can also be estimated by means of 3-D photoionization models. By modelling the physical parameters, the geometry (morphology) and size of the nebula, simultaneously with the CS properties, it is possible to constrain the nebular distance. A simplified 3D model structure can be derived from the images and velocities, over all the observed lines and density maps of the PN, therefore such a model represents all the geometrical nebular observations simultaneously. And, on the other hand, the CS luminosity and effective temperature, as well as the chemistry of the gas are tunned until the best fitting is achieved. This modelling process gives, as outputs, the ionizing source characteristics, the physical properties and chemistry of the gas and the object distance, all of them with a high internal consistence (Monteiro & Schwarz, 2007). This method has been successfully applied to determine the distances of a few planetary nebulae, as NGC 6369 (Monteiro et al., 2004), Menzel I (Monteiro et al., 2005) and NGC 6781 (Schwarz & Monteiro, 2006).

Expansion parallaxes

In the expansion parallax method, the PN distance is physically related with its tangential and angular velocities (see, Eq. (1.3)). Therefore, by measuring the angular expansion of a PN (angular velocity or proper motions) and assuming that its radial velocity is the same as the tangential velocity due to the assumption of PN's spherical symmetry, the distance can be calculated (Terzian, 1997). From high-dispersion spectra, the radial expansion velocity component can be obtained. The distance can be estimated assuming a constant expansion velocity and an equivalence between the angular expansion rate and the spectroscopically measured radial velocity by:

$$D \quad [\mathrm{kpc}] = 211 \frac{V_{\perp} \quad [\mathrm{km/s}]}{\dot{\theta} \quad [\mathrm{mas/yr}]} \tag{1.3}$$

where $V_{\perp}$ is the tangential expansion velocity and $\dot{\theta}$ is the proper motion (Terzian, 1997).

For instance, Reed et al. (1999) showed that the physical radial expansion velocity of a nebula obtained spectroscopically can be converted to tangential velocity by using a morpho-kinematic model of it. This approach was used because several regions in a nebula do not meet the requirement of having equal radial and tangential expansion velocity due to the loss of spherical symmetry Li et al. (2002).

Mellema (2004) has showed that the radial and angular velocity vectors of an expanding nebula do not correspond to the same component. In particular, the former refers to the expansion of the ionized gas behind the ionization front (which is called matter velocity) whereas the latter displays the angular expansion of the ionization front itself (which is called pattern velocity). A significant difference, up to 30% between the pattern and matter velocity has been found by these authors. This difference indicates that the calculated distances from the expansion parallax method are underestimated by this amount, and so they have to be corrected. For both, shocks and ionization fronts, the correction factor is around 1.2 to 1.3.

Later on, Schönberner et al. (2005) reached to the same conclusion, by using 1D hydrodynamical modeling: the pattern velocity is always larger than the matter velocity. They also shown that the correction factor varies between 1.3 and 3, depending on the evolutionary stage of the CSPN, see Fig. 1.7.

Hajian (2006) made a detailed review on the expansion parallax method, mentioning that besides the systematic sources of errors, the distance uncertainty does not exceed 25%.

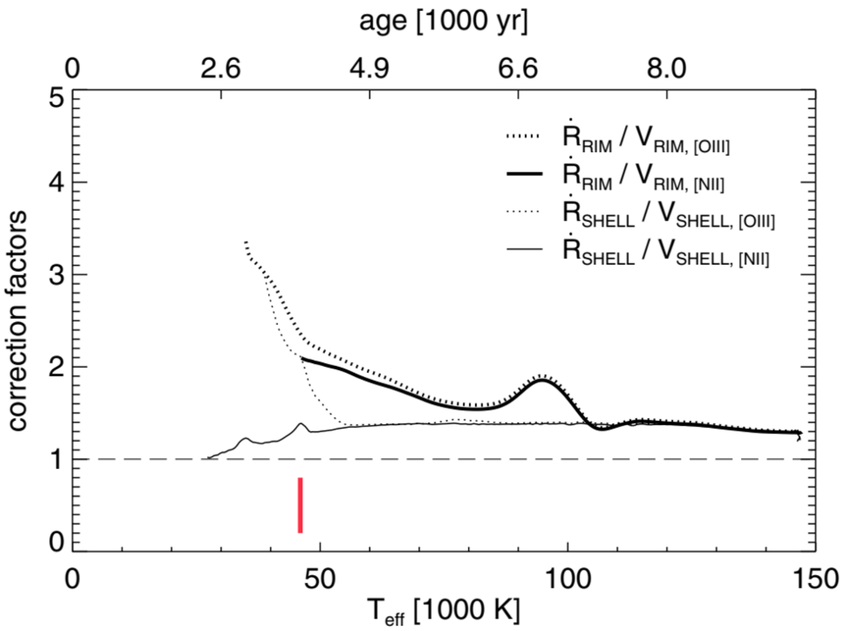

FIGURE 1.7: Correction factors, $F = \dot{R}/V$ versus the surface temperature of the CS of a PN. The red vertical line indicates when the ionization front passes the shock. Adapted from Schönberner et al. (2005).

1.3.2 Statistical methods

These methods rely on certain particular assumptions about the nebular structure and properties. The difference between the statistical and the individual distances can be of a factor of 2 or even higher (Jiménez, 2005).

The constant mass relation

The ionized mass of a nebula can be calculated from its total irradiated energy (its luminosity) and its size (volume). The luminosity of a nebula in a given emission line is a function of the flux in that emission line and the distance of the nebula. The radius of the nebula is also related with its angular expansion and distance. Hence, the volume depends on the angular expansion and distance too. Hence, the total ionized mass of the nebula could be expressed in terms of its distance, angular size and flux. This implies that the distance to PN can be calculated if its total ionized mass, flux and angular size are known (Gurzadyan, 1997). Shklovsky (1956) used this relationship under the assumption that the total ionized mass is constant for all PNe, due to its weak dependency on distance. Recently, a distance catalogue of several PNe distance scales, that rely on this method, and on further modifications of it, was presented by Frew et al. (2016). These authors also remark that the distances based on these constant-mass scales are overestimated for young PNe, and underestimated for the largest evolved PNe.

The mass-radius and temperature-radius relationships

These two methods were derived from the Shklovsky method with some modifications. The mass-radius relation states that the mass is a continuous function of the radius (Pottasch, 1980). Van de Steene & Zijlstra (1994) proposed a second relationship based on the brightness temperature-radius relationship and the radius of PNe. Both are empirical relations, whose constants and power-law indexes are highly debatable in the literature (Frew et al., 2016).

The "emission line" and surface brightness-radius relations

Frew et al. (2016) describe in details these two methods. Both methods require the knowledge of the angular size of PNe, the integrated flux of an emission line and the reddening of PNe. An intrinsic radius is calculated from these quantities, which is then combined with the angular size, in order to derive the distance. the Hα emission line is preferred over the [O III] or [N II], because it includes bright and old PNe, over a broad range of excitation, and better estimates the ionized mass (Frew, 2008; Shaw et al., 2001). Hα line is also preferred over the Hβ, because it is approximately 3 times brighter. The Hα-radius relation appears to be a robust statistical distance, with a distance dispersion of $\pm 28\%$ (Frew et al., 2016).

1.4 3D morpho-kinematic modeling of astrophysical nebulae

The deduction of the physical properties of astrophysical objects can be achieved by physical modeling, using a set of limited constrains (Steffen et al., 2011). Traditional softwares related with the reconstruction and 3D modeling of astrophysical nebulae are specialized in modeling particular aspects, such as the molecular radiation transfer, the photoionization or the geometric structure (Steffen, 2016). An example of such softwares is MOCASSIN, a fully 3D Monte-Carlo radiation transfer code that accepts as input parameters any gas distribution and dust density on a cartesian grid, which was developed by Ercolano et al. (2003). It accepts the outputs of hydrodynamic models (Monteiro & Falceta-Gonçalves, 2011), or the outputs from 3D morpho-kinematic models (Akras et al., 2016).

Nowadays the constructive morpho-kinematic modeling approach, which involves only structural (morphological) and velocity (kinematic) information is widely used. Due to the availability of high-resolution imaging and high dispersion spectroscopy for several nebulae. Such measurement are fundamental to constrain the kinematics and morphology of the nebular models.

The SHAPE software is then presented as a 3D morpho-kinematic code that can reconstruct and model, interactively, the structure of an astrophysical object in three dimensions (Steffen et al., 2011). The software contains a 3D modeling view to define the geometry and behavior of the model as well as a two-dimensional view, for a comparison of the simulated features with the observational data. Among the SHAPE most relevant features are the following:

- it combines in the same system the visualization and analysis of the model, and allows to access the model data at any stage of the process;
- it allows to refine the model parameters by direct comparison between the observations and the model predictions until a qualitatively fitting its achieved;
- It can import data from external simulations for visualization and analysis of the results.

SHAPE models are constructed with 3D elementary mesh components (spheres, cylinders, etc). There are based on some assumptions about the morphology and geometry of the object, together with the velocity field and surface brightness derived from observations. The mesh component properties can be modified in several ways, with a variety of preloaded SHAPE functions (modifiers), without the need of programming. The modeling process follows, in general, these 3 steps (Steffen et al., 2011):

1. To select a region in the spatial domain and the elementary mesh components. Multiple components can be used in order to reproduce more complex models and in different spatial scales.
2. To give physical or kinematic properties to each mesh component as a function of position in the spatial domain. It is allowed to use different functions for different substructures.
3. To read the previous physical and kinematical properties of each mesh component to generate the results.

SHAPE has been tested and applied for a variety of scientific research projects[2]. For a more detailed modeling procedure see Steffen et al. (2011), and the software website[3].

[2]http://www.astrosen.unam.mx/shape/v4/publications/scroll/publications.html
[3]http://www.astrosen.unam.mx/shape/index.html

2

The Distance Mapping Technique - DMT

As a novel variation of the expansion parallax, the DMT proposed by Akras & Steffen (2012) is presented here. This technique deals with a kinematic analysis and a distance calculation. It is able to constrain morpho-kinematic models of expansion nebulae and determine their distance, by using the assumption of modeled velocity fields and the observed proper motion vectors.

In the expansion parallax methodology, a tangential velocity component and an angular expansion rate are used to calculate the distance of an expanding nebula, under the relationship in Eq. (1.3). The novelty of the DMT is the multiple application of Eq. (1.3), in different regions of the nebula, to create a distance map. The distance to a nebula comes from the average of the non-zero values in the distance map. An error map is also provided by the DMT. Along with the distance map, the error map therefore shows the distance error in the different regions of the nebula. The error in each region of the nebula, and the total error of the nebular distance, are calculated following the error propagation methodology. In the absence of observational errors for the measured proper motions, the distance error represents only the intrinsic uncertainty of the DMT.

The main inputs and outputs of the DMT are represented in the flow diagram of Fig. 2.1. The most important inputs are the set of tangential velocity vectors and the set of proper motion vectors. The former is derived from a morpho-kinematic model of the nebula –the three-dimensional morpho-kinematic code SHAPE is a good example of a software used to create those models– the latter are measured from two observed images obtained in two different dates (Hajian, 2006). The primary outputs are the distance and the error maps.

If the modeled tangential velocity field matches the observed angular expansion rate (proper motions) then, homogeneous distance and error maps are expected. Otherwise, some regions of the maps will present several deviations from the mean distance value and the homogeneity of the maps will be lost. Such deviations in distance cannot be interpreted as nebular regions that lie closer or further away from us, because the distance error is higher than the average size of a nebula. Several adjacent cells in the distance map could present similar distance deviations from the mean value, and in that case, this group of cells is considered as a systematic distance deviation (SDR). These SDR regions indicates a localized divergence between the modeled and observed velocity fields. This divergence could be related to additional physical phenomenon in the nebula, which

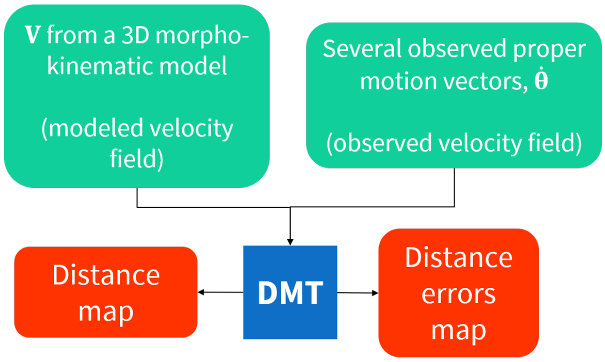

FIGURE 2.1: General inputs (green) and outputs (orange) of the DMT.

escape from the assumptions of the morpho-kinematic model, or could even point out a problem with the measured proper motions.

The next sections will represent how the DMT works, outlining both the inputs and outputs. Then, a statistical study of the DMT will be presented.

2.1 DMT methodology

The main input information in the DMT are the observed proper motions and the modeled tangential velocity field. These data sets must specify the coordinates and magnitude of the vectors. The size of the DMT map (i) must be specified in order to define the working region. "i" has to be large enough to include the whole nebula as well as all the velocity vectors. The DMT will cover all the working region discreetly, cell by cell. The size and the number of the cells (n) are related with the resolution (re), which the user must specify. As long as the cell contains both proper motion and tangential vectors, the DMT will apply the expansion parallax formula in each cell. Then, the distance errors are calculated using the error propagation methodology. Therefore, after covering the entire working area, the distance and error maps are generated. The distance (D) and error (E) of the nebula are calculated from these maps. Finally, the distance and error maps are printed together with their histograms, as well as a data table.

2.1.1 Technical details of the DMT

The DMT code has received several updates in this thesis, since its first version by Akras & Steffen (2012):

- the DMT code was initially written in FORTRAN. It has now been rewritten in PYTHON;
- it is now possible to add observational errors from observed proper motion vectors, and take them into account in the calculation of the distance uncertainty;
- it calculates and prints the standard deviation and the coefficient of variation for the distance and the error maps;

- it is possible to exclude outliers from the maps, based on the modified Z-score criterion;
- it prints the histogram for both maps;
- information about the map, the targets, the final distance and error, as well as the resolution of the maps are provided;
- the color bar includes a legend indicating the units;
- by default the color maps of the distance and error maps are different;
- it is possible to choose different color maps for distance and error maps from a large set provided by the Matplotlib color maps reference;
- it is included in the top and left borders of the maps, a counting of the cells.

The inputs of the DMT are:

- the modeled tangential velocity field and the observed proper motions: the data set must contain the coordinates and the velocity component magnitudes in RA and Dec, with the central star of the nebula being the reference point. The tangential velocity vectors must be given in km/s and while the proper motions in mas/yr;
- the observational errors of the proper motion vectors (optional): the data set must contain the coordinates and uncertainty magnitudes in RA and Dec, with the central star of the nebula being the reference point. The uncertainty must be given in mas/yr;
- the size of the image of the object ($\imath$): in arcseconds;
- the resolution ($\mathscr{re}$) of the maps: it is applied to both distance and error maps. $\mathscr{re}$ is related with the size $\imath$ [arcsec] and the number of square cells of the map (n [cells/dimensionless]) by

$$\mathscr{re} = \frac{\imath}{n} \quad \text{[arcsec]} \tag{2.1}$$

  in some cases, it may be necessary to be given different resolution per axis. In that case, the size of the image in RA direction ($\imath_{RA}$) is different from the one in Dec direction ($\imath_{Dec}$), which implies a specific resolution for RA and Dec direction:

$$\mathscr{re}_{RA} = \frac{\imath_{RA}}{n} \quad \text{and} \quad \mathscr{re}_{Dec} = \frac{\imath_{Dec}}{n} \text{ [arcsec]} \tag{2.2}$$

  one can define $\mathscr{re}$ or can specify the number of the cells, n (optional);
- outliers exclusion (optional): in the default mode outliers are not excluded. The DMT finds the outliers using the modified Z-score method (Iglewicz & Hoaglin, 1993) where a data point is described in terms of its relationship with the median absolute deviation (MAD) and the median value;

- color map for distance and error maps (optional): the default will be applied in case of no selection;
- object's name: the name of the nebula that will be displayed in the maps, histograms and data tables.

And the DMT outputs are:

- distance and error maps: they are colored maps containing as a title, the map's resolution in arcsec, the object name, and the corresponding final distance and error value in kpc or pc;
- histogram with Gaussian fits for the distance and error maps: Also presents the map's resolution and the corresponding standard deviation of the distance and error maps. If the outliers are excluded, they does not appear in the histograms;
- data table: a table is printed showing the name of the object, the resolution of the maps, the distance, the error, the standard deviation and the coefficient of variation of distance and error maps.

2.2 A statistical study of the DMT

Not only one pair of distance and error maps can be generated for a given nebula, upon the variation of some input parameters. As long as the relationship of the input parameters with the distance calculation of the DMT is known, the optimal pair of maps, as well as, the optimal distance estimation of the nebula, can be found. There is a problem, however, related with the following input parameters:

- the resolution ($\mathscr{re}$);
- number of vectors ($\mathscr{q}$)

and, from the morpho-kinematic model:

- the inclination angle ($\mathscr{In}$);
- the deviation from the position angle ($\mathscr{d}PA$).

These parameters do not have a known relationship with the distance calculation of the DMT. Therefore, a statistical study is necessary to find out the relationship between these inputs and the DMT.

It is important to clarify that, from the 3D morpho-kinematic models, there are also other variables, such as the assumptions made for modeling the nebular morphology, the kinematic law, and the particle density of the 3D model among others, which will increase the diversity of the DMT maps. The good news is that these variables are related to the DMT calculation through the expansion parallax technique and the distribution of the projected 3D model in a 2D area of the DMT maps.

2.2.1 Statistical study methodology

To perform the statistical study on the DMT, synthetic tangential and proper motion velocity fields are needed. Data sets of synthetic tangential velocity vectors (set A, hereafter just A) were derived from SHAPE models of spherical and bipolar nebulae (see, Fig. 2.2). For both models a single velocity expansion law was used.

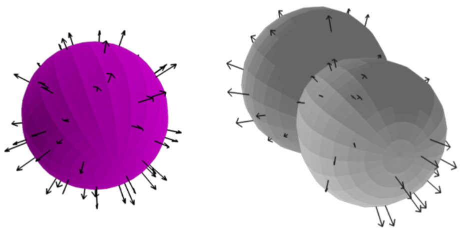

FIGURE 2.2: Spherical (*left*) and bipolar (*right*) SHAPE models used in the statistical study.

In order to create the synthetic proper motion data sets (sets B, hereafter just B), the tangential velocities (A) are used assuming a distance of 1 kpc, plus a random number (R), for both geometries (spherical and bipolar), by means of a variation of the Eq. (1.3):

$$\dot{\theta} \; = 211 \frac{V_{\perp}}{D}$$

where

$$D = 1 \; [kpc] + R$$

then,

$$\dot{\theta} \; [mas/yr] = 211 \frac{V_{\perp} \; \; [km/s]}{1 + R \; [kpc]} \tag{2.3}$$

where R is a random positive decimal number, which is added to the data set (A) in order to differentiate between data set (A) and (B). The synthetic proper motion data sets (B) are constructed applying the Eq. (2.3) to every value of the tangential velocity data set (A). Every time that the Eq. (2.3) is applied, the random number (R) is randomly selected from an interval that goes from 0 to $\mathscr{r}$. Then, $\mathscr{r}$ is the upper limit of the random number. Both R and $\mathscr{r}$ are parameters that does not have any physical interpretation. They are introduced in the study because of the method chosen to generate the synthetic proper motion data set. Any possible relation between $\mathscr{r}$ and the DMT distance calculation is unknown and it must be also investigated in order to separate its effect from the others parameters involved in the study.

The parameter $\mathscr{re}$ will be evaluated in terms of the number of cells ($\mathscr{n}$) of the map, while the image size ($\mathscr{i}$) remains constant. Although $\mathscr{re}$ was evaluated in terms of $\mathscr{n}$, and not in terms of $\mathscr{re}$ (arcsec) itself, there is a formula between them giving by Eq. (2.1). Since the SHAPE models were made with a grid size of 128 cells (its default value), we also want to know what happens if $\mathscr{n}$ is smaller, equal and higher than the grid size of the 3D morpho-kinematic models.

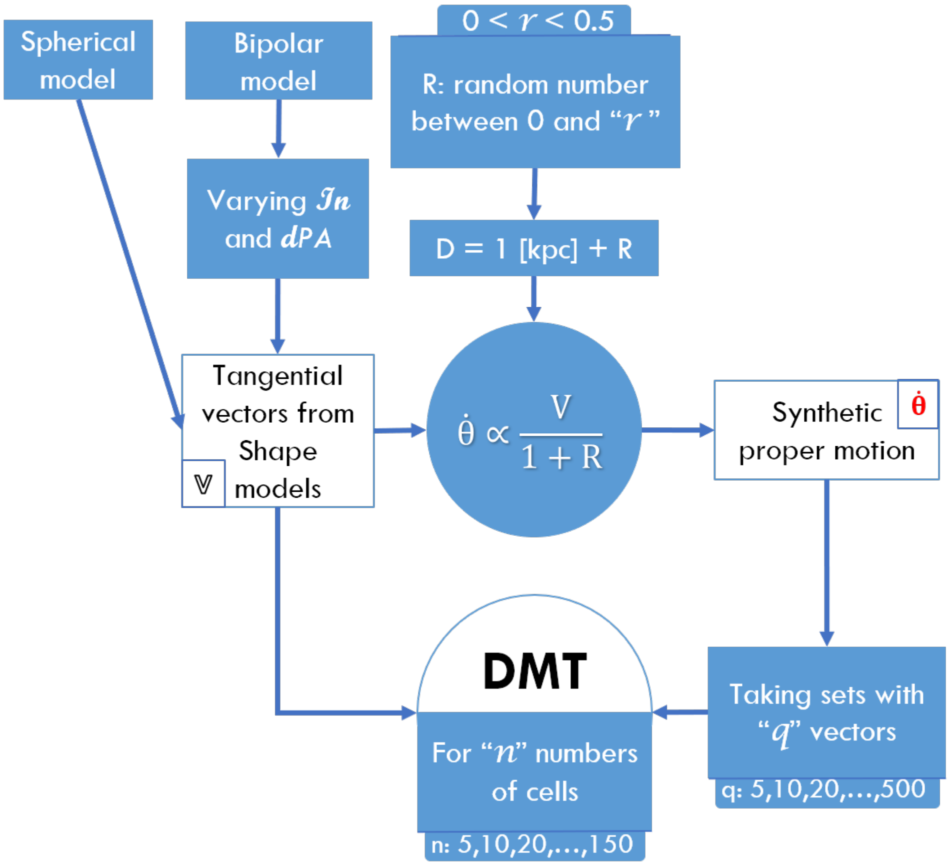

FIGURE 2.3: A general vision of the process followed to develop the statiscal study.

Another variable that it is worth to be studied is the number of velocity vectors (proper motions) (q). Understanding how the number of vectors affects the distance calculation of the DMT is crucial, because there is always a limited number of observed proper motion vectors. Since the synthetic proper motion vectors (B) were created as a variation of the synthetic tangential vectors (A), we randomly selected data sets of 5, 10, 15, 20, 30, 40, 50, 60, 70, 80, 100, 150, 200, 300, 400, 500 tangential vectors from the data sets (A); which were eventually converted to synthetic proper motion vectors using Eq. (2.3). 500 vectors were chosen as the upper limit, because the observed proper motion vectors are always restricted to a certain amount, and generally are below 500.

Taking advantage of the multiple functions of the SHAPE models, it is also possible to generate data sets A and B for different values of inclination angle ($\mathcal{J}n$), for the case of the bipolar model. The aim is to test the effect of the inclination angle in the distance calculation of the DMT. Another test includes exploring the effects on distance calculation, when there are deviations in the position angle (dPA) of the bipolar SHAPE models. The original PA of the models is PA $= 0°$.

Several distance deviations from the reference distance (1 kpc) on the DMT maps are expected by varying the geometry (spherical and bipolar), the inclination angle ($\mathcal{J}n$), the upper limit of the random number (r), the number of cells (n) and the number of vectors (q). By studying such distance deviations we expect to understand how all these variables affect the DMT. The flow diagram in Fig. 2.3 resumes the principal process needed to made the statistical study. Tangential velocity vectors are derived from spherical and bipolar SHAPE models, to provide one of the principal inputs of the DMT and obtain the synthetic proper motion vectors. Then the DMT was executed several times for every value of the secondary input parameters on testing ($\mathscr{n}$, $\mathscr{q}$, $\mathscr{In}$ and $\mathscr{d}PA$) and for the additional variable, $\mathscr{r}$, due to the nature of the study.

The methodology used to perform the statistical study is described in detail through the next four sections, with the aim to constrain the mentioned parameters as well as contrast the results of different geometries. In each case the data collected is composed of data tables: (per geometry); distance and errors maps, with their corresponding histograms; and plots made from the data tables. Note that multidimensional plots are presented in two perspectives, e.i. Fig. 2.12 for better appreciation.

2.2.2 Constraining the upper limit of the random number, $\mathscr{r}$

In the statistical study, every parameter is assumed to have an independent effect on the distance deviation from the reference value of 1 kpc. The study begins constraining the upper limit of the random number ($\mathscr{r}$), since we don't know which is the appropriate value for $\mathscr{r}$ or how it is related with the deviation from the reference distance.

On the other hand, the variation of the inclination angle ($\mathscr{In}$), a parameter related with the morpho-kinematic models, is tested along with the other parameters of the study, and only for the bipolar model. In the spherical model it is only tested the respective parameter –in this case $\mathscr{r}$– because of its spherical symmetry, there is not variation with $\mathscr{In}$.

To constrain $\mathscr{r}$, the rest of the parameters ($\mathscr{q}$ and $\mathscr{n}$) are considered constant. For instance, all the vectors of the synthetic tangential and proper motion data sets are used for this study, whereas the number of cells was chosen to be a $\mathscr{n} = 50$. The first part was executed as follows:

- a set of tangential velocity vectors was generated from the spherical SHAPE model;
- sets of tangential velocity vectors were generated from the bipolar SHAPE model, for different orientations, with $\mathscr{In}$= 0, 15, 30, 45, 60, 75, 90°;
- sets of synthetic proper motion vectors were generated, for both geometries using 5 different random number upper limit values, $\mathscr{r}$, equal to 0.05, 0.1, 0.2, 0.3 and 0.5;
- the DMT was executed for all $\mathscr{r}$ values in the spherical case and all $\mathscr{r}$ plus $\mathscr{In}$ values in the bipolar case.

In the Fig. 2.4 are presented the distance maps (left), the error maps (middle) and the histograms of distance and error maps (right), varying with $\mathscr{r}$ for the spherical case. Fig. 2.5 presents the same information for the bipolar model, but only for the $\mathscr{In} = 45°$. For both geometric cases, the higher the $\mathscr{r}$ value, the less homogeneous the maps. The distance from the reference value (1 kpc) deviates further, the errors increase, as well as the dispersion of the distribution in the distance maps.

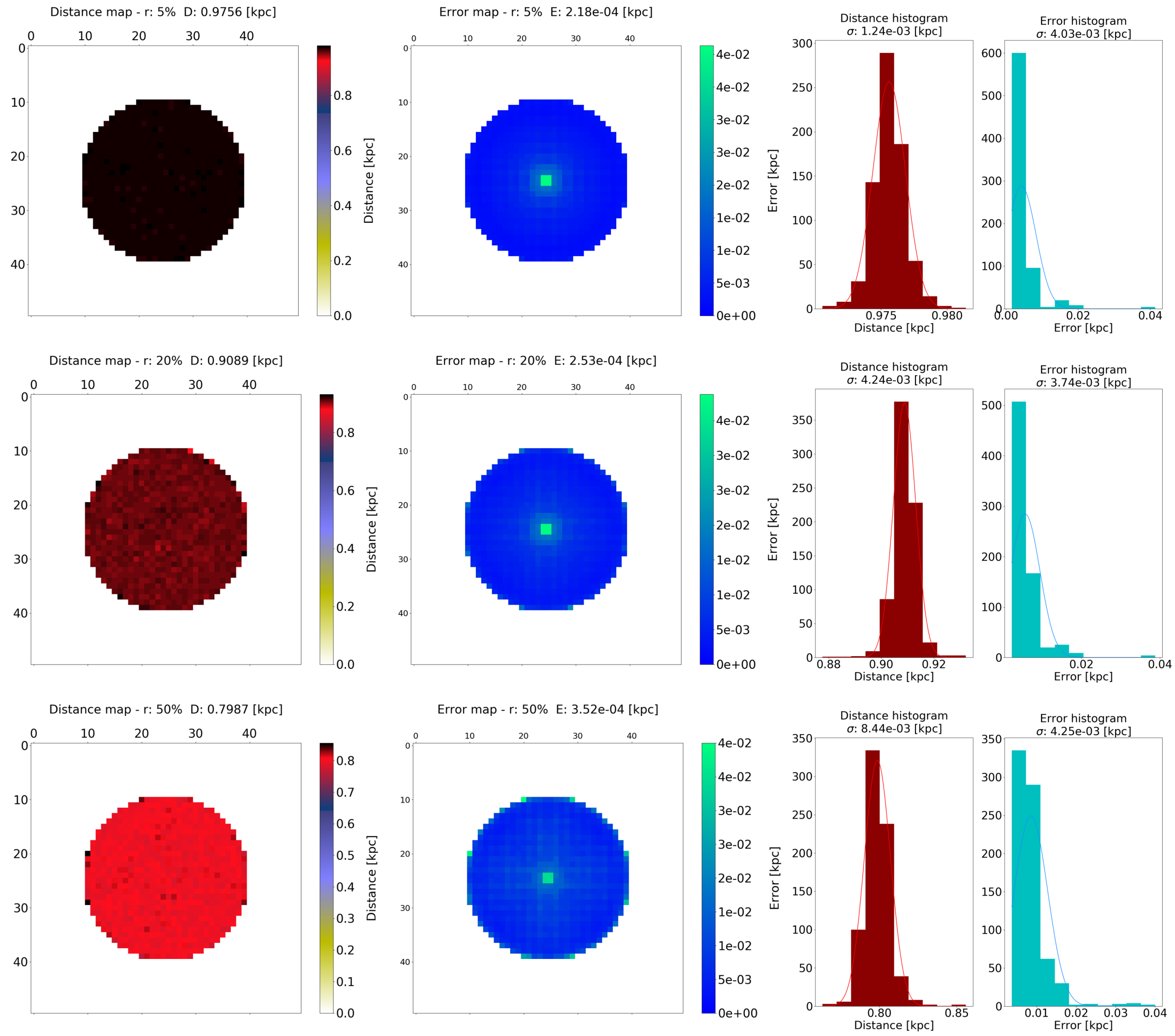

FIGURE 2.4: Distance maps (*left*), error maps (*middle*) and histograms of the distance and error maps (*right*), as a function of $\mathscr{r}$, increasing from top to bottom, for the spherical case.

The distance (D) and its error (E) are plotted against $\mathscr{r}$ in Fig. 2.7, with the aim to find the relationships that link these variables. Two different plots are presented, one for the spherical model (upper panel) and one for the bipolar model (lower panel). With the purpose of focusing solely on the distance and its error relationships with $\mathscr{r}$ in the bipolar case, an average distance, over $\mathscr{In}$ for each $\mathscr{r}$ ($D_{\mathscr{In}}$) is derived. The propagated error of the average distance ($E_{D_{\mathscr{In}}}$), along with the standard deviation of the average distance ($\sigma_{D_{\mathscr{In}}}$) are also calculated, and plotted against $\mathscr{r}$ (lower panel of Fig. 2.7). It is also presented a detailed view of the variability of D and E with $\mathscr{In}$, for the bipolar case, in a 4D plot (see, Fig. 2.6).

Both Figs. 2.6 and 2.7, show that D tends to decline (gets more deviated from the reference value (1 kpc)) whereas E tends to grow with $\mathscr{r}$, in both geometric cases. For the bipolar case, the variation of D and E presented with $\mathscr{In}$ in Fig. 2.6 is inappreciable, while Fig. 2.7 shows that the distance dispersion due to the variation with $\mathscr{In}$ is small and tends to grow with $\mathscr{r}$.

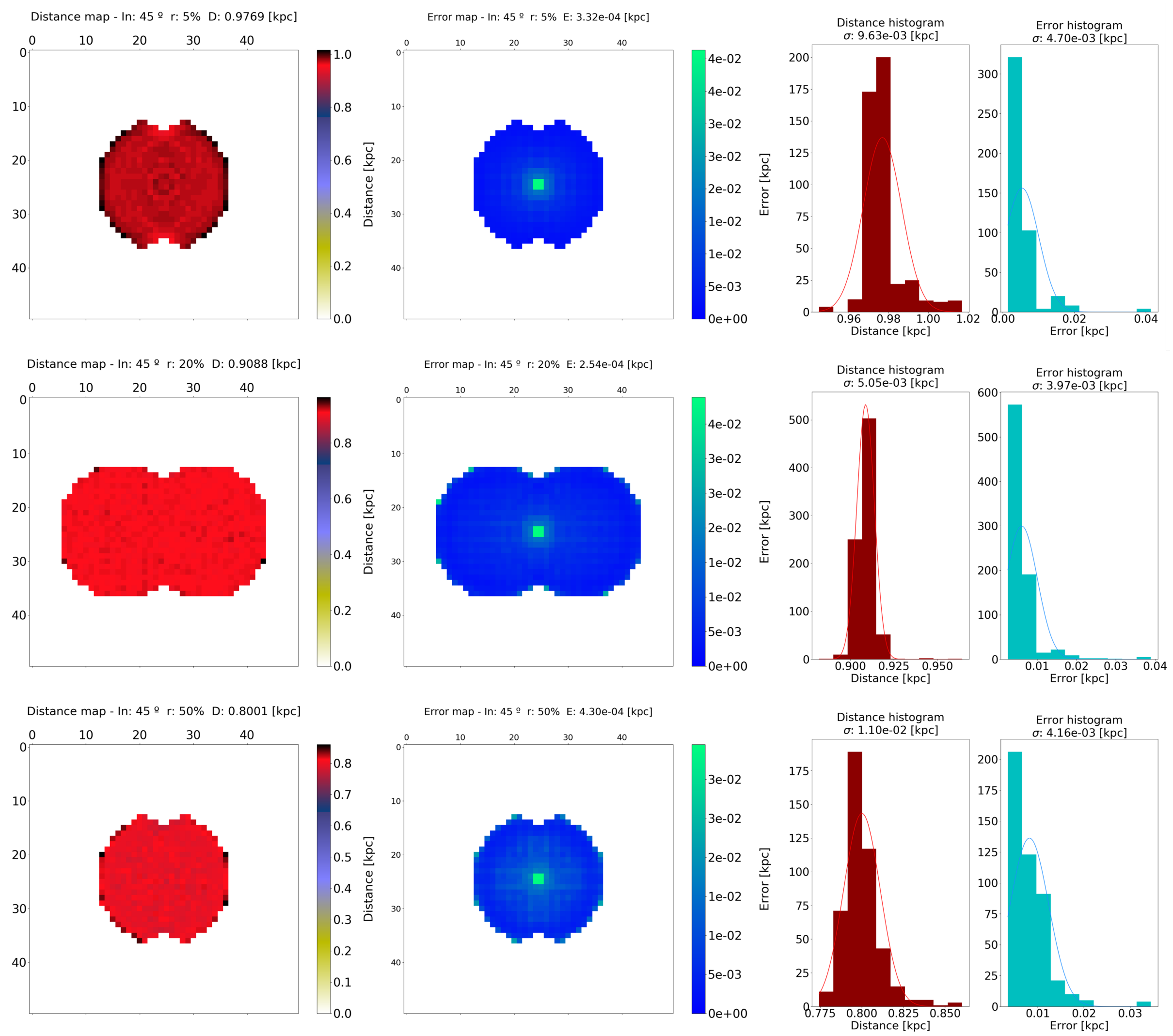

FIGURE 2.5: As in Fig. 2.4, but for the bipolar case, with $\mathscr{In} = 45°$.

The relative distance error, respect to the reference value of 1 kpc is $\delta D = \frac{abs D_{sim} - D_{ref}}{D_{ref}}$, where D_{sim} is the distance simulated in every case and D_{ref} is the reference distance. The distance error fraction (E/D) for the spherical (upper panel) and bipolar (lower panel) models, are also plotted against $\mathscr{r}$, (Fig. 2.8). A linear fitting for these variables is also presented. The linear fitting is really good for both geometries and variables, δD and E/D. Also, it is almost quantitatively equal for both geometries.

The statistical studies presented above lead us to the following conclusions:

- a systematic distance deviation from the 1 kpc reference value is found to be related with the upper limit of the random number ($\mathscr{r}$). The distance deviates at approximately 39% per $\mathscr{r}$ value in both geometric cases;
- the distance error systematically increases in about 0.05% per $\mathscr{r}$ value, in both geometric cases;
- the distance map dispersion, due to variation with the inclination angle ($\mathscr{In}$), is almost negligible (see, Fig. 2.6);

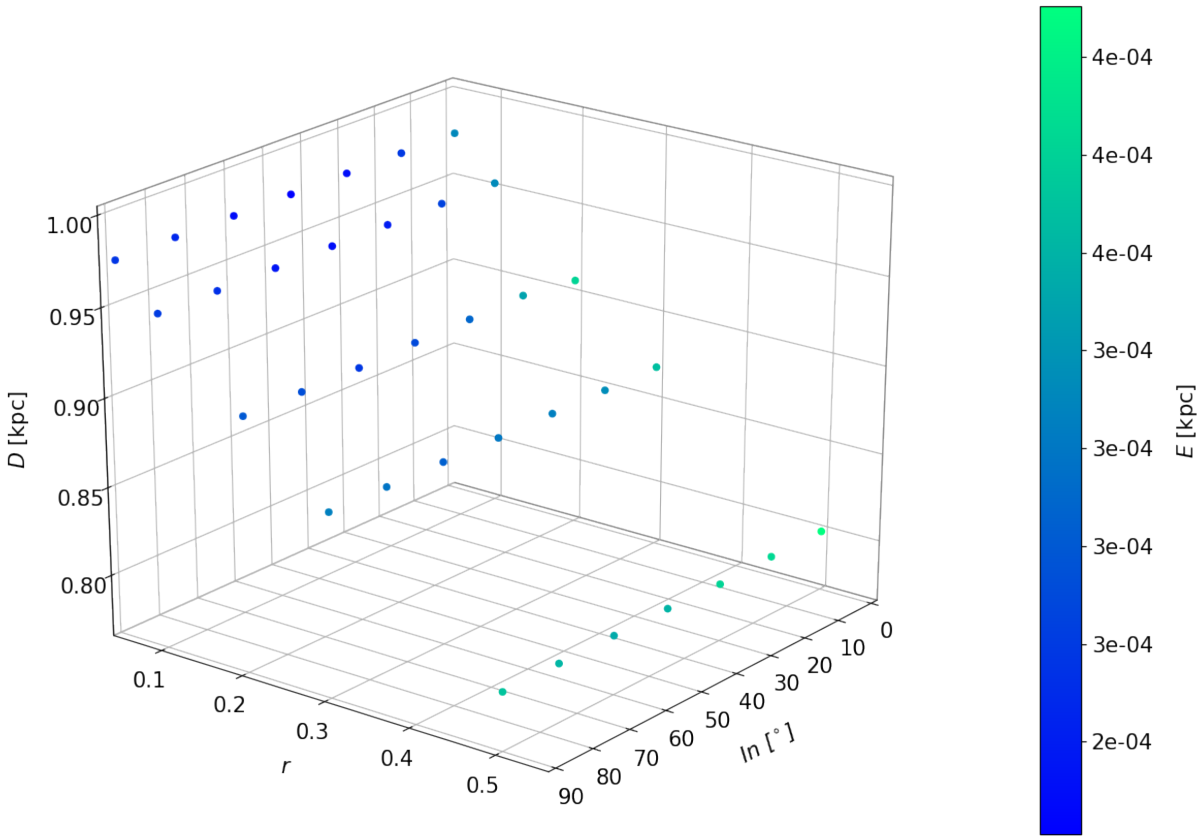

FIGURE 2.6: The distance D (z axis) as a function of $\mathscr{r}$ (y axis) and $\mathscr{In}$ (x axis). The color code gives the value of the error (E).

- qualitatively this analysis shown that the geometry of the modeled nebula does not affect the distance and errors derived by the DMT.

After analyzing the effect of $\mathscr{r}$ in the DMT calculation, we continue with the remaining variables, by setting $\mathscr{r} = 0.5$ for the rest of the study[1]. So, synthetic proper motions, for the rest of the statistical study are generated with $\mathscr{r} = 0.5$. By selecting this value for $\mathscr{r}$, the reference distance of 1 kpc is changed for the rest of the statistical study to 0.8 $\pm\ 1.4 \times 10^{-4}$ kpc.

[1] Value selected by authors preference.

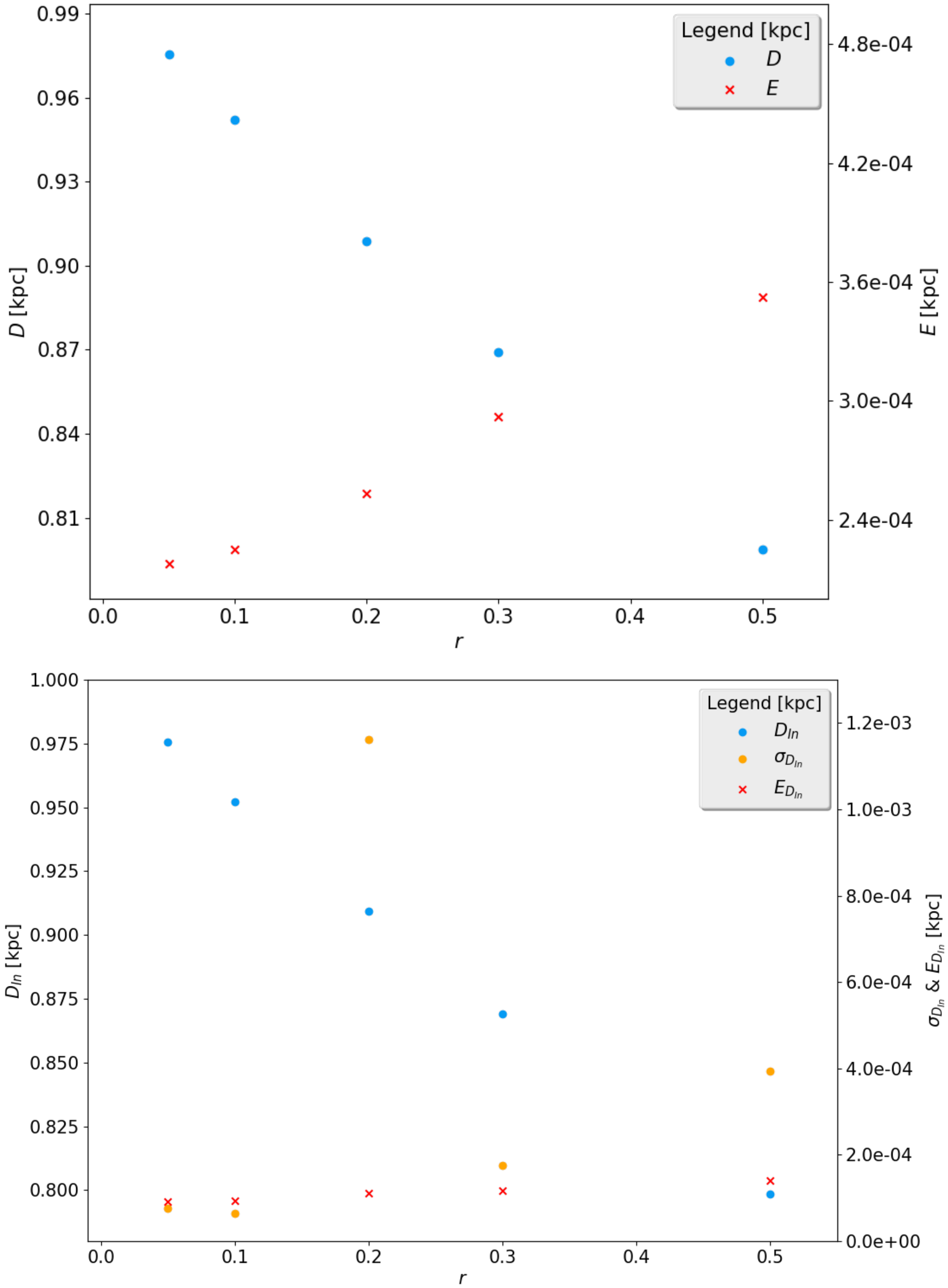

FIGURE 2.7: *Upper panel*: the distance D (blue points, left vertical axis) and error E (red x, right vertical axis) as a function of r, in the spherical case. *Lower panel*: the averaged distance over $\mathscr{I}n$ $D_{\mathscr{I}n}$ (blue points) on the left vertical axis, and, on the right vertical axis are the propagated error of this averaged distance $E_{D_{\mathscr{I}n}}$ (red x), plus the standard deviation of this averaged distance $\sigma_{D_{\mathscr{I}n}}$ (orange points) as a function of r.

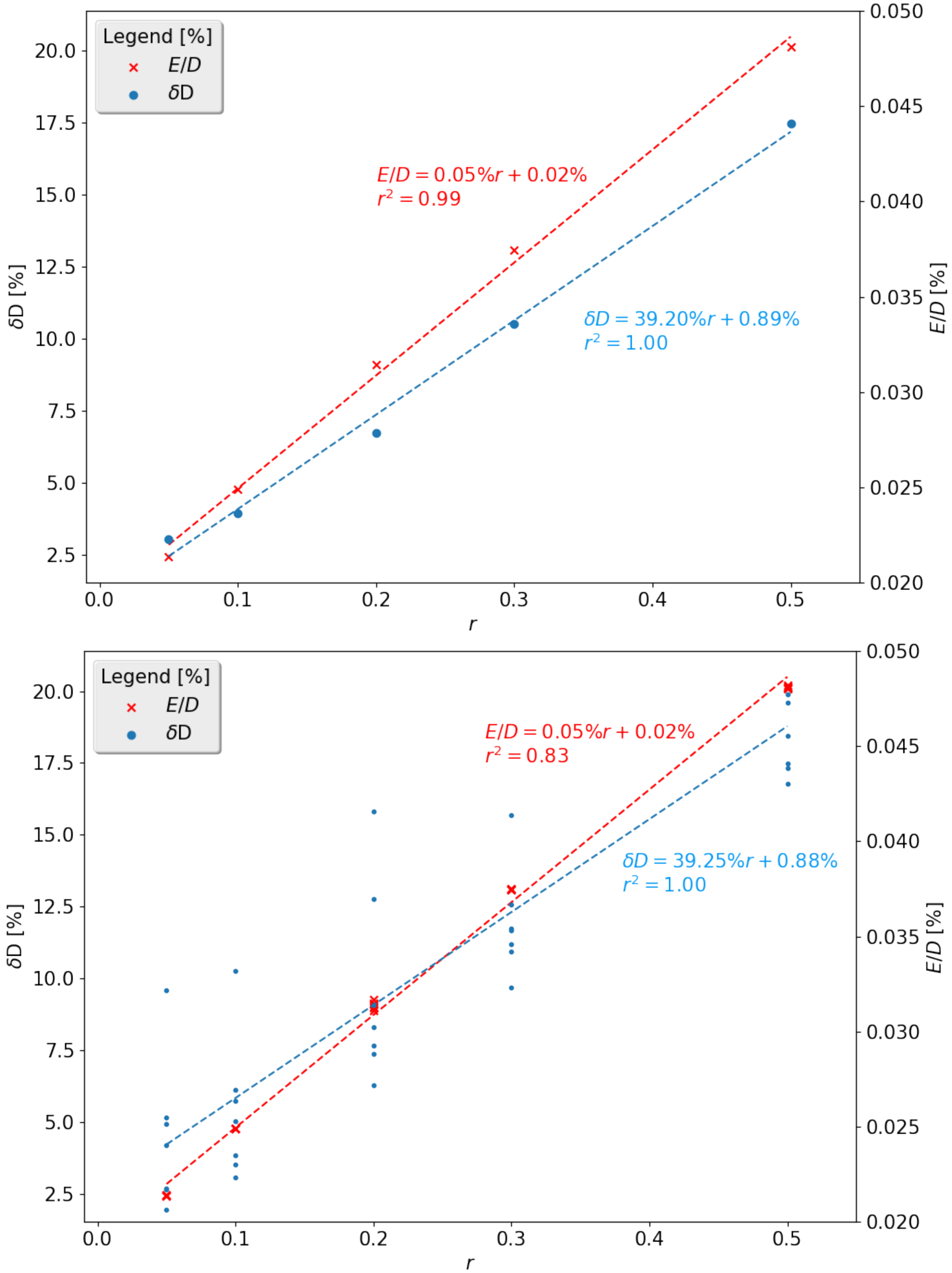

FIGURE 2.8: *Upper panel*: linear fit for the relative distance error, δD (blue points, left vertical axis) and the distance error fraction E/D (red x, right vertical axis) as a function of $\mathscr{r}$ in the spherical case. *Lower panel*: linear fit for δD (blue points, left vertical axis) and E/D (red x, right vertical axis) as a function of $\mathscr{r}$ in the bipolar case.

2.2.3 Constraining the map resolution parameter, $\mathscr{re}$

The second part of the statistical study of the DMT has the objective to explore how the resolution affects the DMT distance. In order to constrain $\mathscr{re}$, the number of cells ($\mathscr{n}$) is used, setting a constant image size ($\mathscr{i}$) through the study. It is possible to evaluate $\mathscr{re}$ in terms of $\mathscr{n}$ because of their inversely proportional relation in Eq. (2.1). The parameters ($\mathscr{r}$ and $\mathscr{q}$) are considered constant. $r = 0.5$ as selected in the previous section and all the synthetic proper motion vectors are used. The second part is executed as follows:

- the tangential velocity vectors data set, generated by SHAPE in the first part, were used for both models (spherical and bipolar);
- the synthetic proper motion vectors data sets were generated, for both geometries, by using a random number upper limit value, $\mathscr{r} = 0.5$ (Section 2.2.2);
- various number of cells, $\mathscr{n}$, have been selected for this part of the study: 5, 10, 20, 30, 40, 50, 60, 70, 80, 90, 100, 128, 129 and 150 cells. 128 cells correspond to the grid size of the SHAPE models;
- the DMT was executed for each value of $\mathscr{n}$ (spherical case) and for each $\mathscr{n}$ plus $\ell\mathscr{n}$ value (bipolar case).

Figs. 2.9 and 2.10 present the distance maps (left panel), the error maps (middle panel) and the histograms of the distance and error maps (right panel), as a function of $\mathscr{n}$ for both geometries. We found that:

- for higher $\mathscr{n}$, the morphological resolution of the spherical and bipolar objects is improved in the maps, and the error decreases;
- for $\mathscr{n} > 128$, one can see that a series of white stripes appear on the maps. This is due to the fact that the number of DMT map cells exceeds the number of SHAPE models cells;
- the D and its dispersion, in general, does not change.

For the spherical model, the variation of D and its error (error bars) as a function of $\mathscr{n}$ are plotted in Fig. 2.11. The blue dashed lines indicate the range of the reference distance. These variations show that:

- E decreases for higher values of $\mathscr{n}$, and remains at approximately 0.03% of the distance;
- D tends to the lower limit of the reference distance.

For the bipolar model, Fig. 2.12 shows a 4D plot in two perspectives, relating D and E as a function of $\mathscr{n}$ and $\mathscr{In}$. The volume delimited by the red dashed lines indicates the range of the reference distance. We highlight that:

- for small $\mathscr{n}$, the distance dispersion and E get higher and vice versa;
- due to the variation on $\mathscr{In}$, D and E do not show a tendency of having a specific value but a range of values, which are between 0.798 - 0.799 kpc and 2.0×10^{-4} - 4.0×10^{-4} kpc, respectively;

- D and E ranges overlap with the reference distance volume. The distances for the case $n > 30$ and $30 < In < 90$ appear to be systematically lower compared to the reference distance volume.

Similar to the previous analysis in Section 2.2.2, the relative distance error with respect to the reference value (δD) and the distance error fraction (E/D) for the spherical (upper panel) and bipolar (lower panel) models are plotted against n in Fig. 2.13. The average distance, over $\mathcal{J}n$ for each n ($D_{\mathcal{J}n}$), along with its propagated error (error bars of $D_{\mathcal{J}n}$ data points), the standard deviation ($\sigma_{D_{\mathcal{J}n}}$) and the standard deviation of the averaged relative distance error ($\sigma_{\delta D_{\mathcal{J}n}}$) of this averages distance, are calculated and plotted in

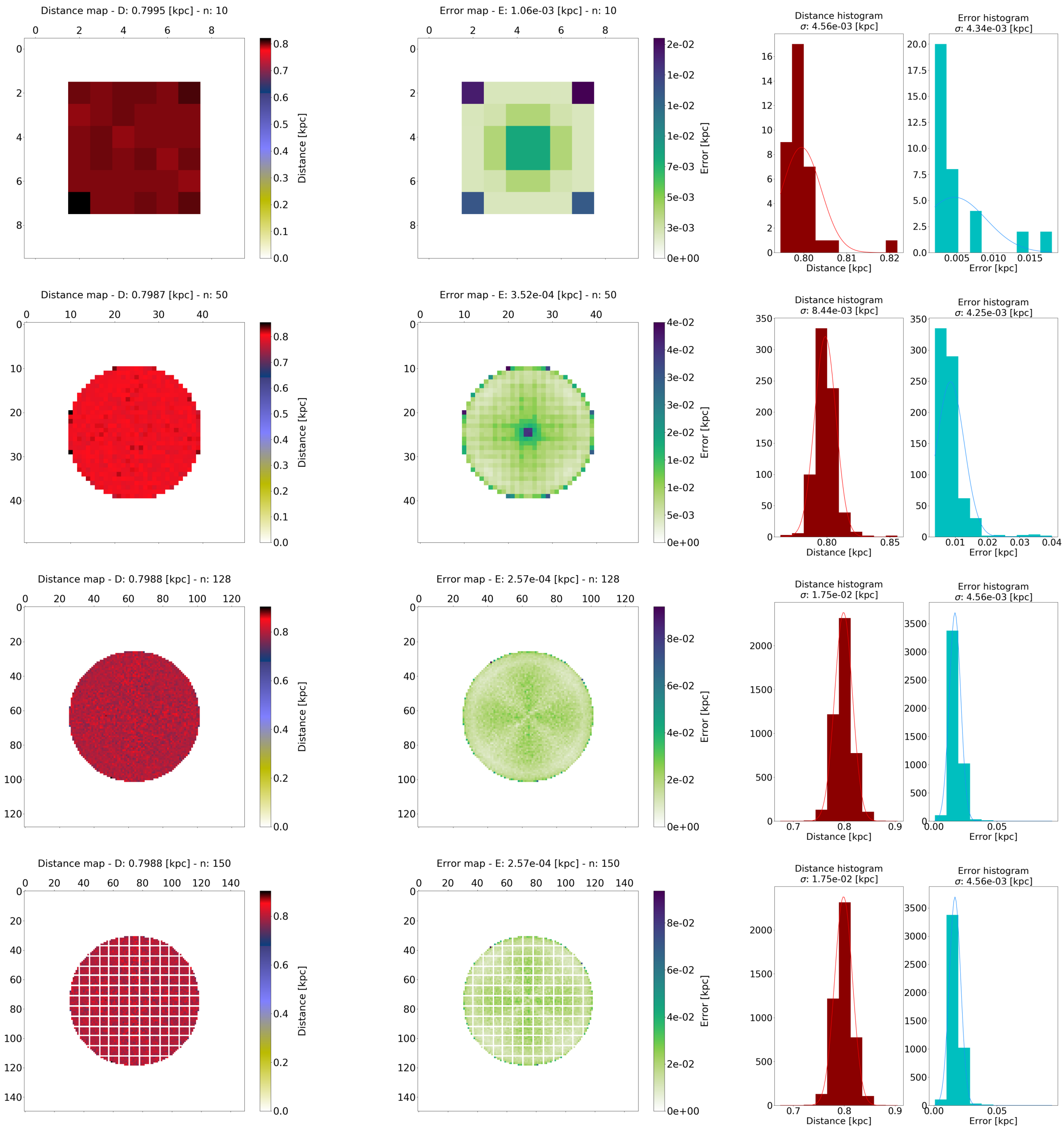

FIGURE 2.9: Distance maps (*left*), error maps (*middle*) and histograms of the distance and error maps (*right*), as a function of n, increasing from top to bottom, for the spherical case.

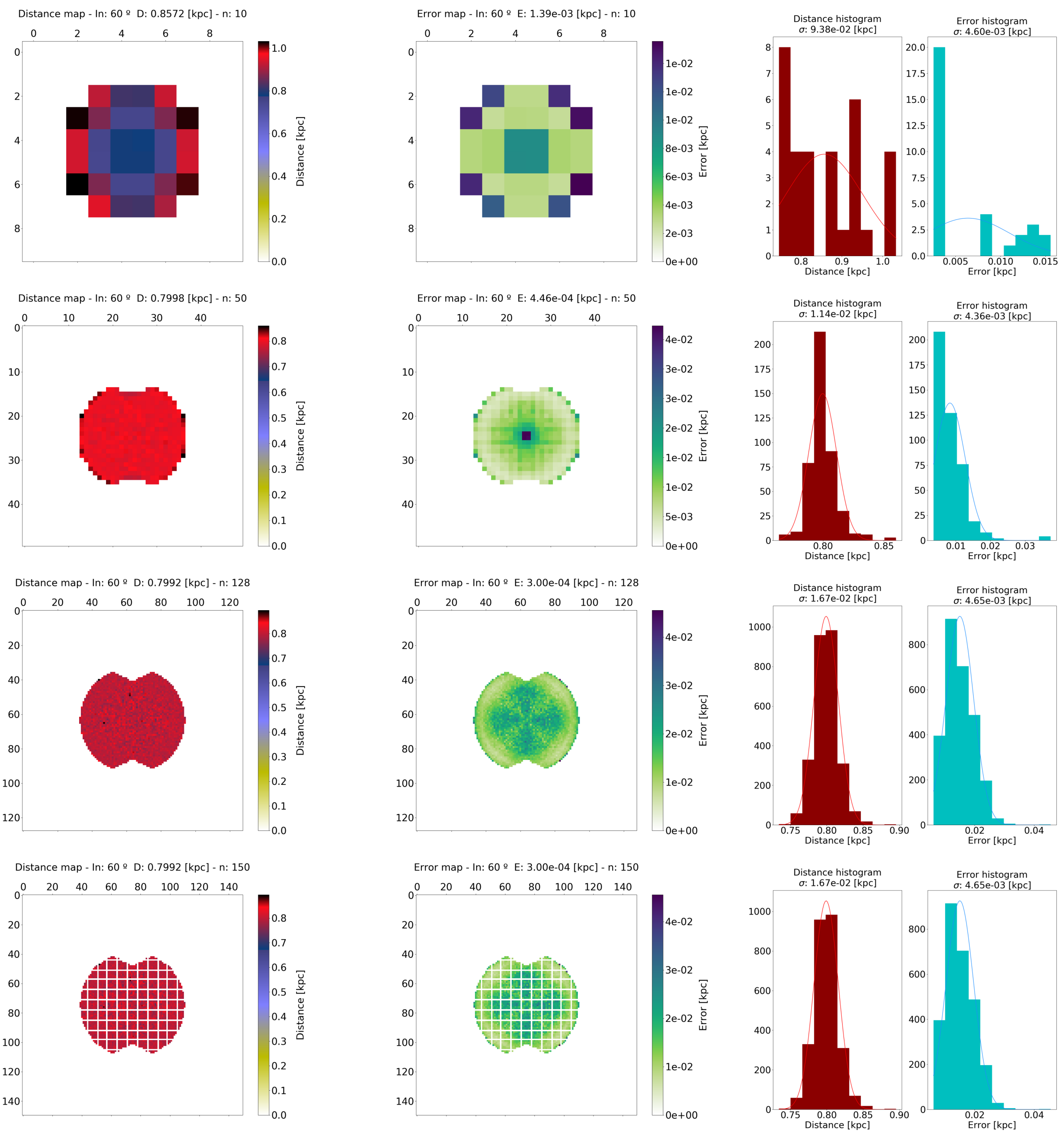

FIGURE 2.10: As in Fig. 2.9, but for the bipolar case, with $\mathcal{I}n = 60°$.

Fig. 2.14. After analyzing these plots, we deduce:

- for the spherical model, E/D decreases with n, and its value tends to be 0.04% as well as δD decreases with n;
- for the bipolar model,
  - both E/D and δD decrease with n;
  - the dispersion of the data points is due to the variation with $\mathcal{I}n$;
  - δD tends to be $\sim 0.05\%$ for $60 < n < 100$, whereas E/D gets values below 0.05% for $60 < n < 100$;

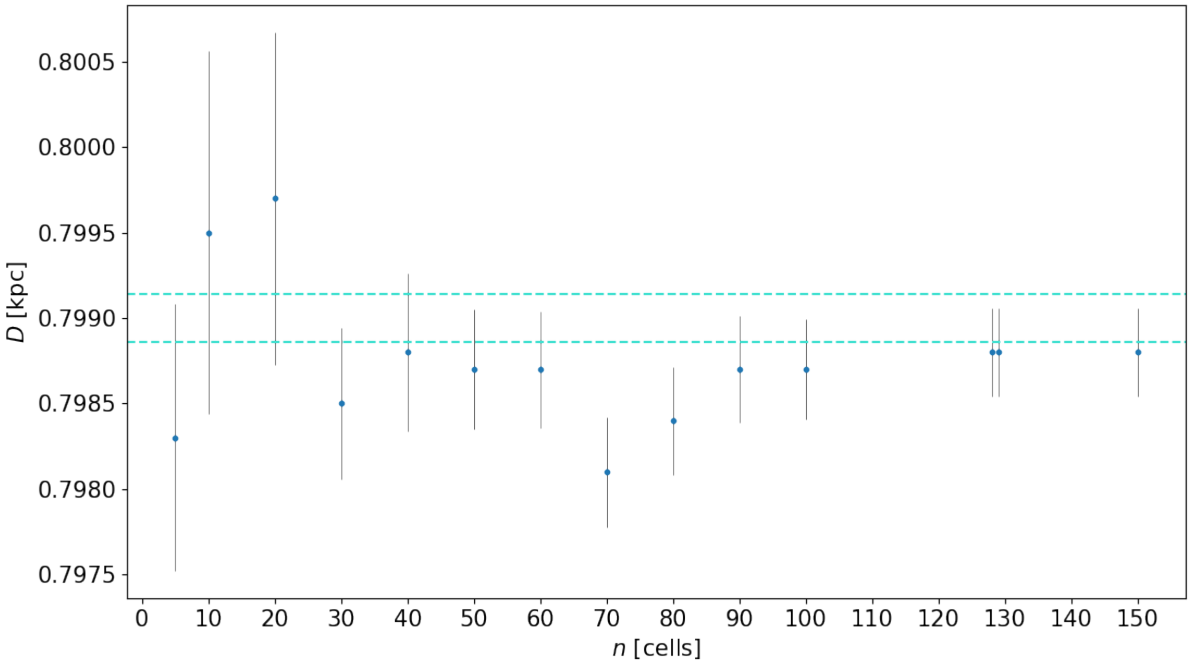

FIGURE 2.11: The distance D (blue points) and the error (error bars) as a function of the number of cells, $\mathcal{n}$. The pair of blue dashed lines delimit the range of the reference distance.

- $D_{\mathcal{J}n}$ tends to be 0.8 kpc while the propagated error decreases with the increasing of $\mathcal{n}$, up to $n < 128$;
- for $\mathcal{n} \geq 128$, the $D_{\mathcal{J}n}$ reaches the highest values, and the propagated error keeps the same order of magnitude;
- $\sigma_{D_{\mathcal{J}n}}$ decreases with $\mathcal{n}$, and the $\sigma_{\delta D_{\mathcal{J}n}}$ decreases up to $\mathcal{n} < 128$;
- for $\mathcal{n} \geq 128$ it is found that the $\sigma_{\delta D_{\mathcal{J}n}}$, $D_{\mathcal{J}n}$ and E/D increase.

Our conclusions from the second part of the statistical study are outlined below:

- the resolution directly impacts the determination of D, since δD, the deviation from the reference distance value, is different from 0, as presented above;
- $\mathcal{n}$ should take values between $60 < \mathcal{n} < N$, where N in this case is the grid size of the SHAPE models ($N = 128$). for $\mathcal{n} \geq N$, the E/D, $D_{\mathcal{J}n}$ and $\sigma_{\delta D_{\mathcal{J}n}}$ of the bipolar model, increase as a function of $\mathcal{n}$, which indicate that the error of the distance and the dispersion of the distance map will be large for this range of resolution. Moreover, in this range of resolution, the morphology of the object in the DMT maps displays strips of white cells;
- from $60 < \mathcal{n} < N$, the propagated error and the $\sigma_{D_{\mathcal{J}n}}$ get the lowest values. Conversely, when $\mathcal{n} < 60$ the propagated error can be of the order of 20% with respect to $D_{\mathcal{J}n}$;
- for the recommended resolution ($60 < \mathcal{n} < N$), the distance dispersion due to the variation with $\mathcal{J}\mathcal{n}$ ($\sigma_{D_{\mathcal{J}n}}$) reaches its lowest value, around 4.0×10^{-4} kpc;
- qualitatively the results are the same for the spherical and the bipolar cases.

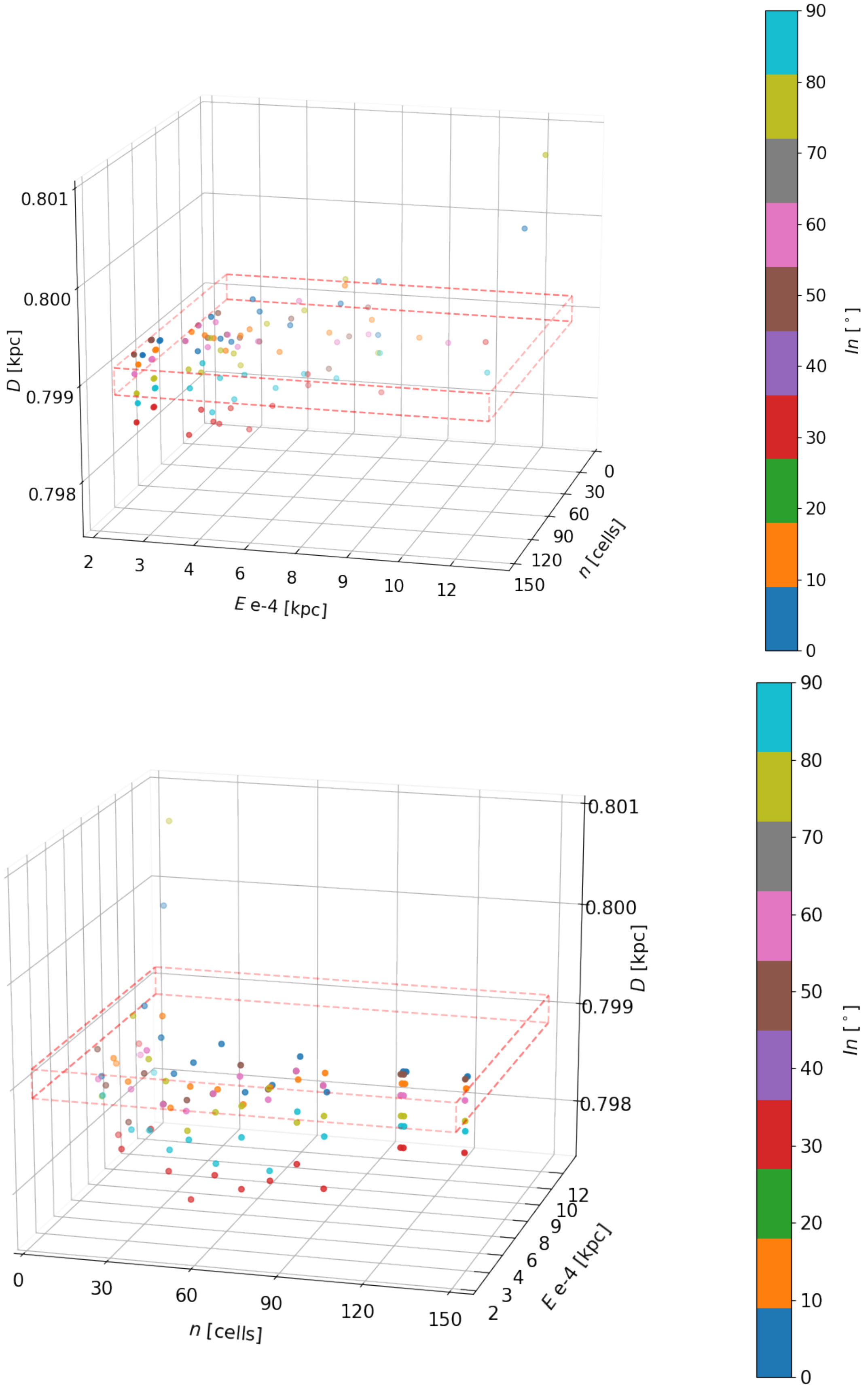

FIGURE 2.12: The distance D (z axis) as a function of the error, E (y axis) and the number of cells, n (x axis). The colors indicate the value of the inclination angle, $\mathcal{I}n$. The plot depth is represented by the fading of the color. The upper and lower panel present 2 different perspectives of the same plot **for the bipolar model**. The volume delimited by the red dashed lines is the range of the reference distance.

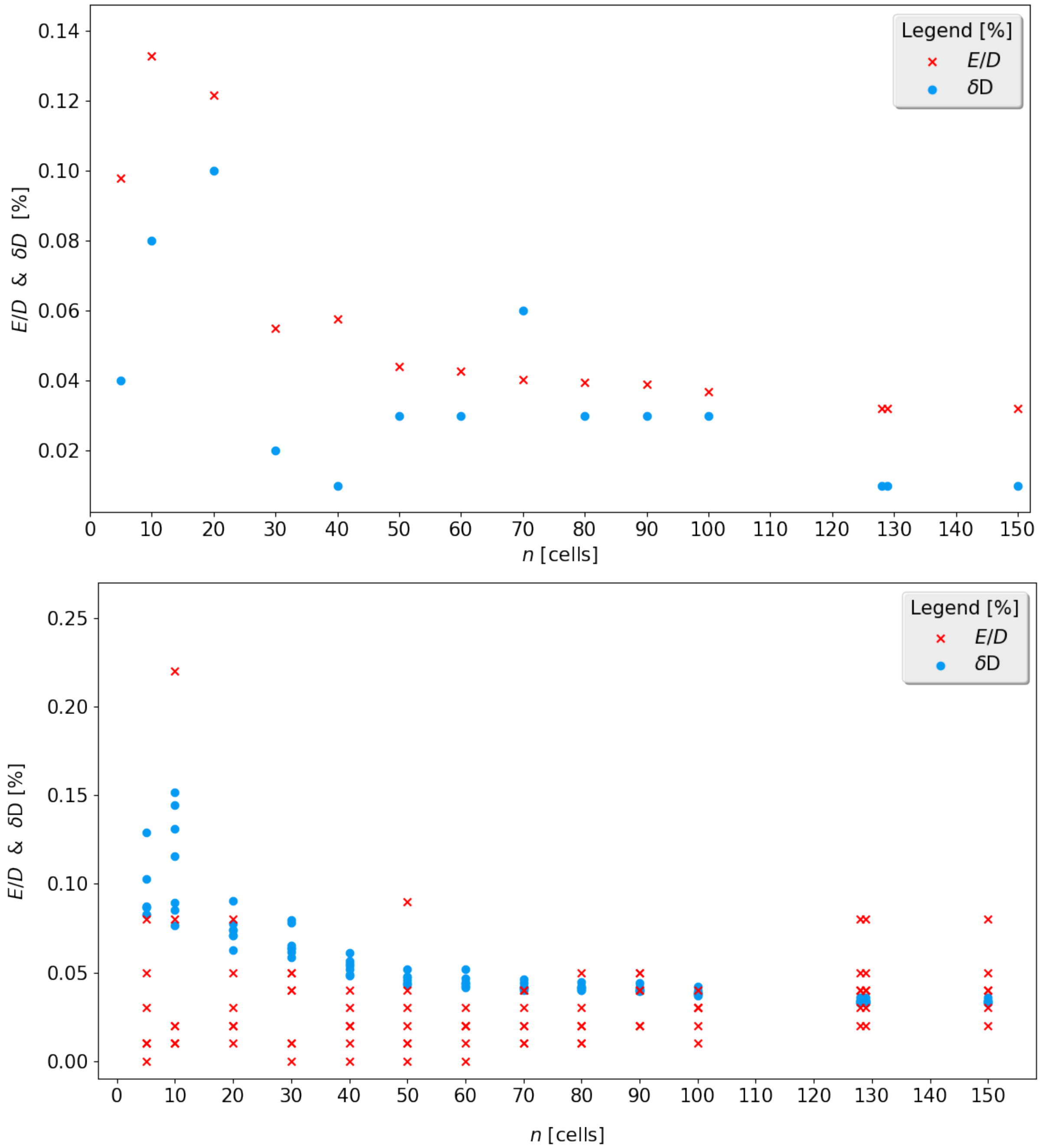

FIGURE 2.13: *Upper panel*: The relative distance error respect to the reference distance, δD (blue points) and the distance error fraction, E/D (red x) as a function of the number of cells, n in the spherical case. *Lower panel*: δD (blue points) and E/D (red x) as a function of n in the bipolar case.

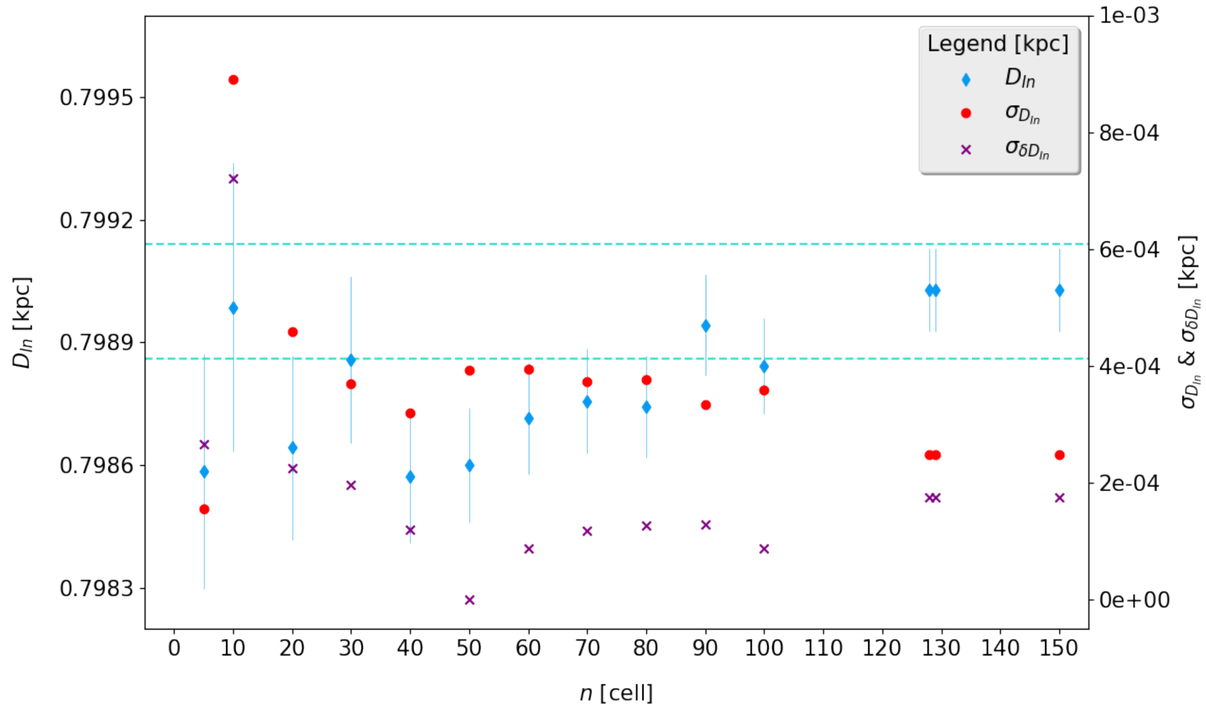

FIGURE 2.14: The averaged distance over $\mathcal{I}n$ $D_{\mathcal{I}n}$ (blue diamonds, left vertical axis) and its propagated error of the averaged distance (error bars), as a function of the number of cells n. On the right vertical axis are the standard deviation of this averaged distance $\sigma_{D_{\mathcal{I}n}}$ (red points) and its averaged relative distance error $\sigma_{\delta D_{\mathcal{I}n}}$ (purple x), as a function of n. The blue dashed lines delimit the range of the reference distance.

2.2.4 Constraining the number of velocity vectors, q

This third part of the statistical study is focused on obtaining the impact of the number of velocity vectors (q) (proper motion) on the DMT distance calculation. At this point, we analyze the deviations from the reference distance ($0.8 \pm 1.4 \times 10^{-4}$ kpc) by varying the geometry, $\mathcal{I}n$, n and q, considering $r = 0.5$. Since instead of found a n, we found a range for n, where the distance deviation is minimum. We also decided to use values for n outside and inside of the previously recommended range, for further testing. The third part of the statistical study, follows the steps below:

- the same sets of tangential velocity vectors generated in the Section 2.2.2, were used for both models (spherical and bipolar);
- sets of synthetic proper motion vectors are generated using a random number upper limit value, $r = 0.5$, for both geometries, and for these selected values of q: 5, 10, 15, 20, 30, 40, 50, 60, 70, 80, 100, 150, 200, 300, 400, 500 vectors;
- n:e: 10, 20, 50, 80, 100 numbers of cells are tested;
- the DMT was executed for each n and q (spherical case) and for every n and q plus $\mathcal{I}n$ (bipolar case).

Figs. 2.15 and 2.16 illustrate the distance maps (left panel), the error maps (middle panel) and histograms of the distance and error maps (right panel) as a function of q for $n = 80$,

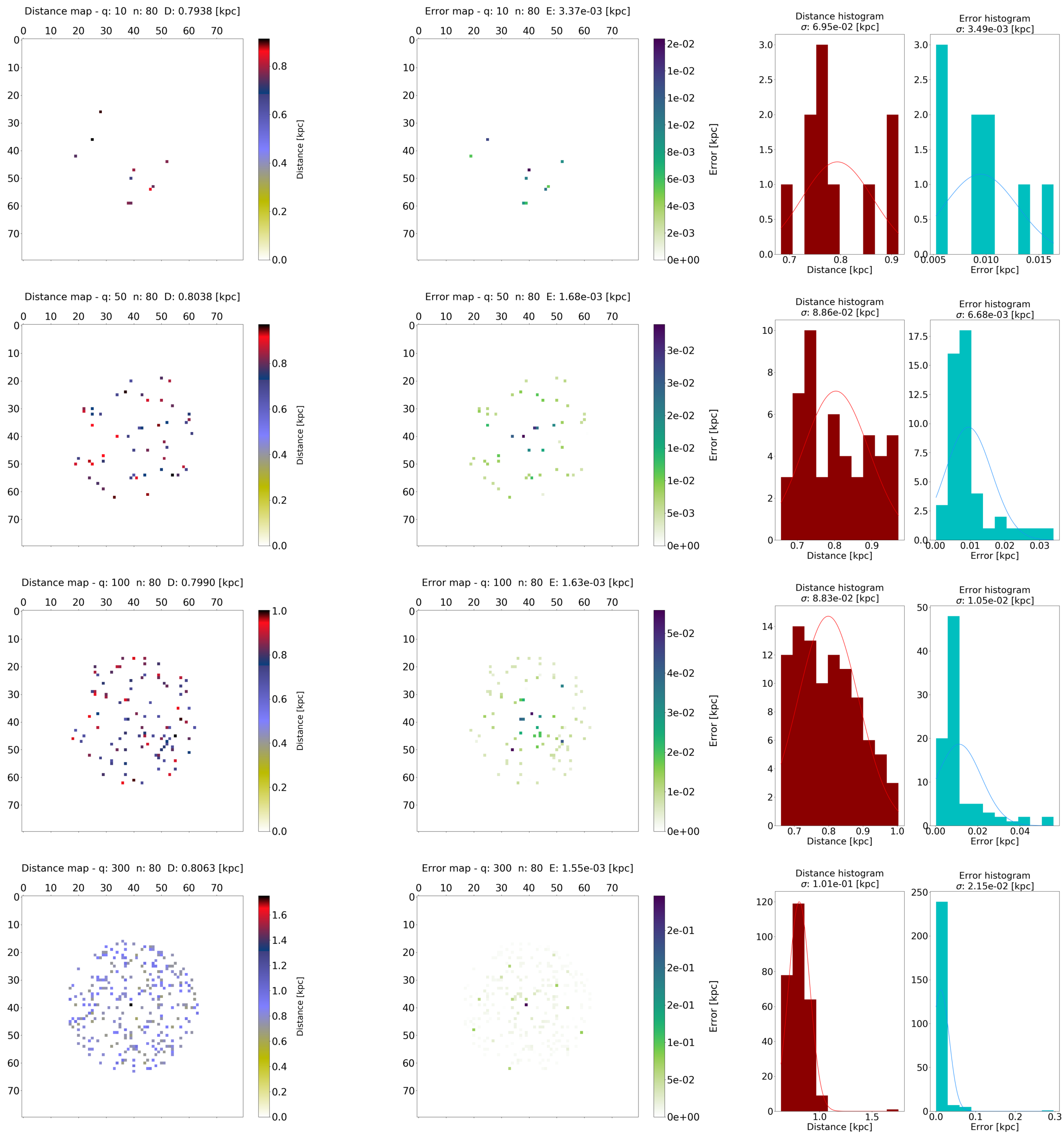

FIGURE 2.15: Distance maps (*left*), error maps (*middle*) and histograms of the distance and error maps (*right*), as a function of q, increasing from top to bottom, for the spherical case($n = 80$ cells).

for the spherical and bipolar ($\mathscr{I}n = 75°$) models. For higher q values the maps become more morphologically accurate (resemble better their respective geometric models), while the resultant distance increases and the error decreases.

In Fig. 2.17 we present the 4D plot for D and E, as a function of n and q parameters, for the spherical model. For the bipolar model, Fig. 2.18, displays the 5D plot for the D and E, as a function of n, q and $\mathscr{I}n$. Both plots show more significant distance deviations from the reference distance at $q \leq 100$ and $n \leq 50$. For $n \geq 50$ and $q \geq 100$ the error is found to be lower than 0.006 kpc, while the distance is approximately 0.8 kpc.

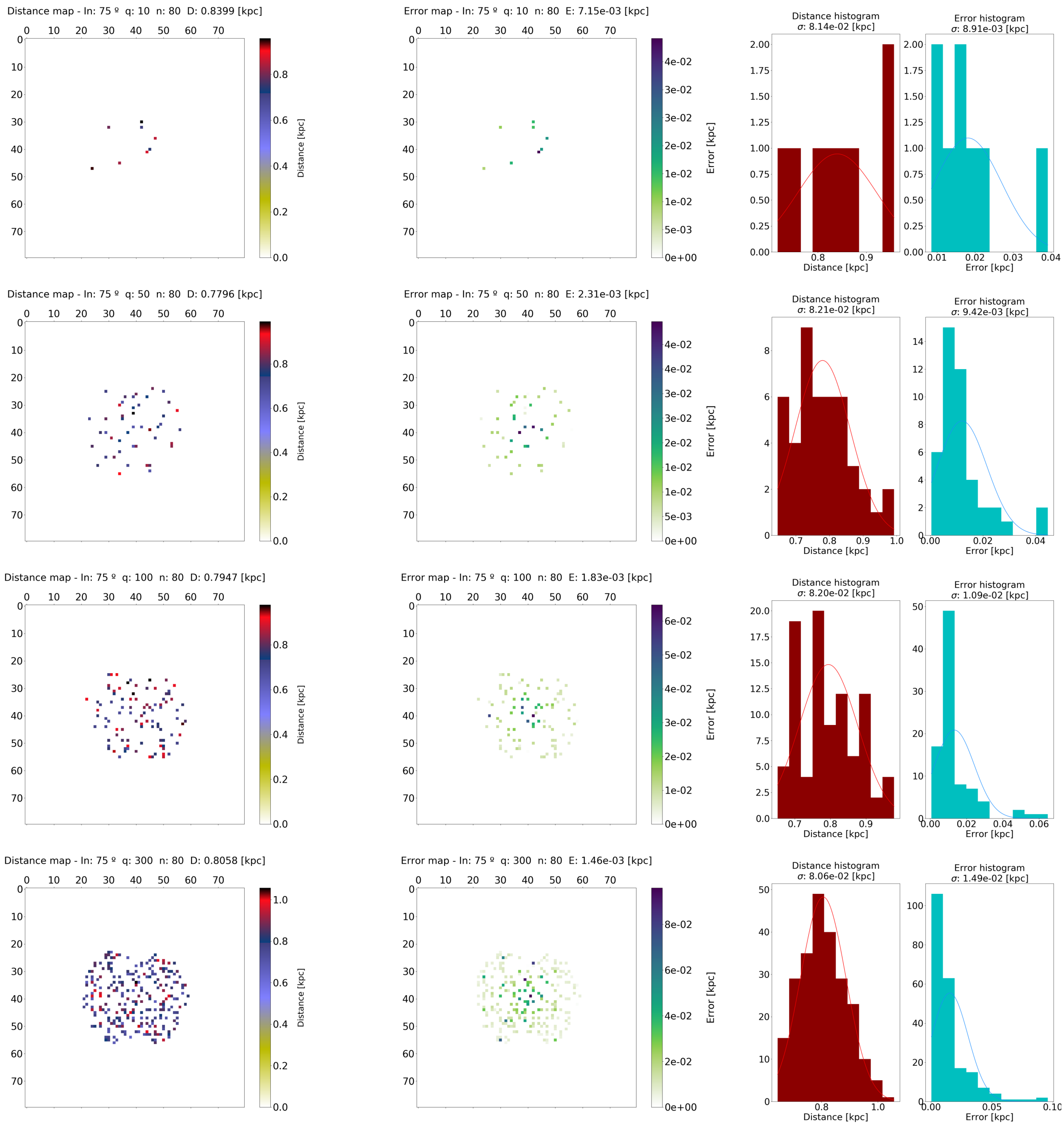

FIGURE 2.16: As in Fig. 2.15, but for the bipolar case, with $n = 80$ cells and $\mathcal{I}n = 75°$.

The relative distance error respect to the reference distance (δD) and the distance error fraction (E/D) are plotted as a function of n and q in the 4D plots of Figs. 2.19 and 2.20, for the spherical and bipolar models, respectively. The general trend of δD and E/D is the decrease with n and q. Both variables are found to be equal or below 1% for $n \geq 50$ and $n \geq 100$, in the two geometries.

The average distance, over $\mathcal{I}n$ for each n and q ($D_{\mathcal{I}n}$), are calculated for the bipolar model. Its propagated error ($E_{D_{\mathcal{I}n}}$) and the standard deviation of this average distance ($\sigma_{D_{\mathcal{I}n}}$) are also estimated. $D_{\mathcal{I}n}$, $E_{D_{\mathcal{I}n}}$ and $\sigma_{D_{\mathcal{I}n}}$, as function of n and q are presented on the 5D plot in Fig. 2.21. We find that both $\sigma_{D_{\mathcal{I}n}}$ and $E_{D_{\mathcal{I}n}}$ decrease with n and q while $D_{\mathcal{I}n}$ tends to be equal to 0.8 kpc.

The main conclusions from these analysis are:

- $\mathscr{q}$ has an additional deviation component in the derived DMT distance, since δD is always different from 0;
- for low $\mathscr{q}$ and low resolution ($\mathscr{q} \leq 100$ and $\mathscr{n} \leq 50$) E/D and δD could be up to 11%;
- we show that from 50 cells, the behavior of the data points is similar to that of the higher values of $\mathscr{n}$. Therefore, the previous recommended lower limit of Section 2.2.3 for $\mathscr{n}$ is shifted from 60 to 50. Therefore, the final recommended range for the resolution is $50 \leq \mathscr{n} \leq 100$ cells;
- all the variables analyzed in this part of the work have a more stepper decrement with $\mathscr{q}$ than with $\mathscr{n}$, showing that the DMT is more sensitive to the number of vectors of the synthetic proper motion sets than to the resolution;
- the distance dispersion due to the variation with $\mathscr{In}$ goes from 20 to 2% with the increase of $\mathscr{q}$ and $\mathscr{n}$;
- qualitatively the results for the bipolar and spherical models are the same;
- since E/D and δD for $\mathscr{q} \geq 100$ have low values, and keep declining in magnitude, the recommended number of proper motions vector is found to be $\mathscr{q} \geq 100$.

2.2.5 Constraining the variation of the position angle, $\mathscr{d}PA$

With the aim of studying the influence of the PA variations ($\mathscr{d}PA$) on the DMT and in the morpho-kinematic models, small offsets from the original PA (PA=0) of the bipolar model, were applied in order to test this parameter. The following offsets were applied: 0, ±5, ±10, ±15 °. For the rest of the parameters is consider the following values, $\mathscr{n}$ = 60 cells, $\mathscr{q}$ = 100 vectors and $\mathscr{In}$ = 30, 60 and 90 °. The steps of the analysis followed:

- the same sets of tangential velocity vectors generated in Section 2.2.2 are used for both models (spherical and bipolar);
- a synthetic proper motion data set with 100 vectors, and for $\mathscr{r} = 0.5$ is considered;
- the DMT was executed for the three values of $\mathscr{In}$ and varying with dPA.

Fig. 2.22 shows the distance (left panel), the error maps (middle panel) and the histograms of the distance and error maps (right panel) as functions of $\mathscr{d}PA$, which increases from top to bottom. Bipolar case, with $\mathscr{In} = 60$. We observe that the higher the PA offset, the worse the recovering of the bipolar shape. The distance deviations from the reference value reach higher values for higher $\mathscr{d}PA$. The error does not present a identifiable trend.

The relative distance error with respect to the reference distance (δD) varying with $\mathscr{d}PA$ and $\mathscr{In}$, is presented in the top panel of Fig. 2.23. There is no clear trend either in the data points, or in the variation with $\mathscr{In}$ or $\mathscr{d}PA$. The range of variation of δD remains between 0 and 3%. The distance error fraction (E/D), as a function of $\mathscr{d}PA$ and $\mathscr{In}$, is presented in the bottom panel of Fig. 2.23. Again, there is no clear trend with any of

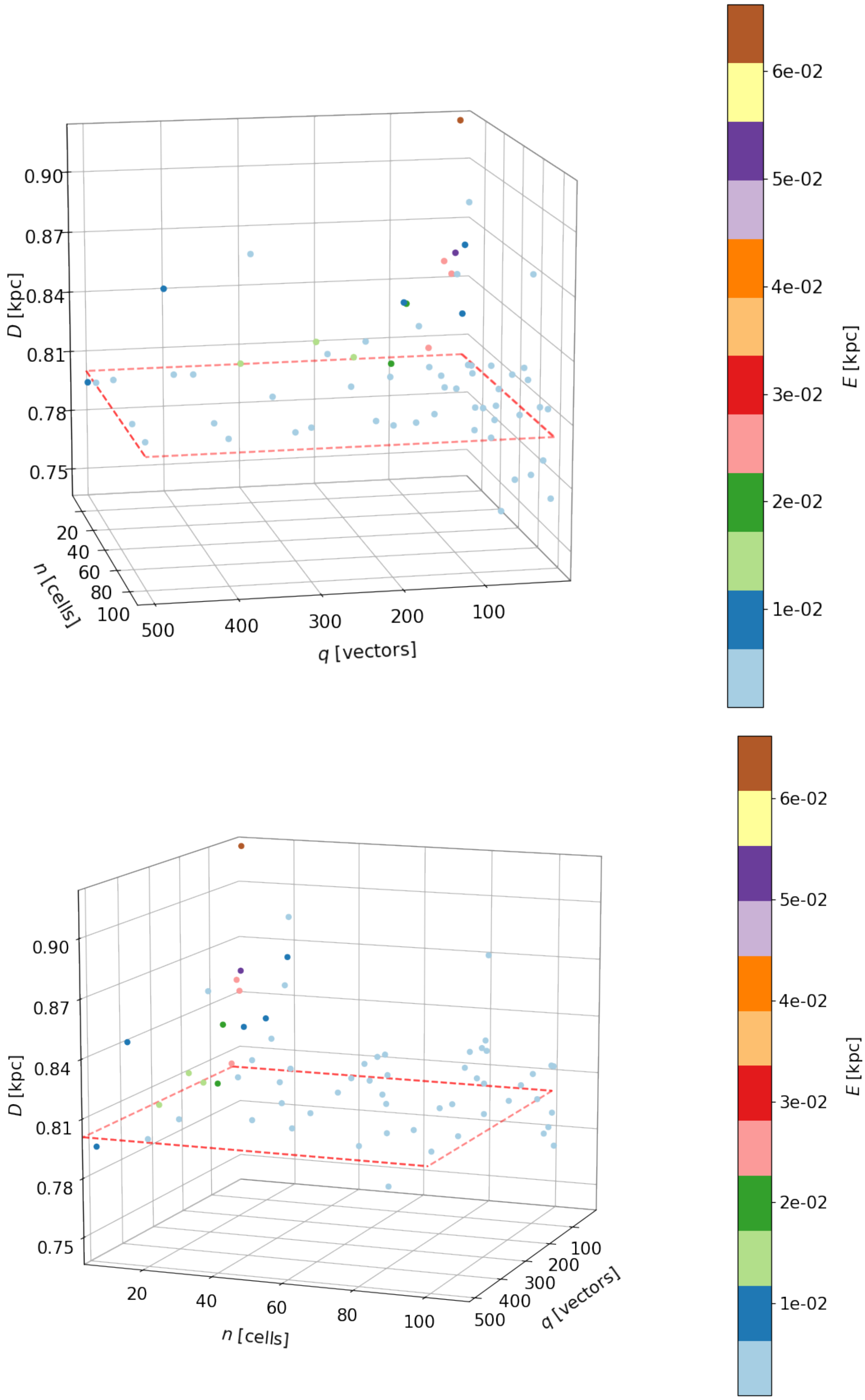

FIGURE 2.17: The distance D (z axis) as a function of the number of cells n (y axis) and the number of vectors q (x axis). The color indicates the error. E. The upper and lower panel present 2 different perspectives of the same plot **for the spherical model**. The volume delimited by the red dashed lines is the range of the reference distance.

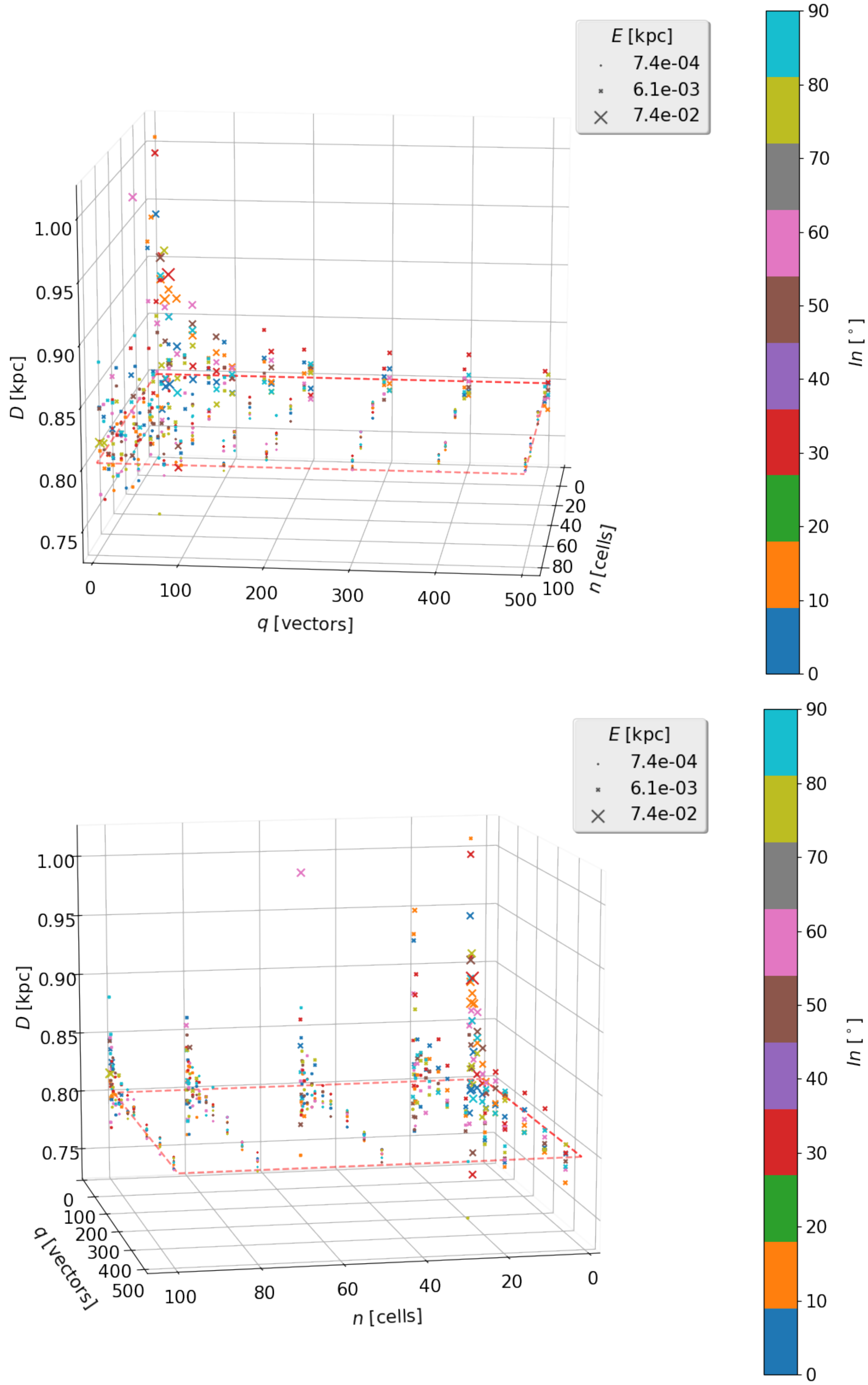

FIGURE 2.18: The distance D (z axis) as a function of the number of cells n (x axis) and the number of vectors q (y axis). The color indicates the error E. The upper and lower panel presents 2 different perspectives of the same plot **for the bipolar model**. The volume delimited by the red dashed lines is the range of the reference distance.

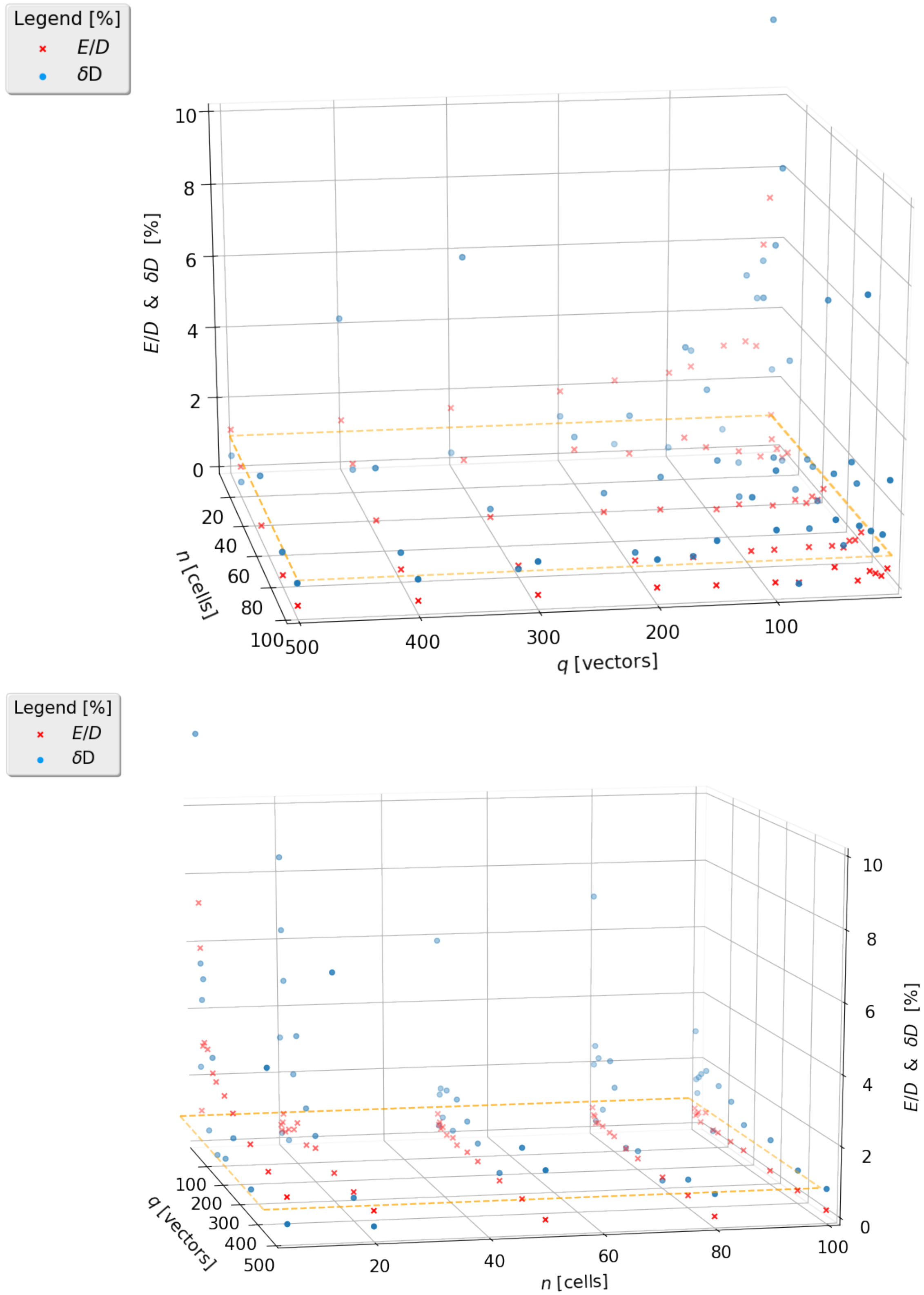

FIGURE 2.19: The distance error fraction E/D (red x, z axis) and the relative distance error respect to the reference distance δD (blue points, z axis) as a function of the the number of cells n (y axis) and the number of vectors q (x axis) **for the spherical model**. The plot depth is represented by the fading of the color. The volume enclosed by the orange dashed lines gives the range of the reference distance.

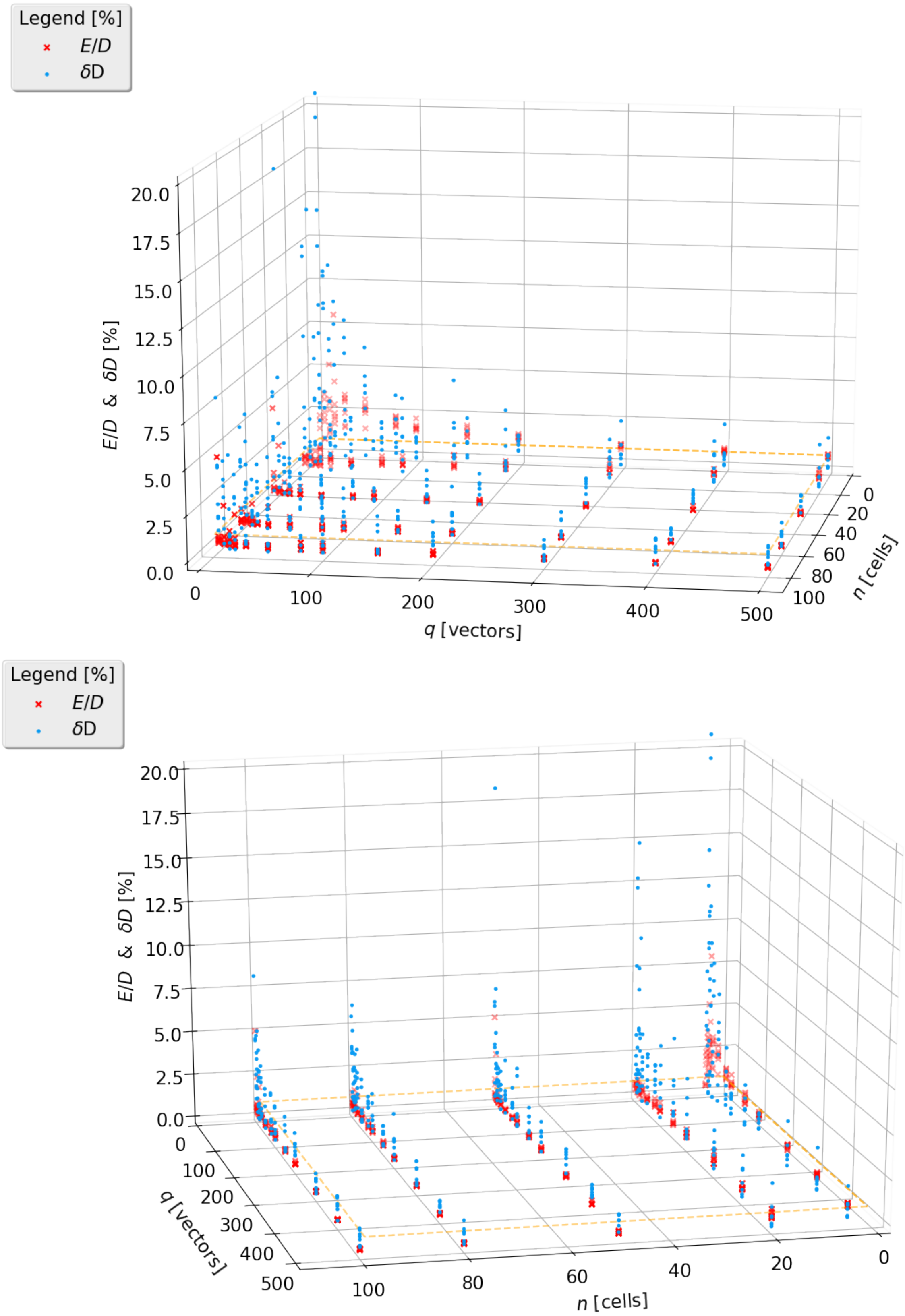

FIGURE 2.20: As Fig. 2.19, but **for the bipolar model**.

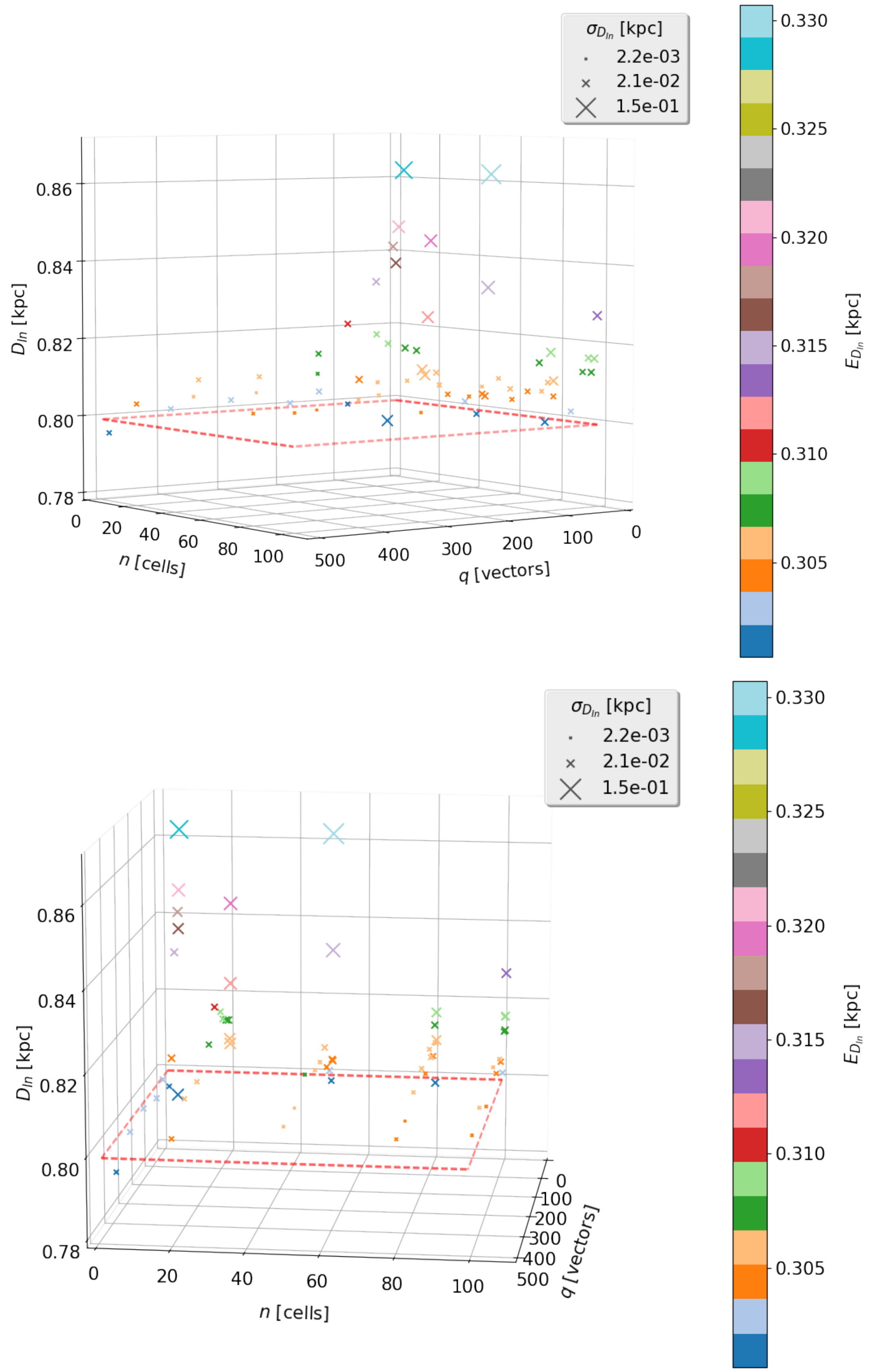

FIGURE 2.21: The averaged distance over $\mathcal{I}n$ $D_{\mathcal{I}n}$ (z axis) as a function of the number of cells n (y axis) and the number of vectors q (x axis). The color indicates the standard deviation of this averaged distance $\sigma_{D_{\mathcal{I}n}}$. The size of the markers represents the averaged relative distance error $\sigma_{\delta D_{\mathcal{I}n}}$. The volume delimited by the orange dashed lines correspond to the range of the reference distance.

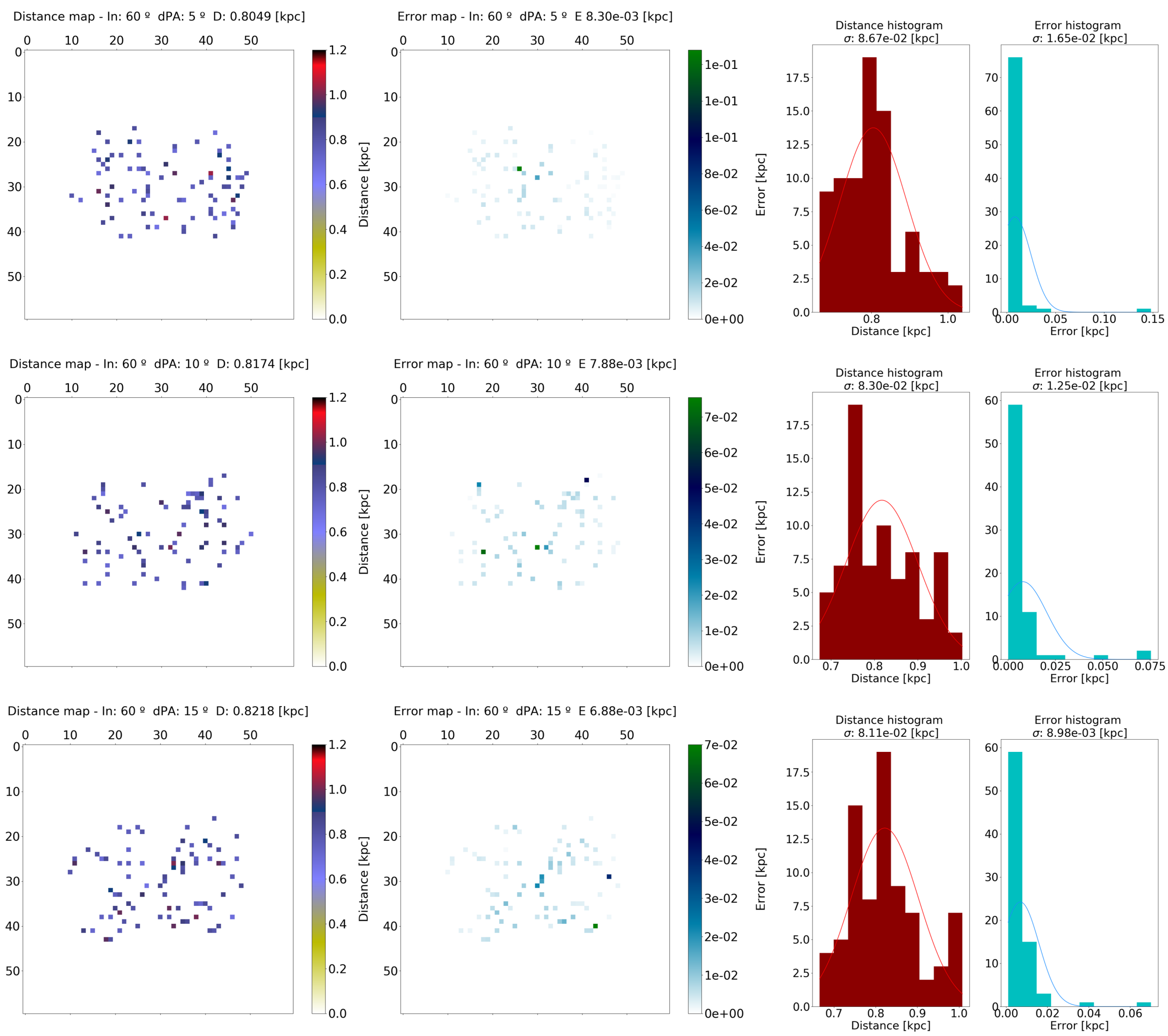

FIGURE 2.22: Distance maps (*left*), error maps (*middle*) and histograms of the distance and error maps (*right*), as a function of dPA increasing from top to bottom, for the bipolar case with $\mathcal{J}n = 60°$.

the two variables, dPA and $\mathcal{J}n$. The range of variation of E/D remains between 0.1 and 0.55%.

The average distance, over $\mathcal{J}n$ for every value of dPA ($D_{\mathcal{J}n}$), together with its propagated error ($E_{D_{\mathcal{J}n}}$) and the standard deviation of this averaged distance ($\sigma_{D_{\mathcal{J}n}}$) are calculated and plotted. $D_{\mathcal{J}n}$, $E_{D_{\mathcal{J}n}}$ and $\sigma_{D_{\mathcal{J}n}}$ as a function of dPA, are presented in Fig. 2.24. We note that $D_{\mathcal{J}n}$ covers a range from 0.8 to 0.82 kpc, or a variation of 2% with respect to the reference distance (blue dashed lines), but does not follow any clear trend with dPA. The E/D remains below 2.0×10^{-3} kpc and presents almost no variation with dPA. The $\sigma_{\delta D_{\mathcal{J}n}}$ varies with dPA in one order of magnitude, but does not present a clear pattern.

From the above analysis, we conclude that offsets of the PA have a minimum effect on the DMT distance calculation, reaching a maximum deviation of 2% if $dPA \neq 0$.

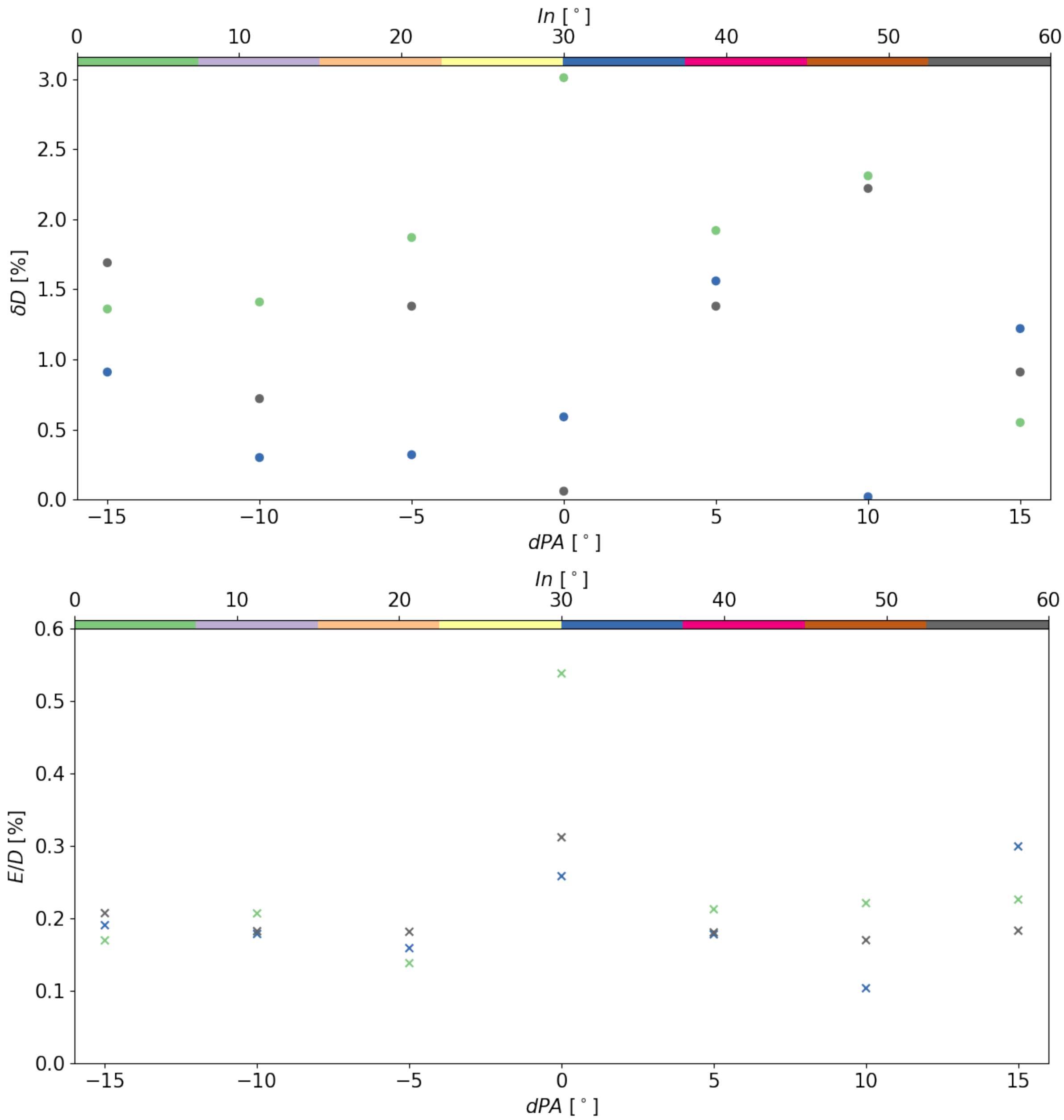

FIGURE 2.23: *Upper panel*: the relative distance error respect to the reference value δD, as a function of $\mathscr{dPA}$. *Lower panel*: the distance error fraction E/D, as a function of $\mathscr{dPA}$. The colors denote the values of the inclination angle $\mathscr{In}$.

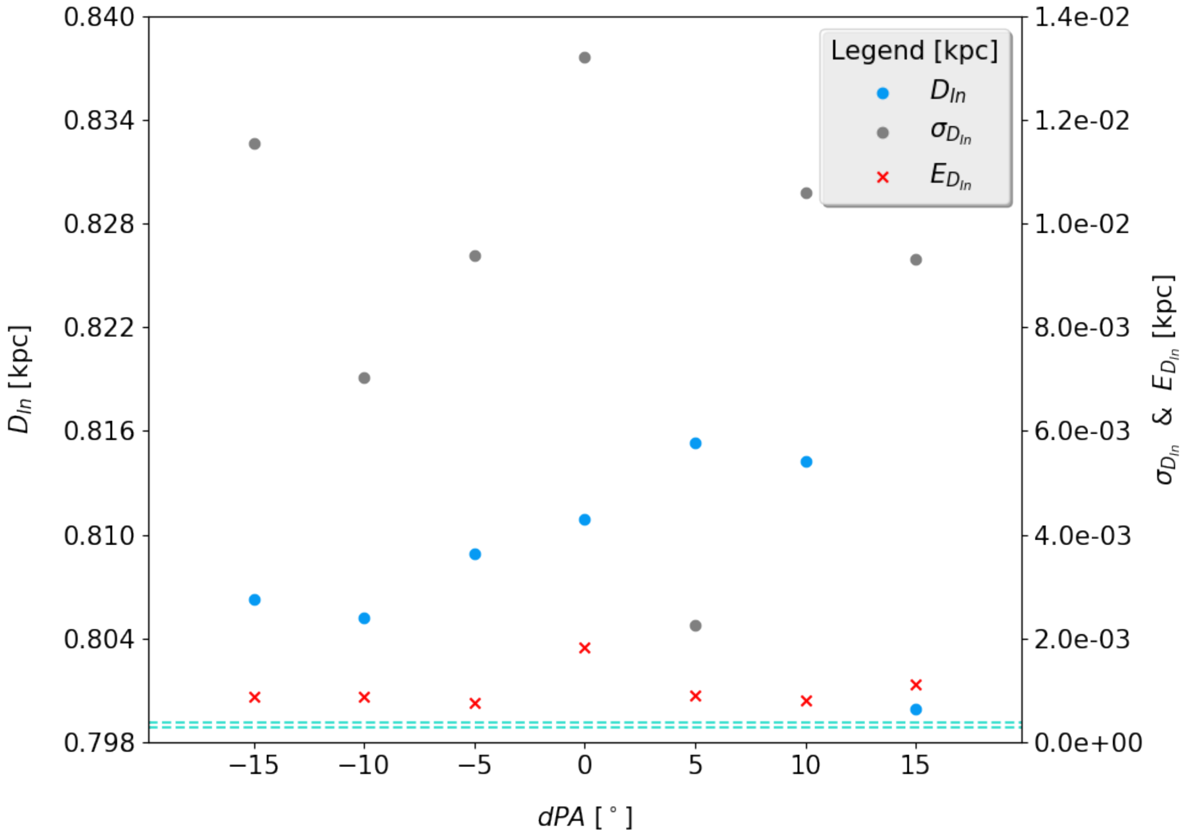

FIGURE 2.24: The averaged distance over $\mathcal{I}n$ $D_{\mathcal{I}n}$ (blue points, left axis) as a function of dPA. The averaged relative distance error $\sigma_{\delta D_{\mathcal{I}n}}$ (grey points, right vertical axis) and the propagated error of this averaged distance $E_{D_{\mathcal{I}n}}$ (red x, right vertical axis) as a function of dPA. The blue dashed lines denoted the range of the reference distance.

2.2.6 Overall results from the statistical study

The statistical study of the DMT was performed to establish the relationships between the parameters: upper limit of the random number (r), resolution (re) in terms of the number of cells (n), number of vectors (q), inclination angle ($\mathcal{I}n$), the deviation from the position angle (dPA) and the variation in the geometry of the model (spherical, bipolar) with the DMT distance calculation. The statistical study was carried out by using synthetic nebulae and their velocity fields as inputs of the DMT. Our general conclusions are the following:

- we found that the 1 kpc reference distance is systematically reduced to 39% of the r value. The error is increased systematically per 0.05% of r value. For the rest of statistical study r was fixed at 0.5, establishing a new distance of reference equal to 0.8 $\pm 1.4 \times 10^{-4}$ kpc, different from the initial one of 1 kpc;
- the resolution of the maps was defined in terms of the number of cells, n. The lowest distance deviations from the reference distance with the smallest errors, are found for $50 \leq n \leq N$ cells, where N is the grid size of the 3D models. For small values of n, the distance deviations and the error get the lower magnitudes. For $n > N$, the distance and its error are not significantly improved and the DMT maps

displays white strips. For SHAPE morpho-kinematic models it is recommended to use a resolution for which $50 \leq n \leq 100$;

- the DMT is more sensitive to the number of vectors (q) than to any other quantity, because it is directly associated with main inputs of the DMT. For $q \geq 100$ vectors, the δD and E/D are below 5% and 2%, for the bipolar and spherical models, respectively, and decrease for higher q. For $q < 100$ vectors, δD and E/D can be as high as 11% and 20%, for both geometric cases;
- according to the dPA analysis, we conclude that poor 3D SHAPE models, in therms of orientation, results in less accurate distance estimations and a poor morphological distance and error maps;
- the distance deviation due to the variation of $\mathscr{I}n$ is smaller for higher n and q, and it can be up to 2%, for the recommended resolution and the number of proper motion vectors.;
- the results of the DMT are not affected by the geometry of the nebular model.

3

DMT Application to Nebulae

3.1 NGC 6543

NGC 6543 is a planetary nebula in the constellation of Draco (RA: $17^h58^m33.43^s$; DEC: $+66°37'59.5''$), at the northern hemisphere, also called the Cat's Eye nebula. Its CS parameters as the surface temperature, radius, luminosity and stellar wind mass-loss rate have been derived, and are between 36,200 K (Natta et al., 1980) and 80,000 K (Bianchi et al., 1986); 0.64 and 0.8 $R_\odot$ (Castor et al., 1981; Bianchi et al., 1986; Perinotto et al., 1989); 3.75 and 4.18, in units of $\log(L/L_\odot)$ (Zhekov & Perinotto, 1998; Bianchi et al., 1986); and 1.7×10^{-6} and 2.8×10^{-9} $M_\odot$/yr (Zweigle et al., 1997; Hutsemekers & Surdej, 1987). The mass of the CS is estimated to be 0.61 $M_\odot$ (Zhekov & Perinotto, 1998), with a stellar velocity wind of 1,900 km/s (Perinotto et al., 1989). It is likely that a binary system with a spectral type of O7 + WR (Aller, 1976) lies in the nucleus of this PN. However this is still controversial. The electron temperature varies from 7 to 10,000 K from the center to the outer regions of the nebula (Wesson & Liu, 2004), whereas the average electron density in the nebula is around 4,500 cm^{-3} (Wesson & Liu, 2004).

3.1.1 Kinematics and morphological description

A morphological description of NGC 6543 was provided by Reed et al. (1999) with a detailed description of the inner and outer features. A inner elongated bubble (a prolate ellipsoid), called the inner ellipse, is identified at the center of the nebula and it is filled up with hot gas, which temperature, derived from X-ray spectral fits, is $\sim 1,700,000\ K$ (Chu et al., 2001). It displays a non-uniform expanding behavior, with the outermost tips having the lowest velocities. This inner ellipse turns out to be nested in a bipolar structure, a pair of large spherical bubbles that are conjoined, forming the waist of the nebula. The waist is observed as a second larger ellipse lying perpendicular to the inner ellipse. The conjoined bubbles are older and expand with a lower velocity compared to the inner ellipse. A pair of polar caps and polar condensations are also present at the tips of the bubbles, being very bright in low-ionization lines (Gonçalves et al., 2001; Akras et al., 2016).

The inner ellipse as well as the whole bipolar structure are surrounded by a number of concentric rings, which are probably the projection of spherical bubbles of apparently constant mass and thickness (Balick et al., 2001). The concentric rings are likely associated with periodic mass-loss events, probably due to the pulsations of stellar winds during the AGB phase (Balick et al., 2001) (see also Section 1.1.3 for more details). At even higher distance from the CS, there is a large, patchy and filamentary halo, almost kinematically inert in contrast with its explosive "appearance" (upper panel, Fig. 3.1), with a maximum expansion velocity of 4.5 km/s (Bryce et al., 1992). The lower part of Fig. 3.1 points out all the aforementioned structures.

3.1.2 Previous distance determinations

NGC 6543 is a widely studied object and various distance determinations are provided by several authors using different techinques. O'Dell (1962) used the flux density in the Hβ emission line to derive D = 0.996 kpc. Also using the Hβ flux, Cahn & Kaler (1971) derived D = 1 kpc. Castor et al. (1981) found D = 1.17 kpc, by assuming that the CS is on the post-AGB evolutionary tracks calculated by Renzini (1979). Later on, Phillips & Pottasch (1984); Maciel (1984) and Cahn & Kaler (1971) used the radio flux of the nebula to calculate its distance equal 4.14 kpc, 0.7 kpc and 0.64 kpc, respectively. A kinematic distance obtained of 0.89 kpc was calculated by Kaler et al. (1985). In order to derive the CS photosperic parameters of NGC 6543, the absolute calibrated spectrum was compared with the theoretical energy distribution, and a distance of 1.39 kpc was derived by Bianchi et al. (1986). Perinotto et al. (1989) derived D = 1.44 kpc using atmospheric models of the CS and the observed stellar flux at 1300Å. By selecting the distance that matches the evolutionary age of the CS to the dynamical age of the envelope, Mal'Kov (1997) found D = 1.8 kpc. Reed et al. (1999) derived D = 1.001 $\pm$ 0.269 kpc by applying the expansion parallax method to proper motion measurements and spectroscopically obtained radial expansion velocities. Cazetta & Maciel (2001) provided a range of distance for NGC 6543, between 0.9 and 1.3 kpc, by using the surface gravity distance method. Mellema (2004) presented a new distance to NGC 6543, 1.55 $\pm$ 0.44 kpc by applying a correction factor to the previous distance of Reed et al. (1999), to account for the fact that the pattern velocity (shocks/ionization fronts) is always larger than the matter (gas) velocity. More recently, by determining the mean value of the bolometric magnitude, Phillips (2005) found D = 1.14 kpc.

3.1.3 Morpho-kinematic model and DMT application

The morpho-kinematic code SHAPE was used to reconstruct the 3D structure of NGC 6543 (Steffen & López, 2006; Steffen et al., 2011) based on the structure's description of Reed et al. (1999), and the PV diagrams obtained from the San Pedro Martir catalog of Galactic PNe (López et al., 2012) using the slits 'a' and 'b' (Fig. 3.1). The position of these two slits is shown overlaid on the [N II] and [O III] HST images of NGC 6543 (panel (a) and (b), Fig. 3.2). A simple geometrical approach was assumed to model the 3D structure of the nebula. The two conjoined bubbles were modeled assuming a bipolar structure, whose lobes are simulated as spherical shells with a constant density (panel (c), Fig. 3.2).

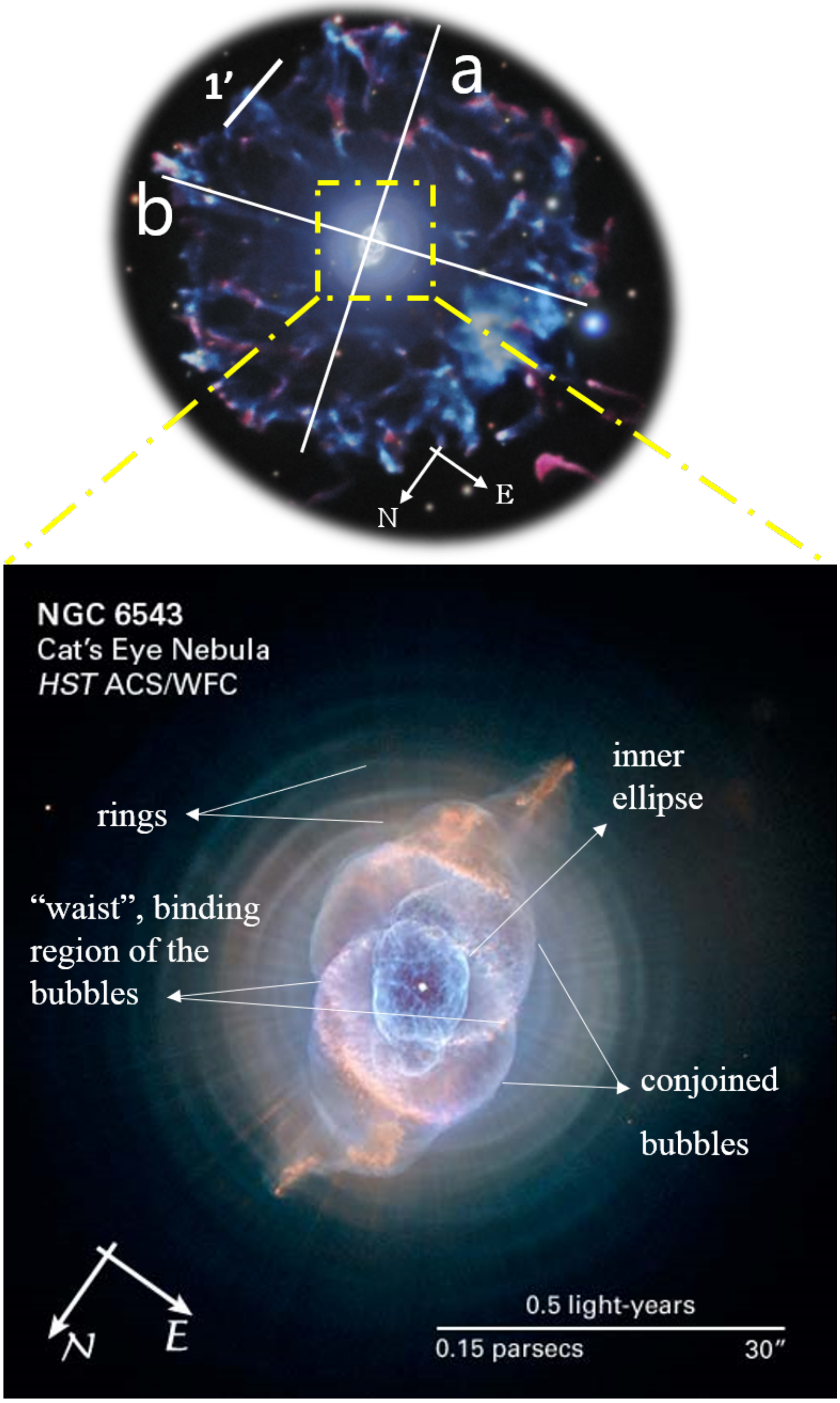

FIGURE 3.1: *Upper panel*: composite image of long and short exposures of the halo of NGC 6543 displaying the slits 'a' and 'b'. Adapted from JDS Astrophotograpghy 2016. *Lower panel:* image of NGC 6543 in [O III] and Hα+[N II] showing the rings, the inner ellipse and the conjoined bubbles. Adapted from ESA, NASA, HEIC and The Hubble Heritage Team (STScI/AURA).

The [N II] image and the PV diagrams were used to reproduce the 3D morpho-kinematic model in despite the fact that the proper motions were measured in the [O III] image. It was necessary to construct a 3D model using the [N II] PV diagrams since they provide a more detailed illustration of the nebular components of NGC 6543 than the [O III] PV diagrams. To create the final [O III] model, the [N II] model was scaled to match the [O III] PV diagrams.

For the expansion velocity field we considered a single homologous velocity law, with V = 22*(r/r_o) km/s, where r is the distance from the CS and r_o is the reference radius of the shell. The synthetic PV diagrams of our model are overlaid on the observed ones (panel (d) and (e), Fig. 3.2) and they are in good agreement with the observed ones using a simple bipolar structure.

For NGC 6543 as well as for the rest of PNe studied in this work, all the vectors of the tangential velocity field were obtained from the respective SHAPE. It is important to mention that the distance errors presented in this work do not include the observational error of the proper motions (except for GK Persei, Section 3.5). Moreover, the outliers of the distance and the errors were found and excluded from the final estimation of the average values, as it is described in Section 2.1.1.

The specific entries for the DMT to determine the distance to NGC 6543 are:

- 107 proper motion measurements from the [O III] HST image, by Reed et al. (1999);
- a map size of 60 × 30 arcsec^2;
- the following maps resolutions (re)[1]: 6, 3, 2, 1.5, 1.2, 1, 0.857, 0.75 and 0.6 arcsec.

Distance and error maps for different values of resolution (re) are presented in Fig. 3.3 and Fig. 3.4, where the re increases from left to right (Recall that lower resolutions mean higher values of re, because lower is the number of cells (n) in the maps, Eq. (2.1)). The increase of the resolution results in (i) slightly different values for the distance and the error and (ii) the improvement of the morphological detail of the maps. Differential resolution for the x and y sides of the map were used to present a morphologically accurate map (less flattened).

In order to choose the best distance estimation using the DMT, when it is applied to any extended nebula, such as NGC 6543, we developed a coefficient of variation analysis. Generally, the coefficient of variation follows the equation $Cv_x = \sigma_x/\bar{x}$ and it was applied to the distance and error maps. The distance coefficient of variation (Cv_D) and the error coefficient of variation (Cv_E) are calculated and analyzed as functions of the resolution (re or n). These coefficients reflect on the extent of the distance/error variability of the maps, in terms of their mean values. Despite the fact that the minimum variability for both parameters is expected to be the best choice, we also used the following criteria. They are: (i) the weighted average value of the two coefficient of variance ($\overline{Cv}$); and (ii) the quality of the morphological features of the distance map.

The best distance and error maps will be selected by the minimum value of $\overline{Cv}$ as long as the criteria (ii) is not relevant, which is the case of a low number of measured proper motion vectors available. The criterion (ii) is relevant when the proper motions are enough to discern the morphological features of the nebula in the distance map. In that case, the resolution plays a fundamental role in the visualization of these features. Therefore, if the minimum $\overline{Cv}$ corresponds to a distance map that clearly displays the

[1] These are the values of the resolution in the x direction. The re in the y direction are the half of the re_x

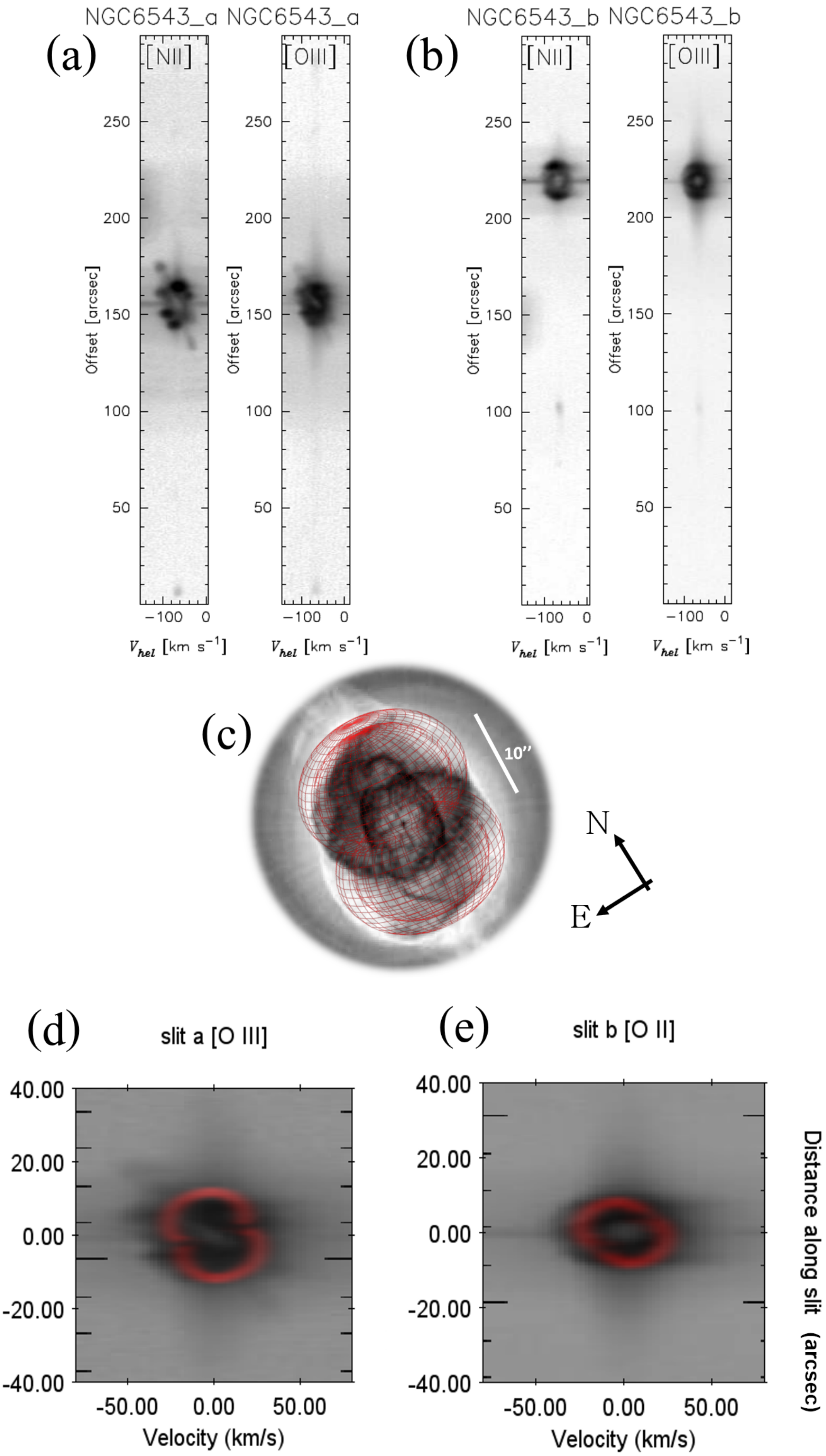

FIGURE 3.2: *Upper panel:* Comparison of the slit 'a' (a) and slit 'b' (b) in emission lines of [N II] and [O III]. *Medium panel:* 3D bipolar model superimposed on the [O III] image (c). *Lower pannel:* synthetic [O III] PV diagrams overlaid on the observed ones for slit 'a' (d) and 'b' (e).

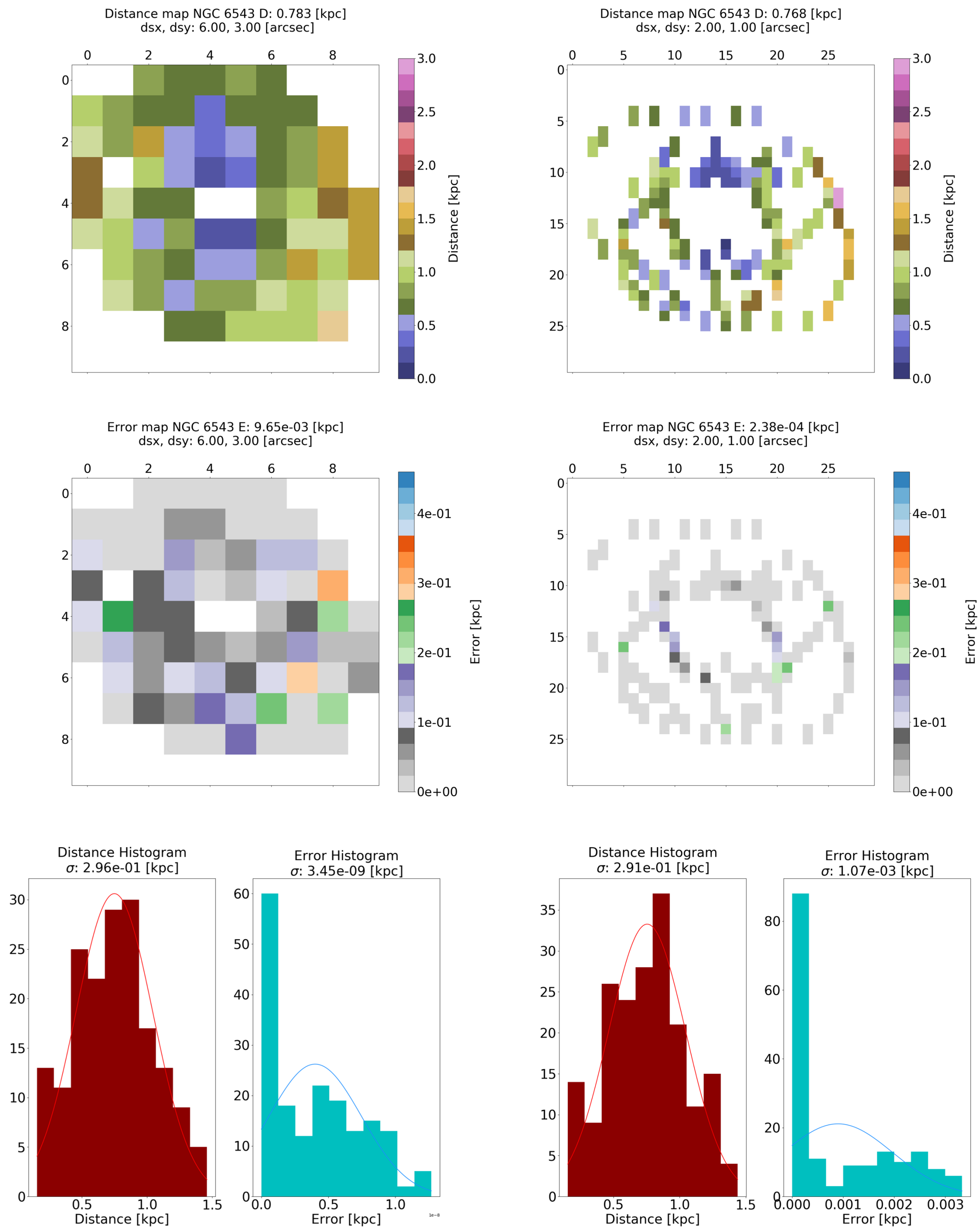

FIGURE 3.3: Distance maps (*upper panels*), error maps (*middle panels*) and histograms of the distance and error maps (*lower panels*), as a function of re (from left to right).

morphological features of the nebula, this will be the best distance estimation. Otherwise, the best distance estimation will be the next minimum $\overline{Cv}$ that matches a distance map with discernible features. It is important to distinguish the morphological features on the distance map to link them with the real images of the nebula, in order to develop

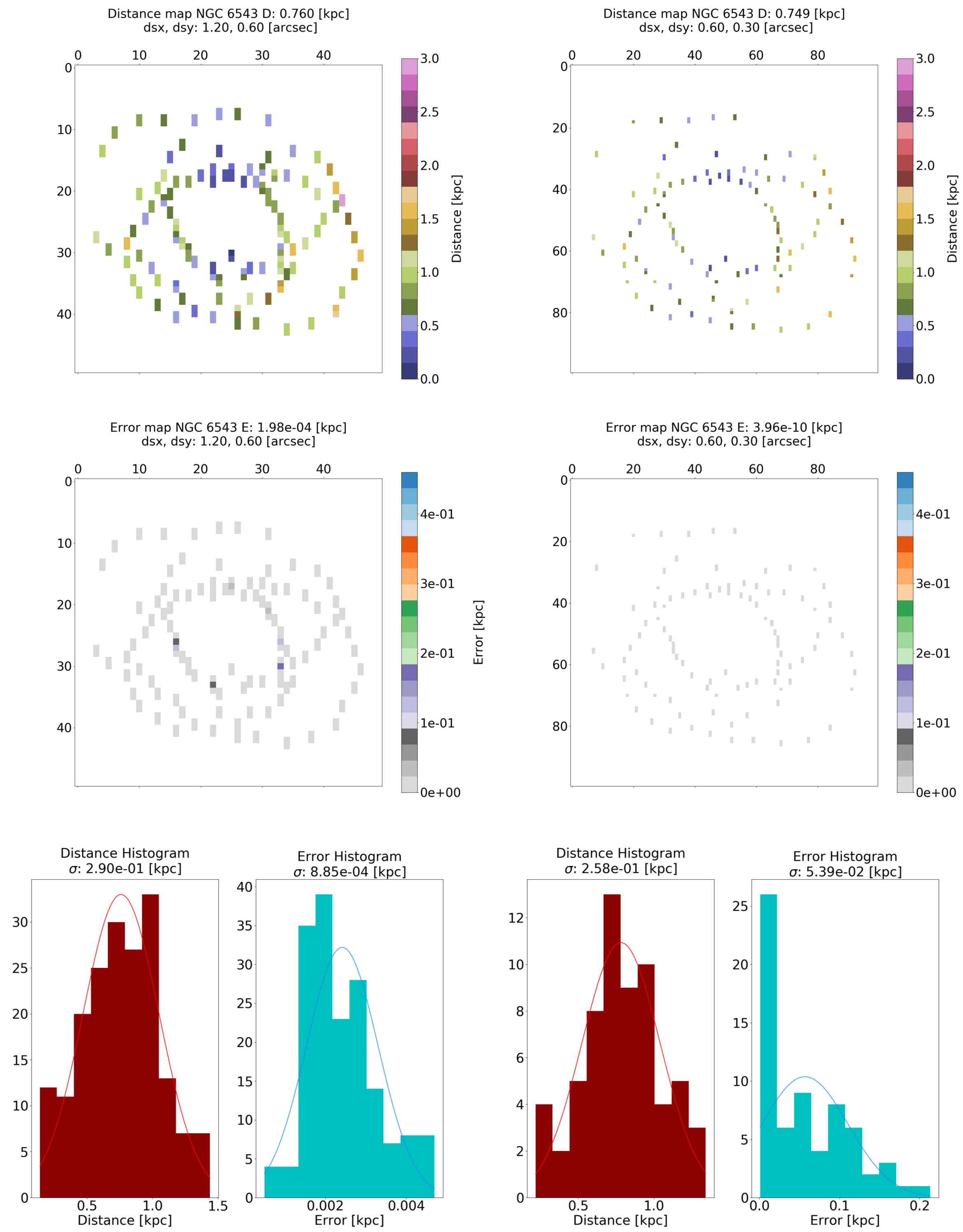

FIGURE 3.4: Continuation of Fig. 3.3.

a kinematic analysis of them based on distance deviations from the mean value. The weight to calculate $(\overline{Cv})$ is 50% for Cv_E, because the error calculated by the DMT only corresponds to the implicit uncertainty of the technique (which is really low), and 100% for Cv_D, because the distance is the principal result of the DMT.

After applying the coefficient of variation analysis to the present nebula, we found the that the most appropriate distance estimation for NGC 6543 occurs for $re = 1.2$ arcsec. The correspondent distance map (Fig. 3.5) presents dispersed and aggregated inhomogeneities with significant distance deviations from the mean distance. The agglomerated inhomogeneities with similar distance deviation values, that appear as regions of similar color in the distance map, are designated as systematic deviation regions (SDRs), and they have an particular kinematic interest.

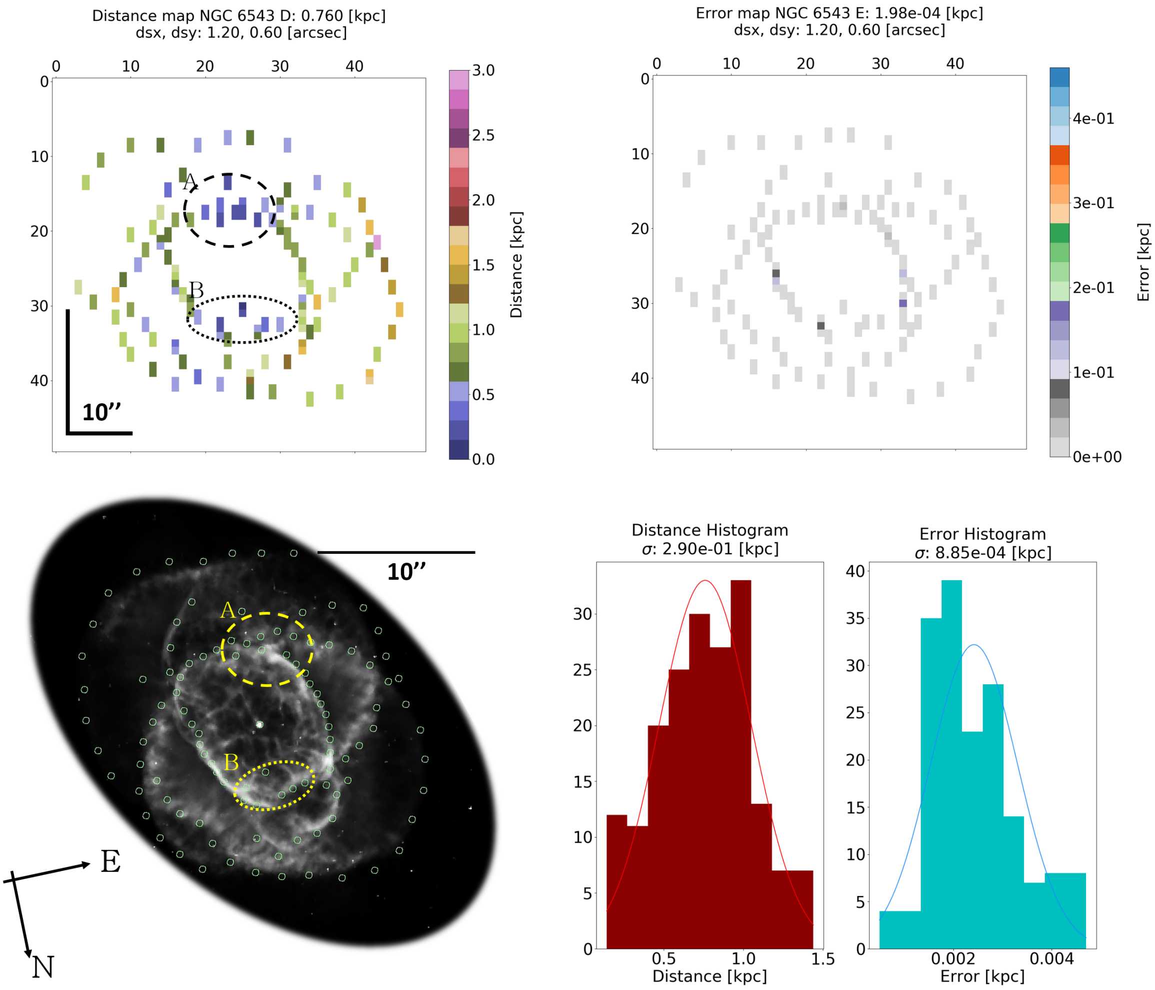

FIGURE 3.5: *Upper panel:* NGC 6543 distance and error maps, for $re = 1.2$ arcsec. The SDRs are marked in black over the distance map. *Lower panel:* The [O III] HST image with the location of the 107 measured proper motions (green circles), with the SDRs in yellow and the histograms of the maps.

A physical interpretation for the SDR is possible, since the distance deviations can be understood in terms of kinematic phenomena as follows. A given homogeneous velocity field, as was assumed to derive the tangential velocity vectors ($V_\perp$) is expected to match the observed angular expansion velocity field ($\dot{\theta}$), measured as proper motions. Therefore, any distance deviations from the mean value indicates a difference between $V_\perp$ (the modeled velocity field) and $\dot{\theta}$ (the observed velocity field) components as expressed by Eq. (1.3). This means that in a SDR with distance estimated above the mean, the observed proper motions have lower values than the modeled velocity vectors. On the contrary, in SDRs below the mean, the proper motions are higher than the modeled velocity vectors. To provide an explanation of this localized discrepancy between the modeled and observed velocity field, presented as SDRs in the distance map, a deeper analysis on the SDR is required, in contrast to the morphological features of the nebula.

Two SDRs are identified and highlighted in Fig. 3.5 resulting from the comparison of the distance map with the [O III] image of NGC 6543. We note that these SDRs do not correspond to any particular peculiarity in the error map, which is highly homogeneous. Thus, we can discard the possibility that the SDRs are due to problems in the proper motions measurements and/or the modeled velocity field. This fact hints for a kinematic explanation of the SDRs presence on the distance map of NGC 6543.

The SDRs A and B (see, Fig. 3.5) correspond to the bright borders between the inner ellipse and the bipolar waist. Due to the location of the proper motions of the SDRs A and B, it is likely that they are associated with the bipolar structure and the inner ellipse. Hence, the modeled velocity field diverges from the associated proper motions in these regions. Therefore, given the lower distance values for SDRs A and B, the observed angular expansion in these regions is higher than expected, which can be explained if the observed proper motions are a mixture of the angular expansion of both structures (inner ellipse and bipolar lobes) due to a projection effect.

Distance [kpc]	Reference
1	Cahn & Kaler (1971)
1.17	Castor et al. (1981)
4.14	Phillips & Pottasch (1984)
0.7	Maciel (1984)
0.64	Cahn (1984)
0.89	Kaler et al. (1985)
1.39	Bianchi et al. (1986)
1.44	Perinotto et al. (1989)
1.8	Mal'Kov (1997)
1.001 ± 0.269	Reed et al. (1999)
0.9 - 1.3	Cazetta & Maciel (2001)
1.55 ± 0.44	Mellema (2004)
1.14	Phillips (2005)
1.19 ± 0.11	Present work
0.9 - 1.48	Present work

TABLE 3.1: Cat's Eye distance determinations.

The resultant distance to NGC 6543 derived from the distance map with $re = 1.2\,\text{arcsec}$, is $0.76 \pm 2{\times}10^{-4}$ kpc. However, this value must be corrected because the systematic difference between the matter and the pattern velocities in PNe (Mellema, 2004) (Section 1.3.1). This correction factor (F) was estimated to be 1.56 ± 0.15 kpc (see, Fig. 1.7) (Mellema, 2004; Schönberner et al., 2005). Once F is applied to our DMT value, the final distance to NGC 6543 is 1.19 ± 0.11 kpc. Beware that the error of the distance only corresponds to the inherent uncertainty of the DMT, and the propagation of the error to F. Our result is highly consistent with the previous determined values (see, Table 3.1).

The distance and error values in the DMT maps present a Gaussian distribution clearly seen in the histograms (lower panel, Fig. 3.5). Interestingly, the standard deviation of the error maps shows a clear trend to decrease with the resolution (see Fig. 3.3). Besides the average distance of NGC 6543, we also yield the most probable 1σ distance range between 0.9 and 1.48 kpc. The latter is based on the dispersion value of the distance map ($\sigma_D = 0.29$). 7 out of 13 previous distances[2] estimations listed in Table 3.1 are in this range. This shows that our distance determination of NGC 6543 agrees not only with the previous values derived from the expansion parallax method but also with other methods.

3.2 NGC 6720

This is one of the most widely studied PN, with mora than 760 references so far. It is also known as the Ring Nebula or M57, and is located in the Lyra constellation (RA: $18^h53^m35.08^s$; DEC: $+33°01'45''$). The CS of NGC 6720 presents a surface temperature of 100,000 K (Ziegler et al., 2012), a luminosity of $\log(L/L\odot) \simeq 2.3$, which combined with a nebular age of 7,000 yr gives a stellar mass of 0.61 - 0.62 $M_\odot$ (O'Dell et al., 2007). This indicates that the CS is transitioning to the WD cooling track (O'Dell et al., 2007). By comparing the position of the star in the $\log(T_{eff})$-$\log(g)$ diagram with the evolutionary tracks, an additional value for the stellar mass of 0.53 $M_\odot$ was determined by Ziegler et al. (2012). The electron density of the ionized gas is 500 - 700 cm^{-3} (O'Dell et al., 2007), while the electron temperature varies from 12,000 K in the inner regions to 10,000 K in the outer regions (Garnett & Dinerstein, 2001).

3.2.1 Morphological and kinematic description

The Ring Nebula has a triaxial pole-on shape oriented toward us and it is compound of a thick elliptical equatorial ring (called the main ring), plus a thin and faint polar region (O'Dell et al., 2007) (Fig. 3.6). The main ring is an elliptical structure of ionization bounded gas with a great density concentration in its equatorial plane. In addition, it is surrounded by a glow of [O III] emission and a low-ionization halo. Opposite to the bright nebular emission, several dark knots are seen, pointing towards the CS (O'Dell et al., 2013). A large stratification of the ionization structure and radial velocity is present, being the brightest emissions close to the plane of the sky and the spatial velocity law from the CS scaled with the spatial distance (O'Dell et al., 2007).

A homologous expansion law has shown an excellent agreement with the measure of individual [N II] emission-line features, dark knots, ionized gas and from radial and tangential velocity measurements (O'Dell et al., 2007, 2009, 2013). In such scenario, the ions of higher ionization expand more slowly, such type of motion is commonly found in PNe O'Dell et al. (2007).

[2] Excluding our estimation and range

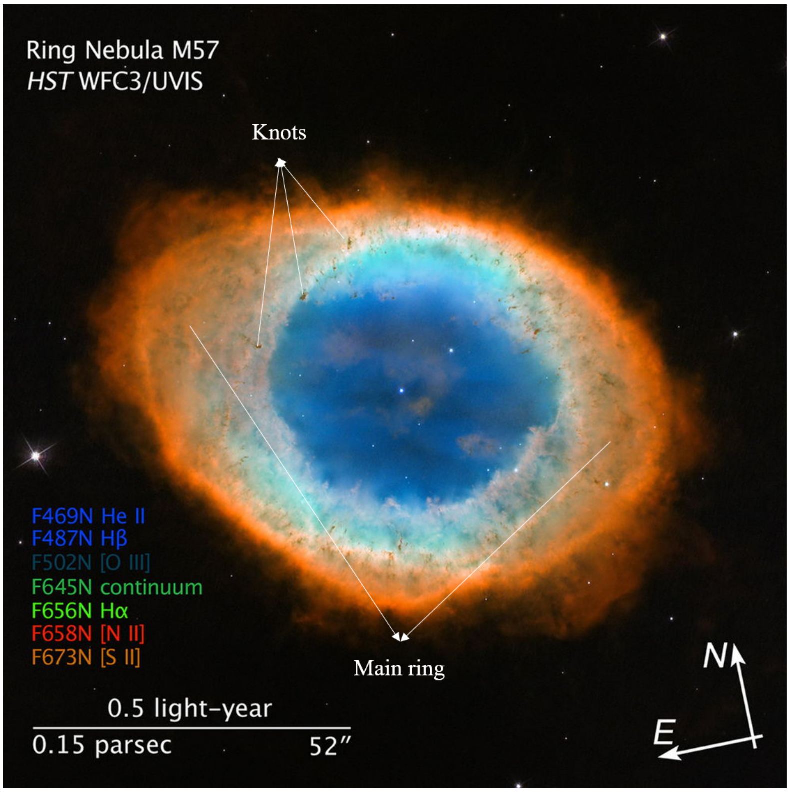

FIGURE 3.6: Composite HST image of NGC 6720. Adapted from NASA, ESA, and Z. Levay (STScI).

3.2.2 Previous Distances estimations

Several distance estimations have been derived for the Ring Nebula. Shklovsky (1956) used the diameter and surface brightness of the nebula and estimated D = 390 pc. Using the emission line Hβ flux density D = 676 pc was found by O'Dell (1962). A distance of 810 pc was estimated using the absorption measurement of the 21 cm emission of the atomic hydrogen by Zuckerman et al. (1980). From the statistical scale of Cahn et al. (1992) D = 872 pc was calculated while D = 1130 pc was estimated by the statistical scale of Zhang (1995). A gravity distance of 1100 pc for the Ring Nebula was obtained by Napiwotzki (2001). Harris et al. (2007) determined the parallax of the CS and derived a distance of $700\pm^{450}_{200}$ pc. Using the extinction corrected Hα surface brightness relation a distance of 900 pc was derived by Frew (2008). Finally, the expansion parallax method was used by O'Dell et al. (2009) to estimate D = $740\pm^{500}_{200}$ pc, while later on O'Dell et al. (2013) improved that value using proper motion measurements from a greater baseline to derive a distance of $720 \pm 30\%$ pc.

3.2.3 Morpho-kinematic model and DMT application

Three scenarios have been proposed in order to explain the 3-dimensional structure of this nebula (Sahai et al., 2012). The first one (i) is a prolate ellipsoid with open ends along the mayor axis, which resemble a barrel (Guerrero et al., 1997; Hiriart, 2004; O'Dell et al., 2007). Then it was proposed (ii) a bipolar nebula nearly pole-on (Bryce et al., 1994; Kwok et al., 2008). Finally (iii) a combination of the two models in which the PN has an open-end barrel-shaped central region that is viewed along its axis was proposed by Sahai et al. (2012).

Our morpho-kinematic model of NGC 6720 follows a simpler approach. Some features are taken from models (i) and (iii). The result is a prolate ellipsoid seen pole-on (see panel *d*, Fig. 3.7). The SHAPE modeled velocity field fitted the PV diagrams of slits 'b', 'e' and 'h' of the [N II] HST image (see panels *b* and *d*, Fig. 3.7). A single homologous velocity law "$V = 37(r/r_o)$ km/s´´ was applied. The 3D SHAPE model along with the synthetic PV diagrams, are shown in Fig. 3.7. Besides the simplicity of the model, the fitting of the synthetic PV diagrams to the observed ones is good.

The specific inputs of the DMT to calculate the distance were:

- 22 proper motion measurements by O'Dell et al. (2009), in a [N II];
- a map size of 500 × 500 arcsec^2;
- the following map resolutions ($\mathscr{re}$) were assumed: 100, 50, 33.3, 25, 20, 16.7, 14.3, 12.5, 11.1 and 10 arcsec.

Distance [pc]	Reference
390	Shklovsky (1956)
676	O'Dell (1962)
810	Zuckerman et al. (1980)
872	Cahn et al. (1992)
1130	Zhang (1995)
1100	Napiwotzki (2001)
$700 \pm ^{450}_{200}$	Harris et al. (2007)
900	Frew (2008)
$740 \pm ^{500}_{200}$	O'Dell et al. (2009)
$720 \pm 30\%$	O'Dell et al. (2013)
$1{,}074 \pm 215$	Present work
828 - 1,320	Present work

TABLE 3.2: NGC 6720 distances values estimated the last 63 years.

The best distance map is found for a resolution of 25 arcsec after the coefficient of variation analysis. The chosen distance and error maps, and the composed image of NGC 6720 with the proper motions as well as the distance and error histograms are presented in Fig. 3.8. The low number of proper motions gives morphologically poor maps of the nebula, thus no kinematic analysis of the distance map is possible. The derived distance from the selected maps is 826 ± 0.39 pc. This value has to be corrected due to the systematic error in the expansion parallax technique (Mellema, 2004). The correction factor, $F = 1.3 \pm 0.26$ was derived using the CS surface temperature (see Fig. 1.7). The final distance estimation for the PN is then $1,074 \pm 215$ pc. Our distance estimation encloses 7 out of 10 values[3] listed in Table 3.2, the upper limits of the most recent individual distance estimations, and all

[3]Excluding our distance and distance range estimation

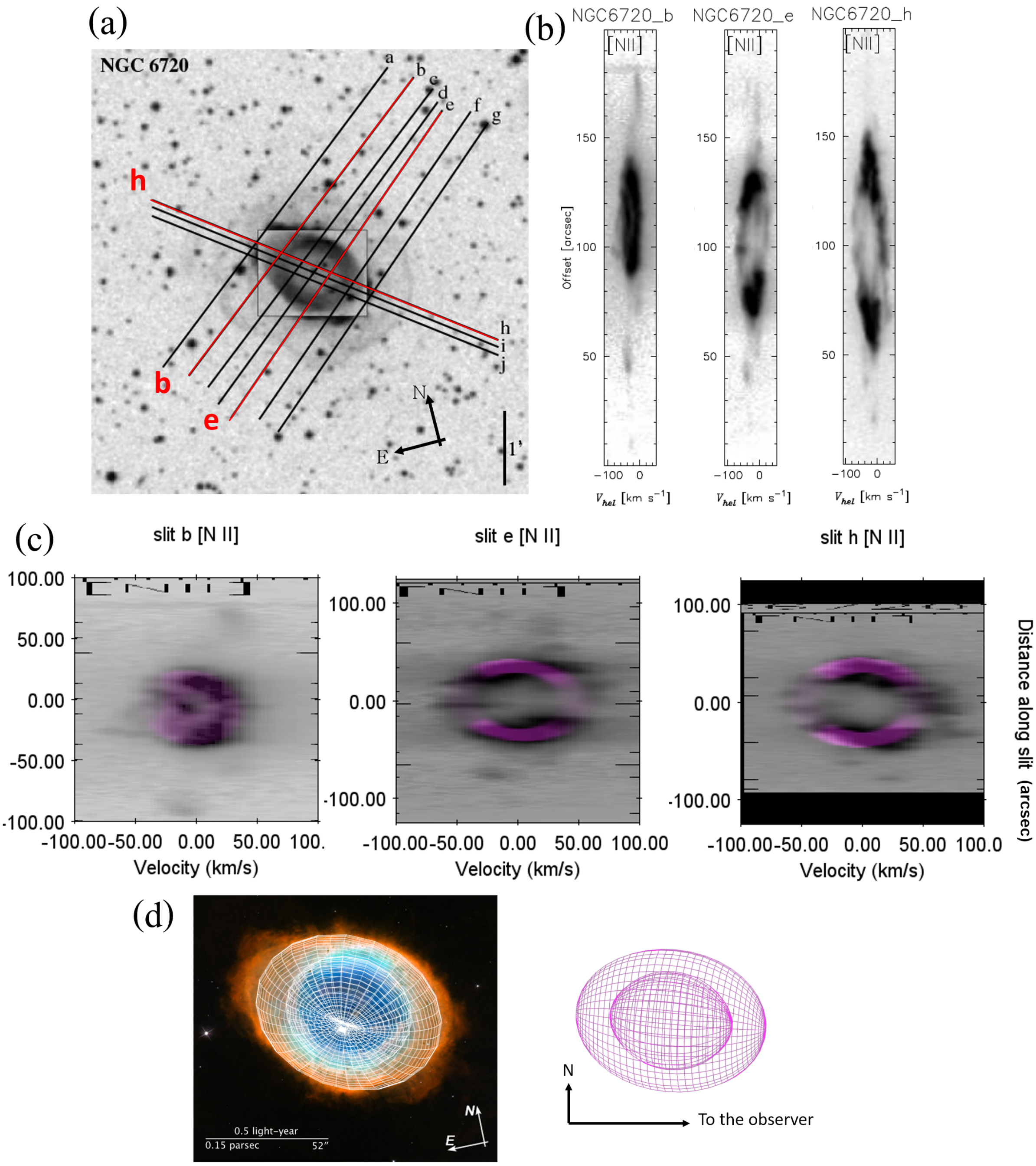

FIGURE 3.7: *Upper panel:* (*a*) Location of the observed slits on NGC 6720 [N II]+Hα image (Bryce et al., 1994), (*b*) Observed PV diagrams of slit 'b', 'e' and 'h' in [N II] (López et al., 2012). *Middle panel:* (*c*) Synthetic PV diagrams overlaid on the observed ones. *Lower pannel*: (*d*) 3D model superimposed on the composed image of NGC 6720 (O'Dell et al., 2013) on the left, and seen edge on the *right*) side.

the statistically derived distances. The 1σ distance range is also provided for NGC 6720 from 828 to 1,320 pc based on the dispersion value of the distance map, $\sigma_D = 246$ pc.

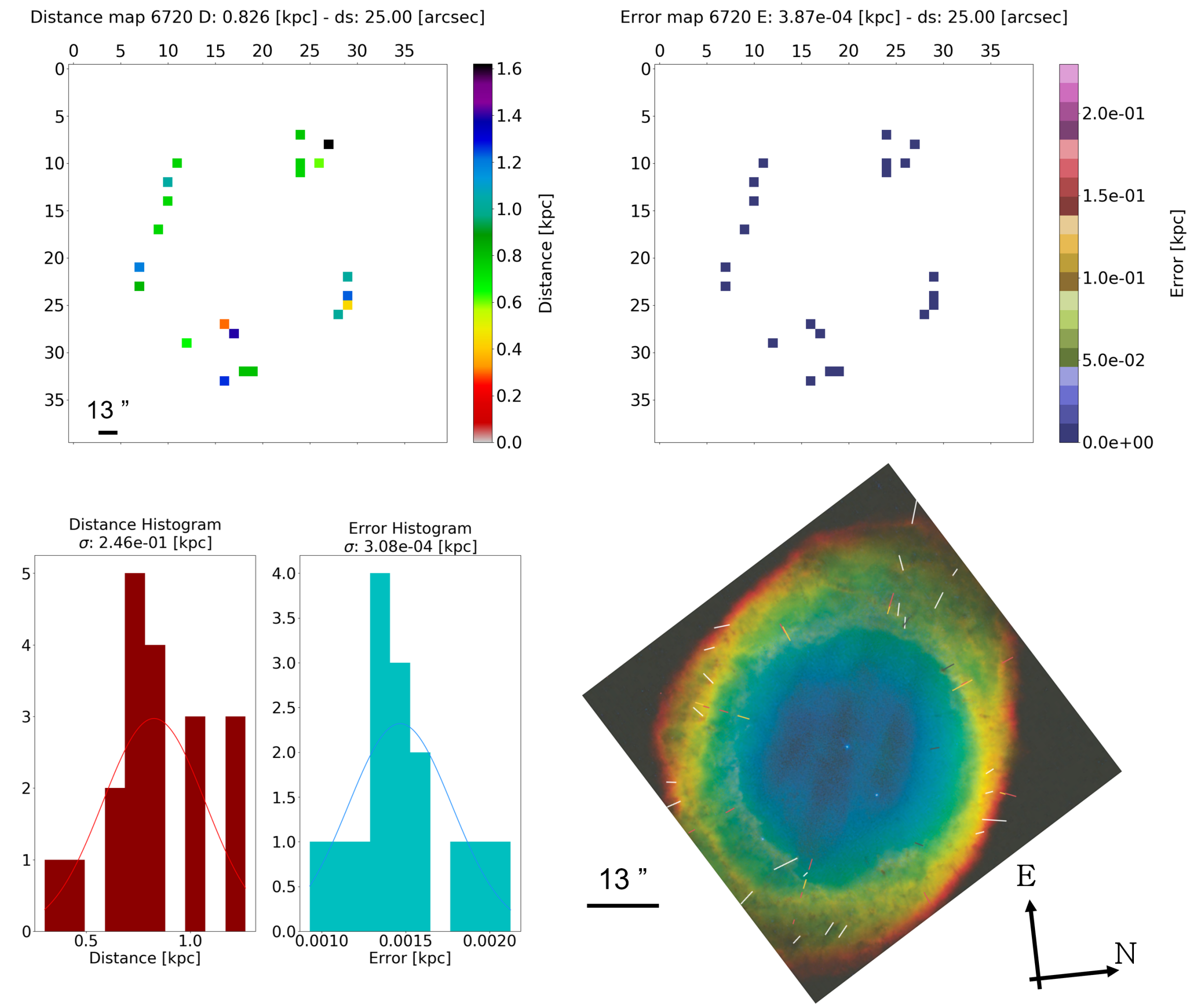

FIGURE 3.8: *Upper panel:* Distance and error maps for re = 25 arcsec. *Lower panel:* the histograms of the maps, and the composed HST image of NGC 6720 with 22 measured proper motions (O'Dell et al., 2009) denoted by the white colored bars.

3.3 BD+30 3639

BD+30 3639 is a dense, compact and young PN located on the Cygnus constellation (RA: $19^h34^45.24^s$; DEC: $+30°30'58.8''$). This PN has an electron density of 11,000 cm^{-3} (Bernard-Salas et al., 2003), a size of 6×4 $arcsec^2$ and an age of 800 yr (Li et al., 2002). The nucleus of BD+30 3639 has been found to be a H deficient Wolf-Rayet (WR) star, with a carbon composition ([WC]-type). [WC]-type stars are similar to massive H deficient WR stars but with significantly lower masses, around 2 $M_\odot$ (Herwig et al., 1999). In particular, the CS of BD+30 3639 has a surface temperature of 42,000 K, a luminosity of $\log(L/L_\odot) = 4.71$ and its wind velocity is 700 km/s (Leuenhagen et al., 1996). Its average electron temperature was reported to be 8,800 K (Bernard-Salas et al., 2003).

3.3.1 Morphological and kinematic description

Bryce & Mellema (1999) established the morphological structure of BD+30 3639 by using resolved, high-spectral resolution observations. These authors found that is composed of a main nebular shell of low-ionization emission, almost axial symmetric, prolate and with an open ended shape, together with a closed shell structure of smaller size and of high-ionization emission. Following these authors, the [O III] expansion velocity (35.5 km/s) is higher than the [N II] (28 km/s) indicating a non homologous expansion law for BD+30 3639. A decreasing expansion velocity function for internal higher ionization ions, and an increasing expansion velocity function for external low-ionization ions were found by Sabbadin et al. (2006). Such a velocity law generates a 'V-shape' velocity profile across the nebula. In this scenario, the expansion velocity is high close to the nebular center but decreases quickly with the nebular radii and finally increases again to the external regions of the nebula. Gesicki et al. (2003) reported 10 Galactic PNe with 'V-shape' velocity profiles based on the emission lines of Hα, [N II] and [O III] (see panel b, Fig. 3.10).

Akras & Steffen (2012) argued the presence of collimated outflows or winds in BD+30 3639, are supported by the CO bullets with expansion velocities of 50 km/s along the polar direction (Bachiller et al., 2000). This high velocity component may be associated with the CO bullets with expansion velocities of 50 km/s along the polar directions (Neiner et al., 2000).

3.3.2 Previous distances

The previous distance estimations for this PN have been revised by Akras & Steffen (2012). In this work, we update this list of distances (see Table 3.3).

3.3.3 Morpho-kinematic model and DMT application

The first morpho-kinematic model of BD+30 3639 was made by Li et al. (2002) considering a tilted ellipsoidal shell that follows a homologous expansion. This model was good enough to find the ratio between the tangential and radial velocity and calculate the expansion parallax distance. Later on, Akras & Steffen (2012) made a more detailed three-dimensional morpho-kinematic model by using SHAPE, to reconstruct the observed PV diagrams in [N II] and [O III], as obtained by Bryce & Mellema (1999). The model presented by Akras & Steffen (2012), have two mesh components as boxy shape ellipsoids (see *a*, Fig. 3.9), one for the high-ionization nebular gas (e.g. [O III]) and another for the gas of low-ionization gas (e.g. [N II] line). According to these authors, two different velocity laws are needed due to the significance difference in the PV diagrams (see Fig.3 and Fig. 4 in Akras & Steffen (2012)), which could not be reproduced with only one velocity field. An additional cylindrical velocity component, in the polar direction, was also used for the [O III] component of the model in order to reproduce the high velocity of [O III] line, likely associated with the bipolar outflows of the PN.

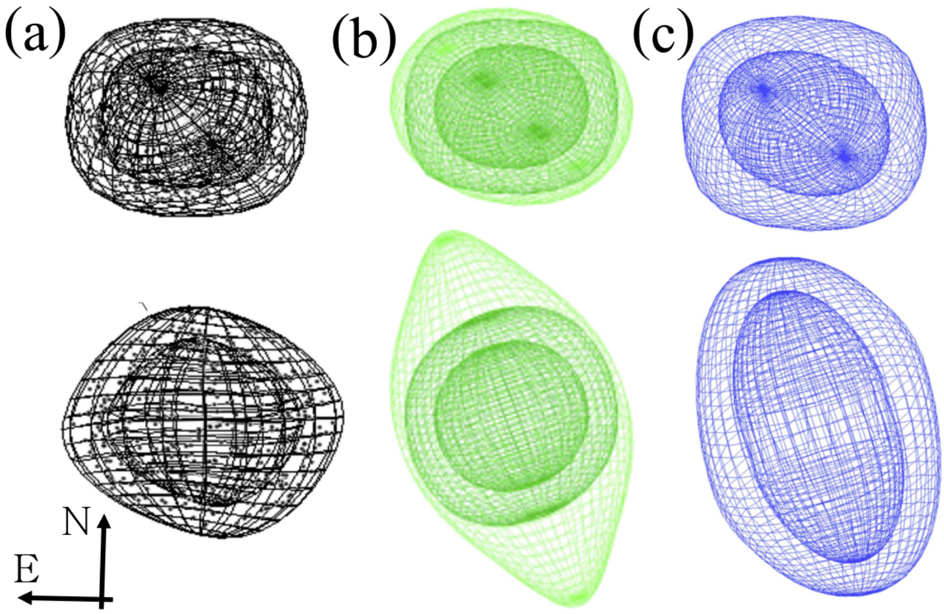

FIGURE 3.9: *Left panel*: (a) (M1) Akras & Steffen (2012) [N II] model of BD+30 3639. *Middle panel:* (b) Freeman & Kastner (2016) [O III] model of BD+30 3639. *Right panel:* (c) (M2) Freeman & Kastner (2016) [N II] model of BD+30 3639. Upper row represents the models as viewed from Earth and the lower row at an inclination of 90°.

Freeman & Kastner (2016) present an even more sophisticated 3D SHAPE model using data from radio, infrared, optical, X-rays and even molecular features as the near-infrared H_2 torus and the CO bullets. For each one of the available spectral data, an ellipsoid model was constructed to fit the observations. Nonetheless, the molecular features required alternative shapes for a good fitting (Freeman & Kastner, 2016).

The main difference between the two SHAPE models above resides in the structure and the velocity fields. Akras & Steffen (2012) used two single ellipsoidal boxy shells for two different kinematic data ([O III] and [N II]) (see *a*, Fig. 3.9), while Freeman & Kastner (2016) modeled an individual elongated ellipsoid shell for [N II] and [O III] (see *b* & *c*, Fig. 3.9). Kinematically the velocity field implemented by Akras & Steffen (2012) is constructed with one homologous law for the [N II] component, and a homologous law (different from [N II]) together with a cylindrical velocity for the [O III] component. Freeman & Kastner (2016) use a single homologous law for both shells. Despite the differences between these two models, both authors reach to a satisfactory fit of the observed data. The explanation for these results lies in the equivalence between the presence of a cylindrical velocity component in a boxy morphology and the absence of the cylindrical velocity component in an elongated ellipsoid morphology. Both approaches successfully explain independently the high velocity [O III] line, commonly associated with the bipolar outflows. Physically, the elongation of the nebula or the presence of a nebular cylindrical velocity component are both supported by the interaction of the collimated outflows with the AGB wind. Hydrodynamic models of PN shaping have also predicted the interaction between collimated jets and fast winds (Huarte-Espinosa et al., 2012).

In this study we use the [N II] models, from Akras & Steffen (2012) and Freeman & Kastner (2016), to obtain the tangential velocity field needed to run the DMT. Note that the observed proper motions were measured in [N II]. We apply this version of the DMT to the model of Akras & Steffen (2012) to test it against the previous version of the code.

For both models (hereafter M1, Akras & Steffen (2012) and M2, Freeman & Kastner (2016)), the next specific inputs for the DMT were used:

- 178 proper motion measurements from Li et al. (2002) in a [N II];
- a map with a dimension of 7×7 arcsec^2;
- the following map resolutions ($\mathscr{re}$): 0.7, 0.35, 0.23, 0.17, 0.14, 0.12 and 0.1 arcsec.

The more appropriate distance estimations for M1 and M2 are found to be 0.23 and 0.12 arcsec, according to the coefficient of variation analysis. The distance and error maps, along with their histograms and the [N II] image of BD+30 3639 showing the proper motions are displayed in Fig. 3.11. The distance maps of M1 and M2 are quite similar, with M2 being more homogeneous. Between the two models, M2 has been found to give lower errors compared to M1. It is worth to emphasize that the previous error map by Akras & Steffen (2012) is similar to our error map for M1. We are not sure if such difference in the distance error is due to the different geometrical and kinematical approach anyway we cannot find a better reason to account for this discrepancy.

Akras & Steffen (2012) identified two SDRs in their distance map (A and B) (see the upper panel of Fig. 3.11). The distances in the SDR A are systematically smaller than the average distance value, while those of the SDR B are systematically larger. A possible systematic error was addressed for SDR A, because of the higher angular expansion in the [N II] line compared to the Hα line in that region (see panel a, Fig. 3.10). Therefore, the overestimation of the angular expansion velocities yields to an underestimation of distance. In the same way, a systematic error was also considered to be a probably explanation for the SDR B, where the angular velocities are lower. Thus, the distance are overestimated (Akras & Steffen, 2012). After comparing the location of the SDRs A and B with the [N II] image of BD+30 3639 (see panel c, Fig. 3.10) no distinguishable features that could be related with the SDR are found in the nebula.

We compare the location of the SDRs A and B from Akras & Steffen (2012) maps with our two distance maps (see middle panel of Fig. 3.11) in order examine for any possible similarities. The SDR A in both distance maps M1 and M2, derived by the current new version of the DMT, encloses several cells with distance below the mean value. The SDR B in both maps encloses only a few cells with distance above the mean value, and for this reason is not considered as a SDR. Although, the location of the SDR B in the M1 error map correspond to a region where the error is 45 times higher than the error of M1. Such error also points towards that the SDR B could be the result of a systematic error in the observations.

We have identified an additional SDR in both maps, namely the SDR C, which also exhibits distance values below the mean. After comparing the location of the SDR C with the [N II] image of BD+30 3639, no nebular features associated with the SDR C were found. We used the plot of the expansion rate in the Hα and [N II] lines as a function of the PA (Fig. 12 of Akras & Steffen (2012)) to verify if the expansion of [N II] is systematically higher than one of the Hα for the location of the SDR C as in the case of the SDR A (see panel a, Fig. 3.10). Effectively, in the SDR C, occurs the same as in

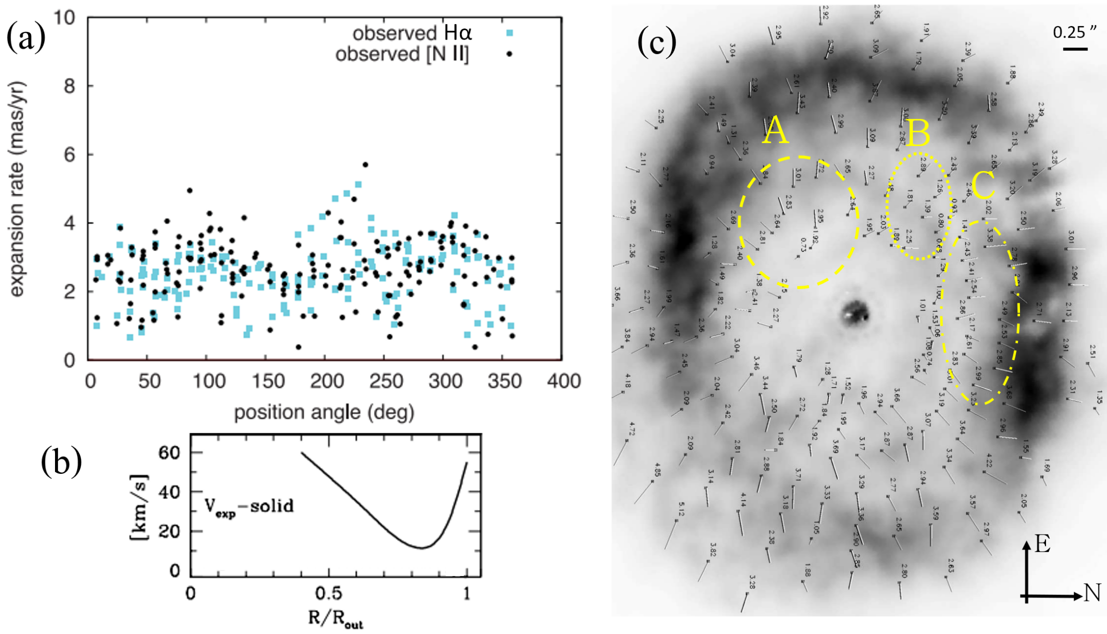

FIGURE 3.10: *Panel a:* Distribution of the BD+30 3639 proper motion as a function of the PA with the values of the Hα (blue) and the [N II] (black) emissions (Li et al., 2002). Image taken from Akras & Steffen (2012). *Panel b:* Modeled radial velocity profile for PN 359.9-04.5 illustrating the 'V-shape' velocity profile. Plot adapted from Gesicki et al. (2003). *Panel c:* [N II] image of BD+30 3639 with the location of the 178 proper motions and the SDRs A, B and C. Adapted from Li et al. (2002).

the SDR A. Hence, it is probable that the underestimation of distance in SDR C is due to the overestimation of the angular expansion velocity in that region.

Since both resultant distance maps, for M1 and M2, display the same SDRs, neither the cylindrical velocity component introduced by Akras & Steffen (2012) nor the elongated model used by Freeman & Kastner (2016) can explain the deviations from the mean distance. Thus, we reckon that the possibility of some errors in the observations are very likely after this analysis.

The previous distance map for BD+30 3639 by Akras & Steffen (2012) and our distance map (M1) are very alike (see upper panel of Fig. 3.11), presenting the dispersed deviated cells in similar locations as well as the SDRs. Therefore, the distance estimations are also very alike and the difference between the two is probably due to the outliers. The outliers exclusion is an option that was not available in the previous version of the technique used by Akras & Steffen (2012).

The distance of BD+30 3639, from M1, is found to be $1.04 \pm 5.5 \times 10^{-3}$ kpc and from M2 it is $1.01 \pm 6.7 \times 10^{-10}$ kpc. These values must be corrected due to the systematic difference in matter and pattern velocity (Mellema, 2004). The correction factor (F) of BD+30 3639 is 1.3 ± 0.2, a value for which Mellema (2004) and Schönberner et al. (2005) agree (see, Fig. 1.7). After the correction, the final distances are 1.35 ± 0.21 kpc and 1.32 ± 0.2 kpc for M1 an M2, respectively. These values agree with 7 out of 16 distance estimation[4] listed in Table 3.3. Only one of them is a statistical determination

[4]Excluding our distance and distance range estimation.

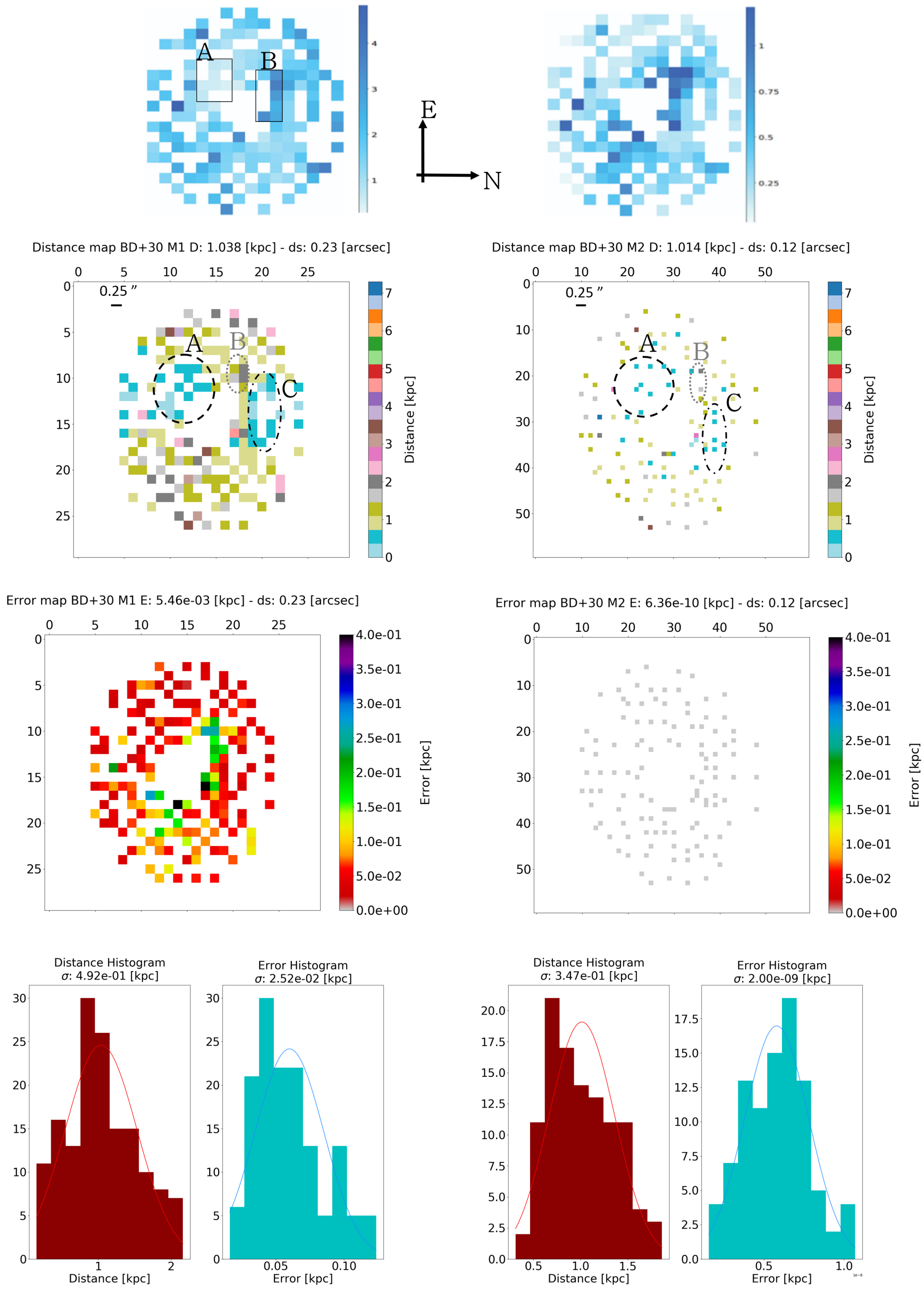

FIGURE 3.11: Distance and error maps along with their respective histograms for BD+30 3639. M1 in the left panels and M2 in the right ones. At the top are presented the distance and error maps derived by Akras & Steffen (2012). SDRs A, B and C are presented in all distance maps.

Distance [kpc]	Reference
4.15	O'Dell (1962)
0.73	Daub (1982)
0.6	Pottasch (1984)
$2.8^{+4.7}_{-1.2}$	Masson (1989)
1.16	Cahn et al. (1992)
2.68 ± 0.81	Hajian et al. (1993)
1.84	Van de Steene & Zijlstra (1994)
1.85	Zhang (1995)
1.5 ± 0.4	Kawamura & Masson (1996)
1.20 ± 0.12	Li et al. (2002)
0.67	Phillips (2002)
2.14	Phillips (2004)
1.3 ± 0.2	Mellema (2004)
2.57	Phillips (2005)
1.2 ± 0.2	Schönberner et al. (2005)
1.46 ± 0.21	Akras & Steffen (2012)
1.35 ± 0.21	Present work - M1
1.32 ± 0.20	Present work - M2
0.86 - 1.84	Present work - M1
0.97 - 1.67	Present work - M2

TABLE 3.3: BD+30 3639 distance determinations.

by Cahn & Kaler (1971) while for the remaining 6 the expansion parallax technique was applied. The 1σ distance range is from 0.86 to 1.84 and between 0.97 and 1.67 kpc, for both M1 and M2 models, respectively, based on their standard deviations ($\sigma_{M1} = 0.49$ and $\sigma_{M2} = 0.35$ kpc). Additionally, the statistical distance of Van de Steene & Zijlstra (1994) is compatible with the 1σ distance range of M1. Regardless of the structural and kinematic differences of M1 and M2, the distance estimations of both models are almost equal. Therefore, it is not possible decide which model better describes BD+30 3639.

3.4 NGC 6302

The Butterfly Nebula is the common designation for NGC 6302 along with the Bug Nebula due to its bipolar appearance. It is located in the Scorpious constellation (RA: $17^h13^m44.21^s$; DEC: $-37°06'15.9''$). The first detection of the CS in this nebula was made by Szyszka et al. (2009), who found a hot star with a mass of 0.64 $M_\odot$ close to the WD cooling track. Its surface temperature is still uncertain, but it is probably higher than 200,000 K in order to account for the detection of highly ionization species. Barral et al. (1982) derived an electron temperature of $20.4 \pm 4{,}000$ K, from the relative widths of the [N II] and Hα emission-lines profiles of the bipolar lobes. The CS is obscured by a massive circumstellar torus of dust, of approximately 2 $M_\odot$, formed between 2,900 and 7,500 yr ago (Peretto et al., 2007). Close to the torus, the electron density is around 80,000 cm^{-3} and falls roughly to 1,000 cm^{-3} in the lobes (Barral et al., 1982). The dynamical age of the bipolar nebula was estimated to be 2,200 yr, by Meaburn et al. (2008), and $2,250 \pm 35$ yr by Szyszka et al. (2011). This implies that the torus was formed before the nebula and it is responsible for its morphology.

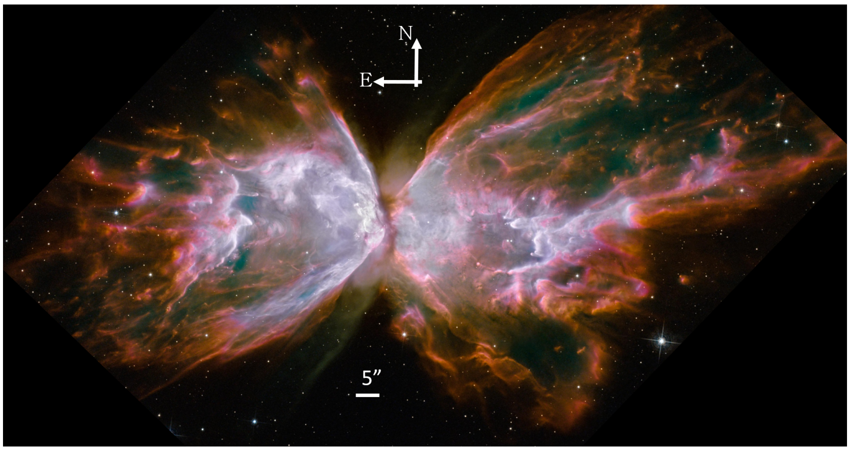

FIGURE 3.12: Composite HST image of NGC 6302, [S II] in white, [N II] in orange, Hα in brown, [O III] in cyan, He II in blue and [O II] in purple. Image obtained by the NASA, ESA, and the Hubble SM4 ERO Team.

3.4.1 Kinematic and morphological description

The complex morphology of NGC 6302 is portrayed in several emission lines in the WFC3 HST image of (Szyszka et al., 2011), as Fig. 3.12. Two prominent lobes emerge from the torus in the east and west directions. The lobes and the waist are characteristic features of a bipolar PN (Balick & Frank, 2002), hence the Butterfly Nebula is a common reference for this morphological type.

A homologous expansion velocity law has been confirmed in the lobes by Meaburn et al. (2005), by using morpho-kinematic modeling of spatially resolved optical-line profiles plus the proper motion measurements of 15 knots in the northwestern lobe. Meaburn et al. (2005) reported outflow velocities ≥ 600 km/s for that lobe. A homologous velocity law was also reported by Peretto et al. (2007) in the velocity component of the CO emission close to the expanding torus. The torus is expanding at ~ 8 km/s (Peretto et al., 2007). Szyszka et al. (2011) argue that the homologous expansion of the lobes can be extended at the innermost parts of the PN and that the proper motion effectively point towards the CS. The latter supports a common kinematic origin for the lobes and the torus. The inner nebular regions present evidence of recent additional acceleration, more pronounced to the southern region probably due to the overpressure after the beginning of the photoionization (Szyszka et al., 2011).

3.4.2 Previous distances determinations

Various distance estimations have been made for NGC 6302 using several techniques. By means of an empirical relationship between the nebular ionized mass and nebular radius a distance of 0.415 kpc was derived by Maciel & Pottasch (1980). Rodríguez & Moran (1982) estimated D = 2.4 kpc using the Shklovsky (1956) method. Later, Rodríguez et al. (1985) calculated D = 1.7 kpc by relating the optical depth in the radio wavelengths range and the electron density of the PN. Due to the lack of detection of an interstellar polarization component in the polarization of the PN, King et al. (1985) suggested D = 1.5 kpc. Gómez et al. (1989) used two different techniques to calculate the distance to NGC 6302, based on the radio wavelengths proper motion measurements of the nebular core and using the measurements of the pressure-broadening of radio recombination lines. The former method gave a distance of 0.8 ± 0.3 kpc and the latter D = 2.2 ± 1.1 kpc. A distance equal to 0.91 kpc was established by Shaw & Kaler (1989) using emission-line photometry of the PN. Later on, Gómez et al. (1993) applied the expansion parallax method to the VLA angular expansion measurements and ended up with D = 1.6 ± 0.6 kpc. Meaburn et al. (2005) reported an expansion parallax distance of 1.04 ± 0.16 kpc by comparing images with a baseline of 46 yr. Then, Meaburn et al. (2008) determined the expansion of 15 knots and estimated a distance of 1.17 ± 0.14 kpc. Finally, Lago & Costa (2014) used high-dispersion long slit velocity profiles of forbidden emission lines in different angular positions, and gave the most recent distance estimation, 0.805 ± 0.143 kpc.

3.4.3 Morpho-kinematic model and DMT application

The first attempt to model the 3D structure of NGC 6302 was carried out by Meaburn et al. (2005) assuming a homologous velocity law. The code SHAPE was used to reproduce successfully, the PV diagrams for the slits 'a' to 'c' shown in Fig. 3.13. Unfortunately, it was not possible to use this previous model to estimate the distance by means of the DMT due to the difference in the SHAPE version.

Therefore, we decided to model again the eastern lobe of the nebula considering an extended 3D conical shell (see, Fig. 3.13), due to the available proper motion velocity field measured for this lobe by Szyszka et al. (2011). Our 3D morpho-kinematic model reproduces the [N II] PV diagrams for the slit 'a' and 'b' using a single velocity law, $V = 28(r/r_o)$ km/s. The synthetic PV diagrams as well as the 3D model are presented in Fig. 3.13. Since the observed PV diagrams give information only for the north side of the selected lobe, we do not have constrains for the morphology of the southern side to our 3D model. Besides this lack of constrains for the whole lobe (additional slits measurements in the south side of the lobe) we used the resultant 3D model to determine NGC 6302 distance. The synthetic PV diagrams adequately reproduced the features, although without take into account the clumps and voids that escapes from our simple modeling approach.

The following specific entries for the DMT were used:

- 200 proper motion measurements, by Szyszka et al. (2011), in a [N II];
- as the size of the mape is 65×65 arcsec^2;
- the following map resolutions (re): 13, 6.5, 4.3, 3.25, 2.6, 2.17, 1.86, 1.63, 1.44 and 1.3 arcsec.

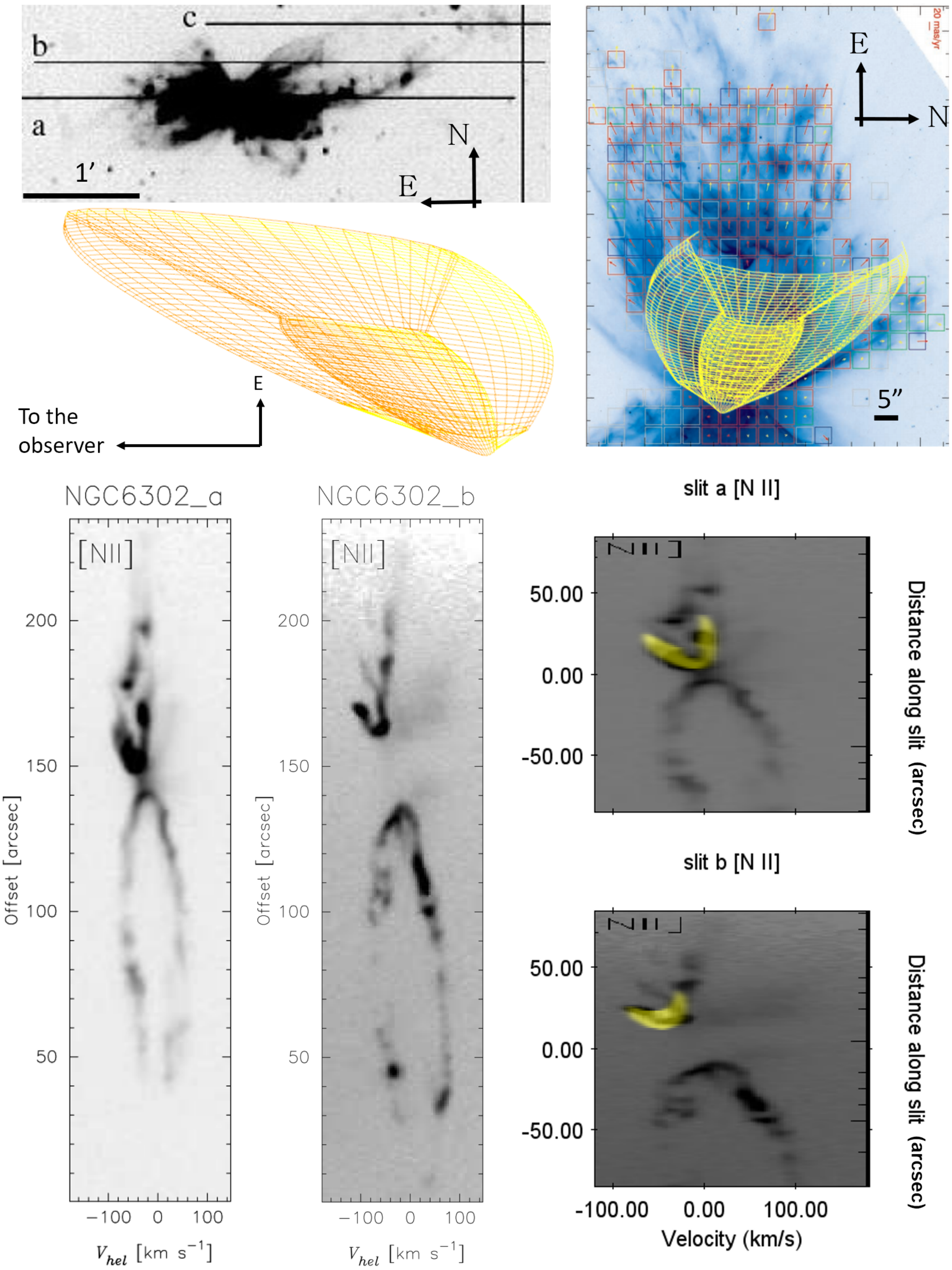

FIGURE 3.13: *Upper panel:* slit position overlaid on the Hα-[N II] image of the nebula plus the modeled 3D conical shell, for a portion of the eastern lobe of NGC 6302, and 3D model properly oriented and overlaid on the eastern lobe proper motion velocity field (Szyszka et al., 2011). *Lower panel:* observed and synthetic PV diagrams of slit 'a' and 'b' (Meaburn et al., 2005).

A resolution of 2.6 arcsec was chosen because it gives the best distance estimation of NGC 6302, after, of course, the use of the coefficient of variation analysis. The derived distance and error maps along with their histograms are presented in Fig. 3.14.

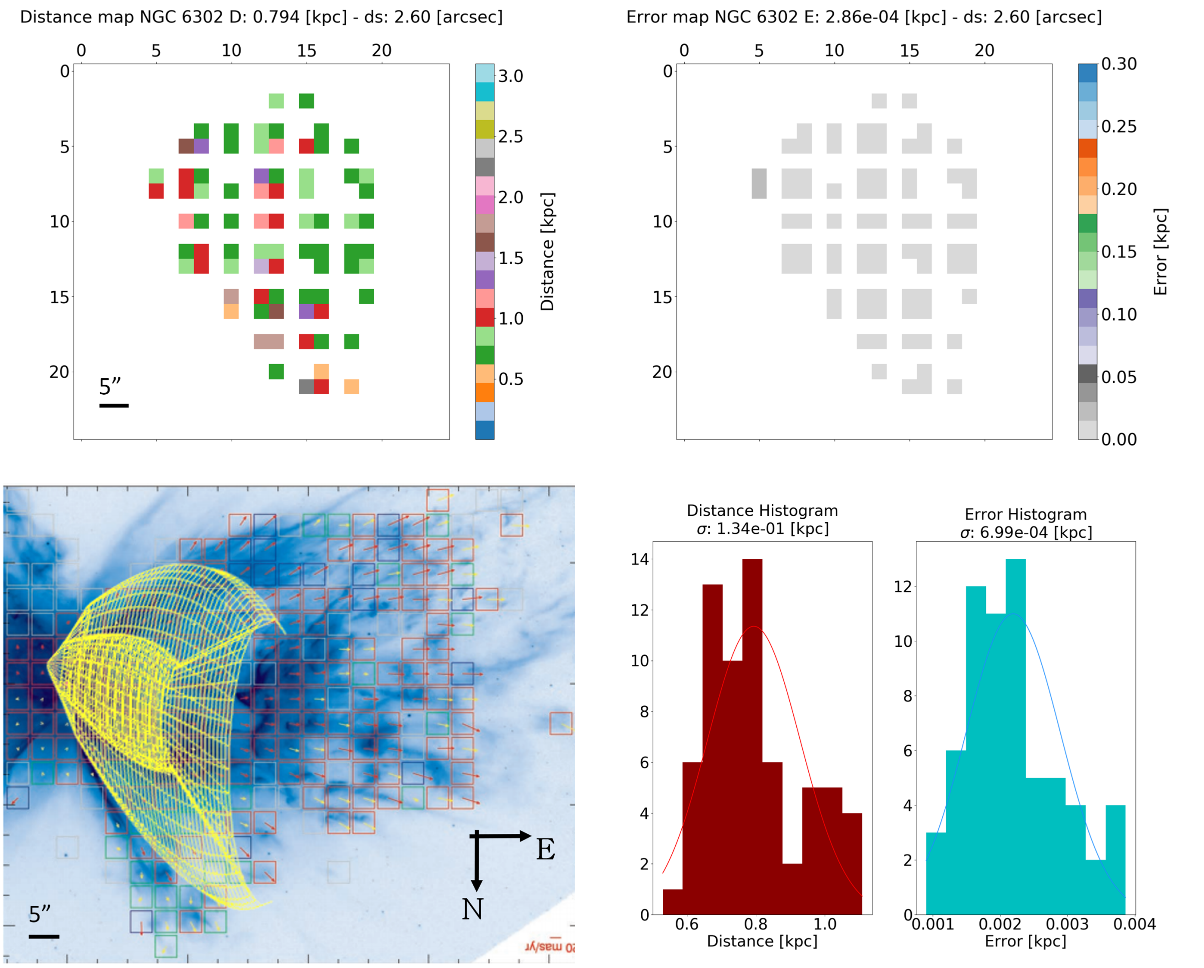

FIGURE 3.14: *Upper panel:* distance and error maps of NGC 6302 at a resolution of 2.60 arcsec. *Lower panel:* proper motion velocity field of the eastern lobe of NGC 6302 and the histograms of the distance and error maps.

No apparent SDRs are identified for this nebula, but only spread cells with distance values above the mean value. Such cells have no correspondence with the error map, which is homogeneous. No kinematic analysis is developed for this PN, first due to the lack of SDRs and second because the 3D model could not properly constrain the entire nebula. The spread cells above the mean distance are probably due to the accuracy of the measured proper motions. Perhaps a second model component could explain the more extended outflow in the eastern direction, but the PV diagrams do not provided enough information to constrain this additional component.

The distance calculated by the DMT, with a resolution of $re = 2.6$ arcsec, is found to be 0.79 $\pm 2.9 \times 10^{-4}$ kpc. A correction factor, $F = 1.3 \pm 0.26$ was derived from the CS surface temperature relationship in Fig. 1.7.. The corrected distance estimation for NGC 6302, by using the DMT, is 1.03 $\pm$ 0.21 kpc. No 1σ distance range is provided for this nebula because the final distance error is larger than σ. Despite the few constrains for the morpho-kinematic model of NGC 6302, the simple model and the small portion of the eastern lobe simulated, the distance estimation provided by the DMT is in agreement with 7 out of 11 distance estimations[5] listed in Table 3.4.

Distance [kpc]	Reference
0.415	Maciel & Pottasch (1980)
2.4	Rodríguez & Moran (1982)
1.7	Rodríguez et al. (1985)
1.5	King et al. (1985)
0.8 ± 0.3	Gómez et al. (1989)
0.91	Shaw & Kaler (1989)
2.2 ± 1.1	Gómez et al. (1989)
1.6 ± 0.6	Gómez et al. (1993)
1.04 ± 0.16	Meaburn et al. (2005)
1.17 ± 0.14	Meaburn et al. (2008)
0.805 ± 0.14	Lago & Costa (2014)
1.03 ± 0.21	Present work

TABLE 3.4: NGC 6302 distances determinations.

3.5 The Firework Nebula

The Firework Nebula or GK Persei is a nova remnant in the constellation of Perseus (RA: $3^h31^m12^s$; DEC: $+43°54'15.0''$) formed by material ejected during an outburst in a cataclysmic variable star (CV). CVs are interacting binary systems that consist of, a WD that accretes mass from a MS star, which has filled its Roche lobe. Eventually, an outburst eruption on the surface of the WD is generated by thermonuclear runaway of the accretion material (Warner, 1995). Classic novae eject large amount of mass, around 10^{-4} $M_\odot$ (Bildsten & Deloye, 2004) at velocities of the order of 5×10^2 to 5×10^3 km/s (Bode & Evans, 2008). The CV of GK Persei consists of a evolved late type star (K2IV) (Crampton et al., 1986) together with a magnetic WD (Sabbadin & Bianchini, 1983). This binary system presents the second orbital period known for a classical nova system, of 1.9968 days (Morales-Rueda et al., 2002). The remnant of this mass ejection has a total mass of 7×10^{-5} $M_\odot$ (Pottasch, 1959) and an electron temperature greater than 2.5×10^4 K (Williams, 1981). The shell of the nebula has been described as clumpy, asymmetric and boxy (Anupama & Kantharia, 2005) (see, Fig. 3.15), and it is interacting with the environment, suffering a deceleration at the south-west region caused by a shock interaction (Seaquist et al., 1989; Bode, 2004).

3.5.1 Previous distance estimations

Some distance estimations have been made for GK Persei. From the observed expansion of the nova shell, McLaughlin (1960) derived D = 470 pc. Duerbeck (1981) found D = 525 pc, by using the distance-line-strength relationship. Distances of 726 pc and 337 pc were derived by Sherrington & Jameson (1983) and Warner (1987), respectively, by using the

[5]Excluding ours.

K-band magnitude of the secondary star, by means of the Bailey method. The latter is a method to calculate distances to CVs that uses the K magnitude and the surface intensity in the K band of the primary star, and the radius of the secondary star (Bailey, 1981), but since the K-band magnitude of the star is not easy separable from the disc contribution, this leads to different distance estimations (Liimets et al., 2012). A distance of 455±30 pc was derived by Slavin et al. (1995) using optical imaging and applying the expansion parallax technique. Downes & Duerbeck (2000) estimated a nebular expansion parallax distance of 460^{+69}_{-59} pc. From the 2MASS K-band magnitudes and the updated version of Bailey method, a distance of 420 pc was calculated by Barlow et al. (2006). Due to variation of the overall shape of the nebula as a function of D, a distance that better adjusts to the spherical shape of the nebula is 400 ± 30 pc (Liimets et al., 2012). Using precise astrometric parallaxes, an astrometric distance to GK Persei of 477^{+28}_{-25} pc was calculated by Harrison et al. (2013).

3.5.2 Morpho-kinematic model and DMT application

Harvey et al. (2016) made a morpho-kinemtaic model of the knotty structure of the nova remnant of GK Persei using SHAPE. The model was based on high-resolution spectroscopic observations and imaging along with optical archival data from several epochs and facilities. 115 knots were modeled as individual three-dimensional cylinders whose specific expansion velocities, distance from the CS, PA and inclination are associated with the measured proper motions of Liimets et al. (2012). Harvey et al. (2016) also modeled the overall shape of the knots distribution, not as a warped spherical shell as Liimets et al. (2012) considered, but as a cylindrical shell whose symmetry axes are related to the inclination of the central binary system. Additional bipolar features were included, to account for the knots that are not enclosed by the barrel. The best fit of the data, indicates that the shell has a cylindrical shape, not a spherical one (Harvey et al., 2016).

Applying the DMT to the remnant of GK Persei, we used the three-dimensional knots from Harvey et al. (2016), and the 117 proper motions measured by Liimets et al. (2012). Additionally, the observational error of the proper motions are available, and therefore they are included in our distance determination with the DMT. The axisymmetric distribution of these knots is represented in Fig. 3.15 overlaid on the Hα-[N II] image of GK Persei, which displays the measured proper motions.

The specific inputs for the DMT for the application of the DMT to GK Persei:

- 117 proper motion measurements by Liimets et al. (2012), in a [N II];
- a map of 130×130 arcsec^2;
- the following map resolutions ($\mathscr{re}$): 13, 6.5, 4.3, 3.25, 2.6, 2.17, 1.86, 1.63, 1.44, 1.3, 1.18 and 1.08 arcsec.

The most suitable distance for GK Persei is obtained by using the same procedure as for the previous nebulae at 1.44 arcsec. The distance and error maps, along with the histograms, are presented in Fig. 3.15. The distance and the error maps display faithfully the distribution of the knots. The error map is dominated by the observational error.

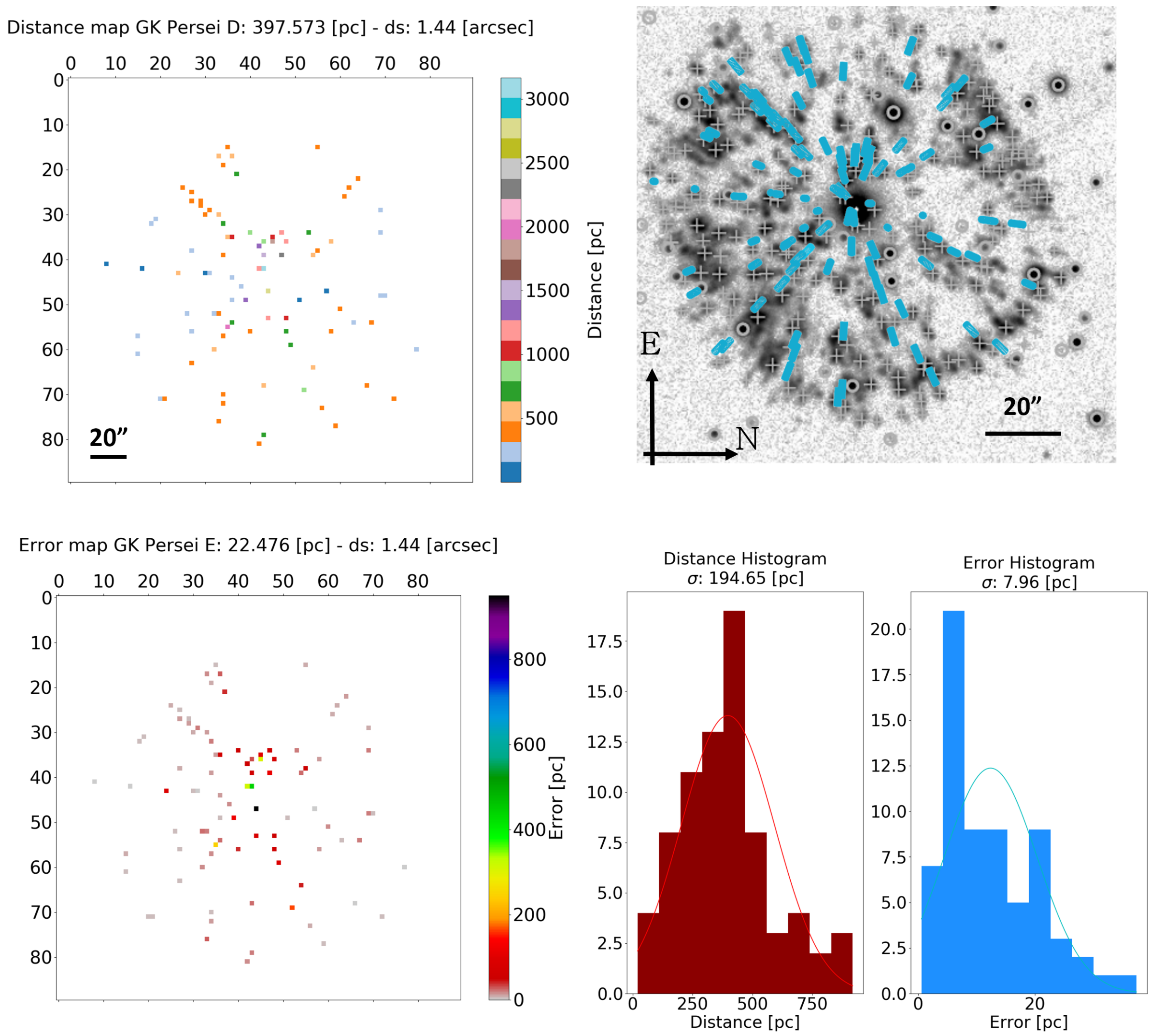

FIGURE 3.15: *Upper panel:* Distance map of GK Persei (*left*) and the Hα-[N II] image of the nova remnant (Liimets et al., 2012) (*right*). *Middle panel:* Error map (*left*) and the modeled 3D knots (Harvey et al., 2016) overlaid on the Hα-[N II] image, also displaying the location of the measured proper motions (Liimets et al., 2012). *Lower panel:* Distance and error histograms.

Most of the cells in the distance map are within the 1σ distance value except for some cells in the center of the map, which present high distances. The same cells with high distance values are also found to exhibit high errors. Therefore, the distance deviation of these cells could be due to the low accuracy of the proper motion measurements, at the center.

The distance estimated for GK Persei, from the DMT map, with a resolution of 1.44 arcsec is 398 ± 23 pc. Note that the correction factor (F) previously used have been studied only for expanding PNe. A direct extrapolation of the derived correction factors for PNe to nova remnants should be properly studied. Nevertheless, the application of the expansion parallax technique of the DMT in a nova remnant requires a correction as in PNe, because the ejecta of nova remnant are partially photoionized due to the hot star of the CV system and also by shocks interactions with the stellar winds. In such scenario, the pattern (shocks plus ionization fronts) velocity and matter (gas) velocity could diverge. Therefore, as a first approximation, we can apply the correction factors derived from PNe to GK Persei, but there is no available information about the surface temperature of the CS star. The latter is needed in order to define the value for F, either using the correction method of Mellema (2004) or Schönberner et al. (2005). In addition to the mean distance value we also provide the 1σ distance range for GK Persei, which is 203 - 592 pc, based on σ_D = 195 pc. Our final distance for GK Persei agrees with 5 out of the 9 distance estimations[6] listed in Table 3.5, while our 1σ range encloses 8 of these 9 estimations. The distance we derived is consistent with the previous expansion parallax distances of Slavin et al. (1995) and Downes & Duerbeck (2000), for which no correction was applied either. Moreover, the upper limit of our distance estimate is found to be 32 pc lower than the lower limit of the trigonometric distance of Harrison et al. (2013). This fact hints for a lower correction factor and indicates that our estimated distance is quite good as a trigonometric distance.

Distance [pc]	Reference
470	McLaughlin (1960)
525	Duerbeck (1981)
726	Sherrington & Jameson (1983)
337	Warner (1987)
455± 30	Slavin et al. (1995)
460^{+69}_{-59}	Downes & Duerbeck (2000)
420	Barlow et al. (2006)
400 ± 30	Liimets et al. (2012)
477^{+28}_{-25}	Harrison et al. (2013)
398 ± 23	Present work
203 - 592	Present work

TABLE 3.5: GK Persei distances determinations.

3.6 η Carinae outer ejecta

η Carinae is a binary system with an orbital period of 5.5 yr (Damineli et al., 2000), located in the constellation of Carina (RA: $10^h45^m03.55^s$; DEC: $-59°41'04''$). It is a widely studied object for which Davidson & Humphreys (2012) made a formidable summary. η Carinae is classified as a luminous blue variable star (LBV) (Davidson & Humphreys, 2012). LBVs suffer extensive mass-loss and show strong optical H and He I lines, generally associated with a P Cygni absorption. This is an extremely luminous and massive system, with a luminosity of $\log(L/L\odot) \simeq 6.7$, an estimated mass ≥ 90 $M_\odot$. Its mass-loss rate is of $\sim 10^{-3}$ $M_\odot$/yr.

Surrounding η Carinae there is a composite circumstellar nebula made principally of a inner bipolar structure called the 'Homunculus', and an outer ejecta, whose main features are labeled in Fig. 3.16. It is generally accepted that the Homunculus was ejected in the

[6] Excluding ours estimates.

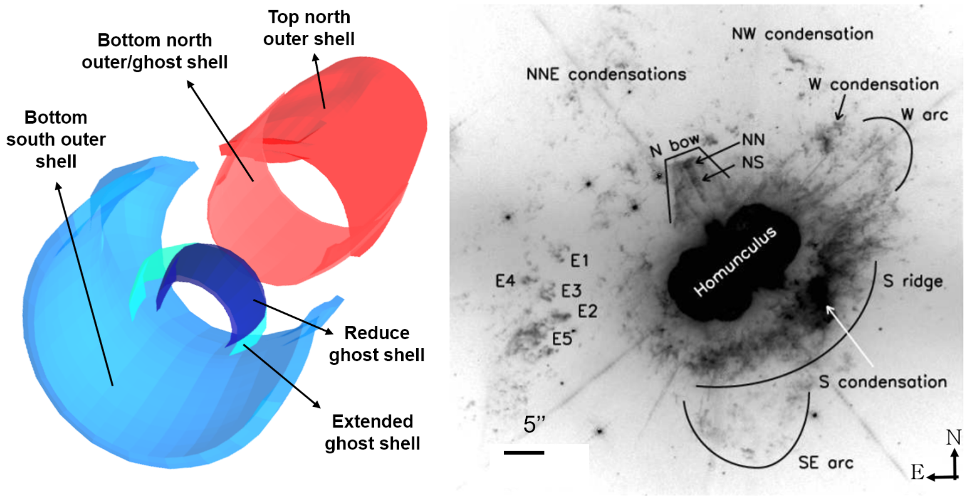

FIGURE 3.16: *Left panel:* Illustration of SHAPE model of the outer ejecta without the bowshock oriented towards Earth (Mehner et al., 2016). *Right panel:* HST WFPC2 image of η Carinae at the [N II] λ6584 and the redshifted Hα emission displaying the labels of prominent features of the outer ejecta. Adapted from Kiminki et al. (2016).

latest eruption of the object in the 1840s, while the southern (S) features were likely formed a little early or later than the great eruption (Davidson & Humphreys, 2012). The eastern (E1 to E5) and the north-northeastern (NNE) condensations were probably formed from an eruption in the 1200s, while the western (W) and the northwestern (NW) condensations were likely originated in the 1500s one (Kiminki et al., 2016). The outer ejecta is largely asymmetric and consists of a variety of individual structures of different sizes, morphologies and velocities distributed in a region with a size of 0.34 pc (Weis, 2001). The electron density of the outer ejecta has been estimated as being 10^4 cm^{-3}, by using the line ratio of the [S II] doublet lines (Weis, 2005), and assuming an electron temperature of 14,000 K (Dufour et al., 1997). The expansion velocities of some of its structures reach up to 2000 km/s, where the typical values are between 400 to 600 km/s (Weis, 2001; Kiminki et al., 2016). Besides the random and irregular distribution of all these structures, their expansion displays a bidirectional motion pattern as in the Homunculus nebula (Weis, 2012).

3.6.1 Previous distance determinations

Several expansion parallax distances have been obtained for η Carinae: 2.2$\pm$0.2 kpc (Allen & Hillier, 1993); 2.3$\pm$0.3 kpc (Meaburn et al., 2005); 2.25$\pm$10% kpc (Davidson et al., 2001); 2.3 kpc (Smith, 2002) and 2.35$\pm$0.05 kpc (Smith, 2006). Walborn (1995) used the luminosities of O-type stars in the ionizing cluster Trumpler 16, close to η Carinae, and he got a distance of 2.25 kpc. Later, Davidson & Humphreys (1997) derived D = 2.3$\pm$0.2 kpc taking into consideration the photometric distance to Trumpler 16.

3.6.2 Morpho-kinematc model and DMT application

A 3D morpho-kinematic multicomponent SHAPE model for the outer ejecta of η Carinae was made by Mehner et al. (2016), based on large-scale optical integral field unit observations. Several large-scale structures were modeled taking into account the apparent spatial association with the observational data, and assuming homologous expansion velocity laws. One of the modeled components, the bowshock, was modeled using the hydrodynamic SHAPE mode, which does not generate the simulated tangential velocity vectors. So, the bowshock component was not taken into account in our analysis.

All the modeled components for which the DMT was applied are indentified in Fig. 3.16. The observations of Mehner et al. (2016) revealed a large shell-like emission feature, whose velocity ranges from -2200 km/s in the south-east side from the CS to +2000 km/s in the north-west direction from the CS. This outer shell was modeled as a bent cylinder that encloses the whole Humunculus nebula, with mainly two components: the bottom-south and top-north outer shells (see left panel, Fig. 3.16). The outer shell components mentioned before, modeled following features of the outer ejecta of η Carinae: the S ridge, the S condensations and the W arc, whereas the E, W and NW condensations were not included in the model (see, Fig. 3.16). Mehner et al. (2016) identified 'horn' features (which are expanding faster than the southern Homunculus lobe) as the ghost shell, discussed by Currie et al. (2002). The ghost shell is a high-velocity, spatially extended emission feature detected in multiple Balmer and forbidden lines ([N II], [S II] and [Ar III]) lying outside the southern Homunculus lobe. Its origin is likely due to the forward shock of the fast stellar wind of the great eruption against the older slow massive stellar wind (Currie et al., 2002). Mehner et al. (2016) modeled this structure as two aligned shells in the front of the SE Homunculus. Behind the northern Homunculus lobe, structures with projected velocities higher than +400 km/s were identified and modeled by Mehner et al. (2016). However, Mehner et al. (2016) state that it is unknown if this component is a counterpart of the ghost shell or part of the outer shell (see, bottom-north outer/ghost shell Fig. 3.16).

Because of the high complexity of η Carinae, first we applied the DMT to the whole model (all the components together except, for the bowshock) and then, to each component separately. In both cases, the inputs of the DMT were:

- 792 proper motion measurements by Kiminki et al. (2016), in Hα+[N II];
- as the size of the map is 70×70 arcsec^2;
- for these map resolutions ($\mathscr{re}$): 7, 3.5, 2.33, 1.75, 1.4, 1.17, 1, 0.86, 0.78 and 0.7 arcsec.

After analyzing the coefficients of variations, the best distance maps for the first case was found to have a 0.7 arcsec resolution. The distance and error maps as well as the histograms are presented in Fig. 3.17. The DMT distance is 4.7 kpc, which is not consistent with the previous distance estimations (see Table 3.7). As the distance histogram clearly shows, the majority of the distance values are higher than those in the literature. The error map presents very high errors for the DMT standards, which does not correlate with the distance map deviations.

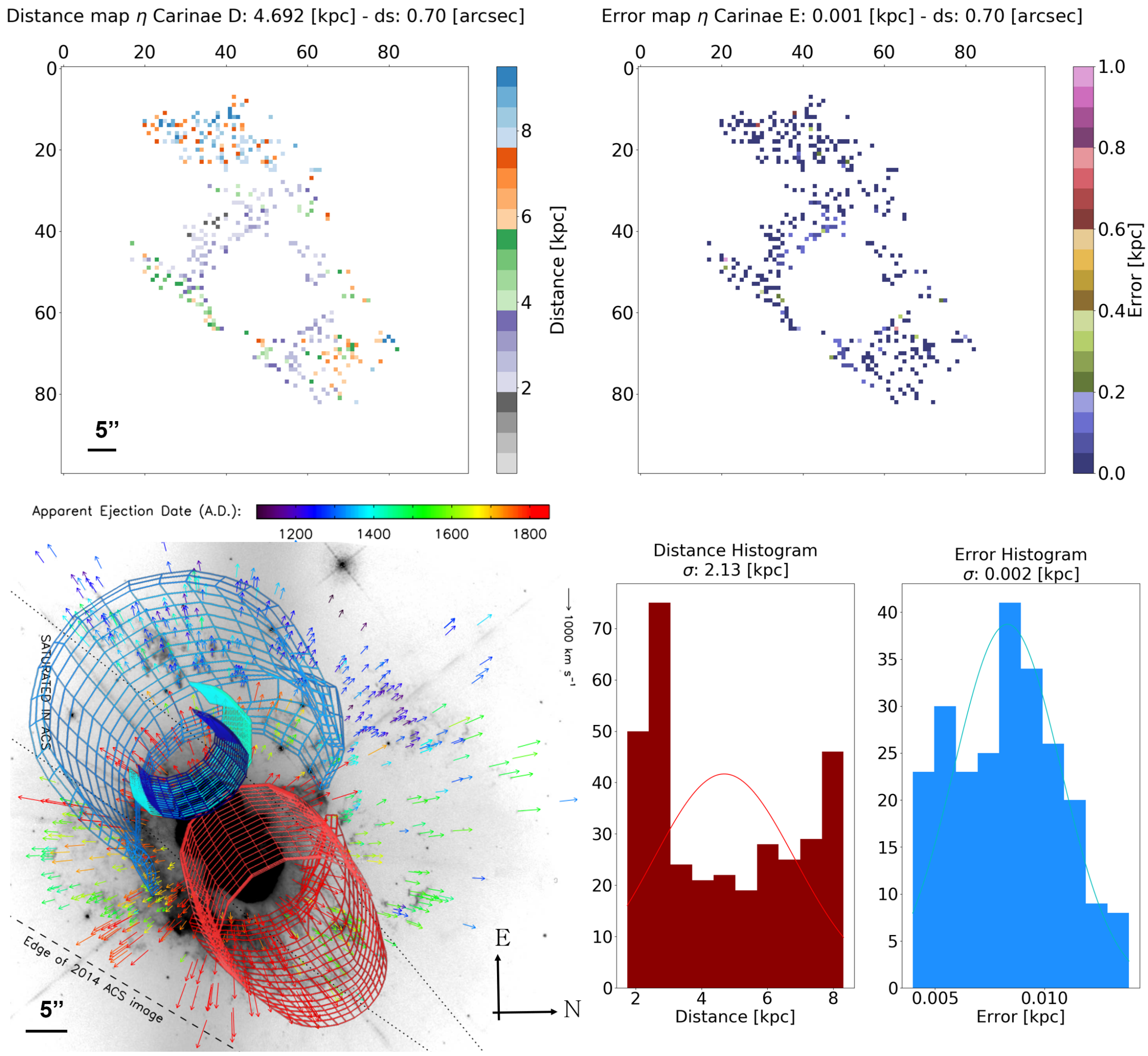

FIGURE 3.17: *Upper panel:* distance (*left*) and error (*right*) maps. *Lower panel:* Model with all the components at the same time overlaid on the proper motions image of the outer ejecta (Kiminki et al., 2016) (*left*) and the histograms (*right*).

Component model name	Distance [kpc]	re [arcsec]
Bottom south outer shell	3.1 $\pm$ 0.07	7
Top north outer shell	7 $\pm$ 0.001	0.7
Bottom north outer/ghost shell	3.8 $\pm$ 0.1	7
Reduce ghost shell	3 $\pm$ 0.004	0.7
Extended ghost shell	2.27 $\pm$ 0.003	0.7

TABLE 3.6: Distance estimations for the individual model components

The results from the case, on which the DMT is applied to each component of the model separately, after accounting for the coefficients of variations analysis, are presented in Table 3.6. One can see that the DMT gives, for the ghost shell, a distance of 2.27 $\pm$ 0.003 kpc ($re = 0.7$ arsecs). This distance value is consistent with previous studies, while for the rest of the components we get distances totally inconsistent with

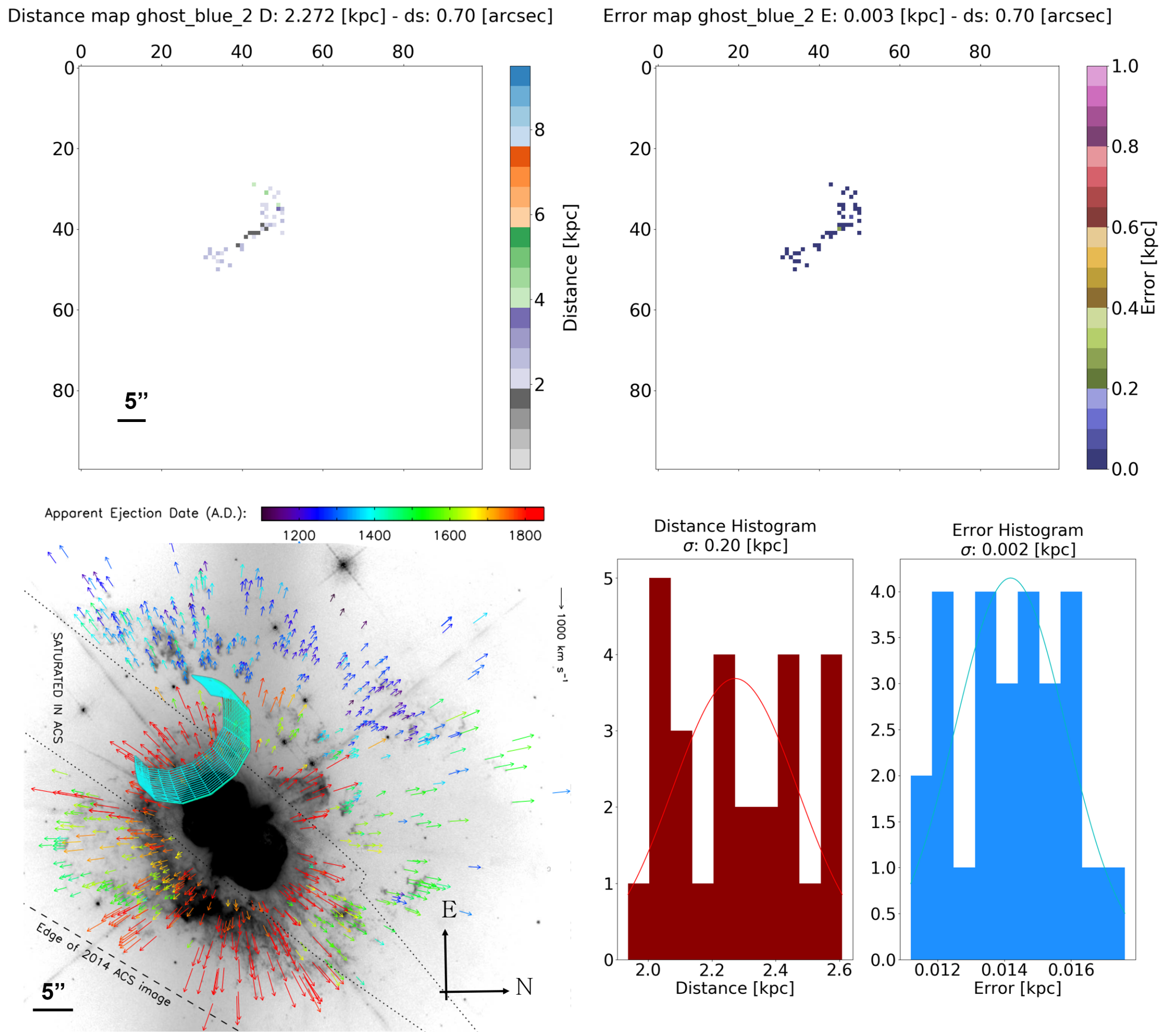

FIGURE 3.18: *Upper panel:* distance (*left*) and error (*right*) maps. *Lower panel:* Model with the extended ghost shell component at the overlaid on the proper motions image of the outer ejecta (Kiminki et al., 2016) (*left*) and the histograms (*right*).

the literature. For the extended ghost shell, the distance and error maps along with the histograms are present in Fig. 3.18. Few proper motions are covered by this component, and most of them seem to be formed by the great eruption (1800s). Note that the distance histogram shows a distance values distribution confined to a small interval, of only 0.6 kpc.

A link between the age of the features for, which proper motions are measured (see lower left panel, Fig. 3.17), and the derived distances has been found. The older the features, the higher the distance value. Then, it is possible to translate the relation between the distance and the age of the features by means of Eq. (1.3) into a relationship between the distance and the observed angular expansion of different epochs. Therefore, the older ejecta is expanding slower than the recent one, as the colored vectors in Fig. 7 of Kiminki et al. (2016) suggest.

According to this analysis, we conclude that complex multicomponent SHAPE models are not suitable for the DMT. This model of the outer ejecta of η Carinae is a good example of such complexity. Despite of that, we report that one of the component presents a distance estimation that agrees with the distance values from previous studies, and we also provided its respective 1σ distance range, 2.07 - 2.47 kpc, based on $\sigma_D = 0.2$ kpc.

Distance [kpc]	Reference
2.2 ± 0.2	Allen & Hillier (1993)
2.25	Walborn (1995)
2.3 ± 0.2	Davidson & Humphreys (1997)
2.3 ± 0.3	Meaburn (1999)
$2.25 \pm 10\%$	Davidson et al. (2001)
2.3	Smith (2002)
2.35 ± 0.05	Smith (2006)
2.27 ± 0.003	Present work
2.07 - 2.47	Present work

Table 3.7: η Carinae distances determinations.

4

Discussions and conclusions

The main objective of the research in this master thesis was to derive more accurate distances for a sample of 6 nebulae using an improved version of the distance mapping technique.

Besides a single distance value to each nebula, the DMT allows to study the distance of the nebulae in a spatially-resolved fashion through the generation of the distance and error maps. With these distance maps we can also look for regions that have systematically different distance values compared to the average, possibly associated with physical phenomena as local acceleration or deceleration of the nebula. The histograms of the distances produced by the DMT can also be used to study the distribution of values and define a range of possible distances for each object.

Before applying the DMT to real data, it was necessary to carry out a detailed statistical analysis on the DMT itself. There is a number of input parameters ($n, q, \mathcal{I}n, PA$) that can affect the results of the DMT, so they deserved further study. In the first part of the statistical study we derived the relations between the studied parameters that are direct inputs of the DMT (re and q) and the DMT distance calculation. We found that the best range of values for q and n that give the lowest error and distance dispersion are $q \geq 100$ and $50 \leq n \leq 100$. We also concluded that the low-resolution maps and low number of proper motions systematically result in higher errors.

Nebula	i [arcsec]	re [arcsec]	n [cells]	q [vectors]	Distance [kpc]
NGC 6543	60	1.2	50	107	1.19 ± 0.11
NGC 6720	500	25	20	22	1.074 ± 0.215
BD+30 3639 (M1)	7	0.23	30	178	1.35 ± 0.21
BD+30 3639 (M2)	7	0.12	60	178	1.32 ± 0.2
NGC 6302	65	2.6	25	200	1.03 ± 21
GK Persei	130	1.44	90	117	0.398 ± 0.023
η Carinae outer ejecta	70	0.7	100	792	2.27 ± 0.003

Table 4.1: i, re, n and q parameters and distance estimated for the nebulae of this work.

We conclude the statistical study by finding the relation between the orientation ($\mathcal{I}n$ and dPA) and the geometrical shape (spheric or bipolar) of the modeled nebulae with the DMT distance. We found that variations in the inclination angle ($\mathcal{I}n$) of the model generate variations in the distance of up to 2%, for the recommended ranges of

re and q. On the contrary, the DMT distance was found to be unaffected by possible deviations, up to ±15°, in the PA. These results indicate that, by using the DMT, small variations in the inclination and position angle of models have negligible effect in the calculated distance.

The proposed range for the resolution, re, derived from the statistical study was further tested with the actual application of the DMT to the nebulae, with values outside and inside of the range. To choose the best distance estimation among all the map resolutions, we developed a coefficient of variation analysis (Section 3.1.3), in which the distance and error maps with lower dispersion and clearer morphological features (as long as there are enough proper motions to resolve the morphological feature) are selected. Table 4.1 lists the image size (i), the resolution (re) and the number of cells (n), along with the available proper motions of each nebula treated in this work. In three cases the resolution of the maps has been found to be outside the recommended range. On the other hand, the upper limit of the resolution range was not violated in any of the above cases. Therefore, for future application of the method, we decided to change the recommended resolution range to $20 \leq n \leq 100$, due to the satisfactory distance determination of all these cases.

We demonstrated that the DMT is a constructive generalization of the expansion parallax method. By applying the expansion parallax method for different locations in the nebula, where several proper motions were measured, various distances are calculated from which a mean distance value is derived. Therefore, the first application of the DMT by Akras & Steffen (2012), and the estimated nebular distance in this work, probe that this technique is an accurate and robust distance determination method for expanding nebulae. We also demonstrated that the DMT can be applied to other expanding nebulae than PN, as long as there are available data sets of tangential velocity vectors (derived from three-dimensional morpho-kinematic models) and data sets of angular expansion velocity vectors (measured proper motions). We successfully used the DMT to calculate the distance for four PNe (NGC 6702, NGC 6543, NGC 6302 and BD+30 3639), a nova remnant (GK Persei) and the outer ejecta of a LBV (η Carinae).

By using SHAPE we carried out our own morpho-kinematic modeling for NGC 6543, NGC 6302 and NGC 6720. Regarding to NGC 6543 and NGC 6720, we tried to reproduce the 3D structure of the whole nebula, while for NGC 6302 only the eastern lobe, due to the limited availability of the proper motions. A single homologous velocity law was considered for all the SHAPE models. We reported that the DMT distances for these PNe agree very well with most of the values published in the literature, in spite of the simple geometrical and kinematical approach applied in this work.

The bipolar PN NGC 6543 was modeled as a bipolar structure with a homologous expansion, where the lobes are spherical shells of constant density. With the modeled tangential vectors and more than 100 proper motions, a distance of 1.19 ± 0.11 kpc was calculated using the DMT. An additional 1σ range, 0.9 - 1.48 kpc, which encloses 54% of the distances in the literature, was also provided. Two SDRs below the mean distance value were identified in the distance maps of NGC 6543. These SDRs are likely product of proper motions that combine the expansion of two different nebular components (the inner ellipse and the conjoined bubbles) resulting in higher proper motions, and thus lower distances.

The model for NGC 6720 followed an elliptical prolate shell viewed pole-on. From which modeled tangential vectors were exported and used in the DMT together with 22 proper motions. We calculated a distance of 1,074 $\pm$ 215 pc that encloses 70% of literature values along with the 1σ range, between 828 and 1,320 pc.

Two morpho-kinematic models (M1 and M2) with different geometrical and kinematical approaches were used for BD+30 3639, plus more than 100 proper motions. By using the DMT, distances of 1.35 $\pm$ 0.21 kpc for M1 and 1.32 $\pm$ 0.2 kpc for M2, in well agreement with the literature, were estimated. The 1σ range of M1 (0.86 to 1.84 kpc) and of M2 (0.97 to 1.67 kpc) enclose 44% of the previous distance estimations. The performance of the new version of the DMT presented in this work have been corroborated, by applying the DMT to the same nebula (BD+30 3639) of the first application. Two SDRs (SDR A and C) are present in the distance maps of the models M1 and M2. These SDRs escape from a physical explanation since they persist through two different modeling approaches.

A portion of the eastern lobe of the bipolar PN NGC 6302 was modeled as a conical shell. Using the exported tangential vectors from this model and 200 proper motions, the resultant DMT distance is 1.03 $\pm$ 0.21 kpc. 64% of the previous distances are enclosed by our derived value.

A multicomponent SHAPE model for the GK Persei nova remnant was used in the DMT along with more than 100 proper motions. A distance of 398 $\pm$ 23 pc was derived together with the 1σ range, from 828 to 1,320 pc, both well in agreement with the literature, enclosing 64% of the quoted values.

The DMT was finally applied for the multicomponent SHAPE model of the outer ejecta of η Carinae, along with more than 700 proper motions. Two different approaches for the application of the DMT were used. In the first approach, we used all the components in the DMT and the derived distance of 4.7 kpc is inconsistent with the literature. In the second approach, the DMT was applied to each of the component separately. Only the distance of one component, the extended ghost shell, of 2.27 $\pm$ 0.003 kpc, together with its 1σ range, 2.07 - 2.47 kpc, agree with the literature values, whereas the other 4 components have inconsistent distances. We conclude that multicomponent models of such complexity, as the outer ejecta of η Carinae, are not appropriate for the DMT application.

Bibliography

Akras, S., Clyne, N., Boumis, P., Monteiro, H., Gonçalves, D. R., Redman, M. P., & Williams, S. 2016, MNRAS, 457, 3409

Akras, S., & Steffen, W. 2012, MNRAS, 423, 925

Allen, D. A., & Hillier, D. J. 1993, Proceedings of the Astronomical Society of Australia, 10, 338

Aller, L. H. 1976, PASP, 88, 574

Anupama, G. C., & Kantharia, N. G. 2005, A&A, 435, 167

Bachiller, R., Forveille, T., Huggins, P. J., Cox, P., & Maillard, J. P. 2000, A&A, 353, L5

Bailey, J. 1981, MNRAS, 197, 31

Balick, B. 1987, AJ, 94, 671

Balick, B., & Frank, A. 2002, ARA&A, 40, 439

Balick, B., Wilson, J., & Hajian, A. R. 2001, AJ, 121, 354

Barlow, E. J., Knigge, C., Bird, A. J., J Dean, A., Clark, D. J., Hill, A. B., Molina, M., & Sguera, V. 2006, MNRAS, 372, 224

Barral, J. F., Canto, J., Meaburn, J., & Walsh, J. R. 1982, MNRAS, 199, 817

Bernard-Salas, J., Pottasch, S. R., Wesselius, P. R., & Feibelman, W. A. 2003, A&A, 406, 165

Bianchi, L., Cerrato, S., & Grewing, M. 1986, A&A, 169, 227

Bildsten, L., & Deloye, C. J. 2004, ApJ, 607, L119

Bode, M. F. 2004, in Astronomical Society of the Pacific Conference Series, Vol. 313, Asymmetrical Planetary Nebulae III: Winds, Structure and the Thunderbird, ed. M. Meixner, J. H. Kastner, B. Balick, & N. Soker, 504

Bode, M. F., & Evans, A. 2008, Classical Novae

Bresolin, F., Stasińska, G., Vílchez, J. M., Simon, J. D., & Rosolowsky, E. 2010, MNRAS, 404, 1679

Bryce, M., Balick, B., & Meaburn, J. 1994, MNRAS, 266, 721

Bryce, M., Meaburn, J., Walsh, J. R., & Clegg, R. E. S. 1992, MNRAS, 254, 477

Bryce, M., & Mellema, G. 1999, MNRAS, 309, 731

Cahn, J. H. 1984, ApJ, 279, 304

Cahn, J. H., & Kaler, J. B. 1971, ApJS, 22, 319

Cahn, J. H., Kaler, J. B., & Stanghellini, L. 1992, A&AS, 94, 399

Castor, J. I., Lutz, J. H., & Seaton, M. J. 1981, MNRAS, 194, 547

Cazetta, J. O., & Maciel, W. J. 2001, Ap&SS, 277, 393

Chong, S.-N., Kwok, S., Imai, H., Tafoya, D., & Chibueze, J. 2012, The Astrophysical Journal, 760, 115

Chu, Y.-H., Guerrero, M. A., Gruendl, R. A., Williams, R. M., & Kaler, J. B. 2001, ApJ, 553, L69

Ciardullo, R. 2012, Ap&SS, 341, 151

Corradi, R. L. M., Steffen, M., Schönberner, D., & Jacob, R. 2007, A&A, 474, 529

Crampton, D., Fisher, W. A., & Cowley, A. P. 1986, ApJ, 300, 788

Currie, D. G., Dorland, B. N., & Kaufer, A. 2002, A&A, 389, L65

Damineli, A., Kaufer, A., Wolf, B., Stahl, O., Lopes, D. F., & de Araújo, F. X. 2000, ApJ, 528, L101

Daub, C. T. 1982, ApJ, 260, 612

Davidson, K., & Humphreys, R. M. 1997, ARA&A, 35, 1

Davidson, K., & Humphreys, R. M., eds. 2012, Astrophysics and Space Science Library, Vol. 384, Eta Carinae and the Supernova Impostors

Davidson, K., Smith, N., Gull, T. R., Ishibashi, K., & Hillier, D. J. 2001, AJ, 121, 1569

Downes, R. A., & Duerbeck, H. W. 2000, AJ, 120, 2007

Duerbeck, H. W. 1981, PASP, 93, 165

Dufour, R. J., Glover, T. W., Hester, J. J., Curie, D. G., van Orsow, D., & Walter, D. K. 1997, in Astronomical Society of the Pacific Conference Series, Vol. 120, Luminous Blue Variables: Massive Stars in Transition, ed. A. Nota & H. Lamers, 255

Ercolano, B., Barlow, M. J., Storey, P. J., & Liu, X.-W. 2003, MNRAS, 340, 1136

ESA. 2016, Frequently asked question about GAIA

Frank, A., Balick, B., Icke, V., & Mellema, G. 1993, The Astrophysical Journal, 404, L25

Freeman, M. J., & Kastner, J. H. 2016, ApJS, 226, 15

Frew, D. J. 2008, PhD thesis, Department of Physics, Macquarie University, NSW 2109, Australia

Frew, D. J., & Parker, Q. A. 2010, PASA, 27, 129

Frew, D. J., Parker, Q. A., & Bojičić, I. S. 2016, MNRAS, 455, 1459

Garnett, D. R., & Dinerstein, H. L. 2001, ApJ, 558, 145

Gesicki, K., Acker, A., & Zijlstra, A. A. 2003, A&A, 400, 957

Gómez, Y., Rodríguez, L. F., & Moran, J. M. 1993, ApJ, 416, 620

Gómez, Y., Ródriguez, L. F., Moran, J. M., & Garay, G. 1989, ApJ, 345, 862

Gonçalves, D. R., Corradi, R. L. M., & Mampaso, A. 2001, ApJ, 547, 302

Guerrero, M. A., Manchado, A., & Chu, Y.-H. 1997, ApJ, 487, 328

Gurzadyan, G. 1997, The Physics and Dynamics of Planetary Nebulae, Astronomy and Astrophysics Library (Springer Berlin Heidelberg)

Hajian, A. R. 2006, Proceedings of the International Astronomical Union, 2, 41

Hajian, A. R., Terzian, Y., & Bignell, C. 1993, AJ, 106, 1965

Harris, H. C., et al. 2007, The Astronomical Journal, 133, 631

Harrison, T. E., Bornak, J., McArthur, B. E., & Benedict, G. F. 2013, ApJ, 767, 7

Harvey, E., Redman, M. P., Boumis, P., & Akras, S. 2016, A&A, 595, A64

Herwig, F., Blöcker, T., Langer, N., & Driebe, T. 1999, A&A, 349, L5

Hiriart, D. 2004, PASP, 116, 1135

Huarte-Espinosa, M., Frank, A., Balick, B., Blackman, E. G., De Marco, O., Kastner, J. H., & Sahai, R. 2012, MNRAS, 424, 2055

Hutsemekers, D., & Surdej, J. 1987, A&A, 173, 101

Icke, V. 1988, Astronomy and Astrophysics, 202, 177

Icke, V., Mellema, G., et al. 1992, Nature, 355, 524

Iglewicz, B., & Hoaglin, D. C. 1993, How to detect and handle outliers, Vol. 16 (Asq Press)

Jiménez, S. G. N. 2005, Determinación de distancias a nebulosas planetarias (Universidad de La Laguna)

Kaler, J. B., Mo, J.-E., & Pottasch, S. R. 1985, ApJ, 288, 305

Kawamura, J., & Masson, C. 1996, ApJ, 461, 282

Kiminki, M. M., Reiter, M., & Smith, N. 2016, MNRAS, 463, 845

King, D. J., Scarrott, S. M., & Shirt, J. V. 1985, MNRAS, 213, 11P

Kippenhahn, R., & Weigert, A. 2012, Stellar Structure and Evolution, Astronomy and Astrophysics Library (Springer Berlin Heidelberg)

Kwok, S. 2007, The Origin and Evolution of Planetary Nebulae, Cambridge Astrophysics (Cambridge University Press)

Kwok, S., Chong, S.-N., Koning, N., Hua, T., & Yan, C.-H. 2008, ApJ, 689, 219

Kwok, S., Purton, C. R., & Fitzgerald, P. M. 1978, The Astrophysical Journal, 219, L125

Lago, P. J. A., & Costa, R. D. D. 2014, in Revista Mexicana de Astronomia y Astrofisica, vol. 27, Vol. 44, Revista Mexicana de Astronomia y Astrofisica Conference Series, 135–136

Leuenhagen, U., Hamann, W.-R., & Jeffery, C. S. 1996, A&A, 312, 167

Li, J., Harrington, J. P., & Borkowski, K. J. 2002, The Astronomical Journal, 123, 2676

Liimets, T., Corradi, R. L. M., Santander-García, M., Villaver, E., Rodríguez-Gil, P., Verro, K., & Kolka, I. 2012, ApJ, 761, 34

López, J. A., Richer, M. G., García-Díaz, M. T., Clark, D. M., Meaburn, J., Riesgo, H., Steffen, W., & Lloyd, M. 2012, Rev. Mexicana Astron. Astrofis., 48, 3

Lutz, J. 1973, The Astrophysical Journal, 181, 135

Maciel, W. J. 1984, A&AS, 55, 253

Maciel, W. J., & Pottasch, S. R. 1980, A&A, 88, 1

Maeder, A. 2008, Physics, Formation and Evolution of Rotating Stars, Astronomy and Astrophysics Library (Springer Berlin Heidelberg)

Mal'Kov, Y. F. 1997, Astronomy Reports, 41, 760

Masson, C. R. 1989, ApJ, 346, 243

McLaughlin, D. B. 1960, The Spectra of Novae, ed. J. L. Greenstein (the University of Chicago Press), 585

Meaburn, J. 1999, in Astronomical Society of the Pacific Conference Series, Vol. 179, Eta Carinae at The Millennium, ed. J. A. Morse, R. M. Humphreys, & A. Damineli, 89

Meaburn, J., Lloyd, M., Vaytet, N., & López, J. 2008, Monthly Notices of the Royal Astronomical Society, 385, 269

Meaburn, J., López, J. A., Steffen, W., Graham, M. F., & Holloway, A. J. 2005, AJ, 130

Mehner, A., et al. 2016, A&A, 595, A120

Mellema, G. 2004, Astronomy & Astrophysics, 416, 623

Mellema, G., & Frank, A. 1995, Monthly Notices of the Royal Astronomical Society, 273, 401

Méndez, R., Kudritzki, R., Herrero, A., Husfeld, D., & Groth, H. 1988, Astronomy and Astrophysics, 190, 113

Miranda, L. F., Torrelles, J. M., Guerrero, M. A., Vázquez, R., & Gómez, Y. 2001, Monthly Notices of the Royal Astronomical Society, 321, 487

Monteiro, H., & Falceta-Gonçalves, D. 2011, ApJ, 738, 174

Monteiro, H., & Schwarz, H. E. 2007, in Asymmetrical Planetary Nebulae IV

Monteiro, H., Schwarz, H. E., Gruenwald, R., Guenthner, K., & Heathcote, S. R. 2005, ApJ, 620, 321

Monteiro, H., Schwarz, H. E., Gruenwald, R., & Heathcote, S. 2004, ApJ, 609, 194

Morales-Rueda, L., Still, M. D., Roche, P., Wood, J. H., & Lockley, J. J. 2002, MNRAS, 329, 597

Napiwotzki, R. 2001, A&A, 367, 973

Natta, A., Pottasch, S. R., & Preite-Martinez, A. 1980, A&A, 84, 284

Neiner, C., Acker, A., Gesicki, K., & Szczerba, R. 2000, A&A, 358, 321

O'Dell, C. R. 1962, ApJ, 135, 371

O'Dell, C. R., Ferland, G. J., Henney, W. J., & Peimbert, M. 2013, AJ, 145, 170

O'Dell, C. R., Henney, W. J., & Sabbadin, F. 2009, AJ, 137

O'Dell, C. R., Sabbadin, F., & Henney, W. J. 2007, AJ, 134, 1679

Osterbrock, D., & Ferland, G. 2006, Astrophysics Of Gas Nebulae and Active Galactic Nuclei (University Science Books)

Peretto, N., Fuller, G., Zijlstra, A., & Patel, N. 2007, A&A, 473, 207

Perinotto, M., Cerruti-Sola, M., & Lamers, H. J. G. L. M. 1989, ApJ, 337, 382

Phillips, J. P. 2002, ApJS, 139, 199

—. 2004, MNRAS, 353, 589

—. 2005, MNRAS, 362, 847

Phillips, J. P. 2006, Revista mexicana de astronomía y astrofísica, 42, 229

Phillips, J. P., & Pottasch, S. R. 1984, A&A, 130, 91

Pottasch, S. 1959, Annales d'Astrophysique, 22, 412

Pottasch, S. 1980, Astronomy and Astrophysics, 89, 336

Pottasch, S. R., ed. 1984, Astrophysics and Space Science Library, Vol. 107, Planetary nebulae - A study of late stages of stellar evolution

Ramos-Larios, G., Santamaría, E., Guerrero, M. A., Marquez-Lugo, R. A., Sabin, L., & Toalá, J. A. 2016, Monthly Notices of the Royal Astronomical Society, 462, 610

Reed, D. S., Balick, B., Hajian, A. R., Klayton, T. L., Giovanardi, S., Casertano, S., Panagia, N., & Terzian, Y. 1999, The Astronomical Journal, 118, 2430

Renzini, A. 1979, in Astrophysics and Space Science Library, Vol. 75, Stars and star systems, ed. B. E. Westerlund, 155–171

Rodríguez, L. F., & Moran, J. M. 1982, Nature, 299, 323

Rodríguez, L. F., et al. 1985, MNRAS, 215, 353

Sabbadin, F., & Bianchini, A. 1983, A&AS, 54, 393

Sabbadin, F., Turatto, M., Ragazzoni, R., Cappellaro, E., & Benetti, S. 2006, A&A, 451, 937

Sahai, R., Morris, M. R., Werner, M. W., Güsten, R., Wiesemeyer, H., & Sandell, G. 2012, A&A, 542, L20

Sahai, R., & Trauger, J. T. 1998, The Astronomical Journal, 116, 1357

Salaris, M., & Cassisi, S. 2005, Evolution of Stars and Stellar Populations (Wiley)

Schönberner, D., Jacob, R., & Steffen, M. 2005, Astronomy & Astrophysics, 441, 573

Schwarz, H. E., & Monteiro, H. 2006, ApJ, 648, 430

Seaquist, E. R., Bode, M. F., Frail, D. A., Roberts, J. A., Evans, A., & Albinson, J. S. 1989, ApJ, 344, 805

Shaw, R. A., & Kaler, J. B. 1989, ApJS, 69, 495

Shaw, R. A., Stanghellini, L., Mutchler, M., Balick, B., & Blades, J. C. 2001, 548, 727

Sherrington, M. R., & Jameson, R. F. 1983, MNRAS, 205, 265

Shklovsky, I. 1956, Astron. J. Soviet Union, 33, 222

Slavin, A. J., O'Brien, T. J., & Dunlop, J. S. 1995, MNRAS, 276, 353

Smith, N. 2002, MNRAS, 337, 1252

—. 2006, ApJ, 644, 1151

Soker, N., & Livio, M. 1989, The Astrophysical Journal, 339, 268

Steffen, W. 2016, in Journal of Physics Conference Series, Vol. 728, Journal of Physics Conference Series, 032005

Steffen, W., Koning, N., Wenger, S., Morisset, C., & Magnor, M. 2011, IEEE Transactions on Visualization and Computer Graphics, 17, 454

Steffen, W., & López, J. A. 2006, Rev. Mexicana Astron. Astrofis., 42, 99

Szyszka, C., Walsh, J. R., Zijlstra, A. A., & Tsamis, Y. G. 2009, ApJ, 707, L32

Szyszka, C., Zijlstra, A. A., & Walsh, J. R. 2011, MNRAS, 416, 715

Terzian, Y. 1997, in IAU Symposium, Vol. 180, Planetary Nebulae, ed. H. J. Habing & H. J. G. L. M. Lamers, 29

Van de Steene, G., & Zijlstra, A. 1994, Astronomy and Astrophysics Supplement Series, 108

Walborn, N. R. 1995, in Revista Mexicana de Astronomia y Astrofisica Conference Series, Vol. 2, Revista Mexicana de Astronomia y Astrofisica Conference Series, ed. V. Niemela, N. Morrell, & A. Feinstein, 51

Warner, B. 1987, MNRAS, 227, 23

—. 1995, Cambridge Astrophysics Series, 28

Weis, K. 2001, in Astronomical Society of the Pacific Conference Series, Vol. 242, Eta Carinae and Other Mysterious Stars: The Hidden Opportunities of Emission Spectroscopy, ed. T. R. Gull, S. Johannson, & K. Davidson, 129

Weis, K. 2005, in Astronomical Society of the Pacific Conference Series, Vol. 332, The Fate of the Most Massive Stars, ed. R. Humphreys & K. Stanek, 275

Weis, K. 2012, The Outer Ejecta, ed. K. Davidson & R. M. Humphreys (Boston, MA: Springer US), 171–194

Wesson, R., & Liu, X.-W. 2004, MNRAS, 351, 1026

Williams, R. E. 1981, Scientific American, 244, 120

Zhang, C. Y. 1995, ApJS, 98, 659

Zhekov, S. A., & Perinotto, M. 1998, A&A, 334, 239

Ziegler, M., Rauch, T., Werner, K., & Kruk, J. W. 2012, in IAU Symposium, Vol. 283, IAU Symposium, 211–214

Zuckerman, B., Terzian, Y., & Silverglate, P. 1980, ApJ, 241, 1014

Zweigle, J., et al. 1997, A&A, 321, 891